

Université Lille I - Sciences et Technologies
Laboratoire de Mécanique de Lille (UMR CNRS 8107)
Ecole Doctorale SPI Lille Nord-de-France
Année 2014 - N° d'ordre : 41481

THESE

Pour obtenir le grade de
Docteur de l'Université Lille I - Sciences et Technologies

Discipline : Génie Civil
Présentée par

Lifeng ZHENG

Contribution à la modélisation du comportement différé du massif rocheux fracturé

Thèse soutenue le 24/07, 2014 à LML devant le jury composé de :

Sheng-Hong CHEN, Professeur, Wuhan Université Chine	Rapporteur
Dashnor HOXHA, Professeur, Université Orléans, France	Rapporteur
Nicolas BURLION, Professeur, Université de Lille I, France	Examineur
Djimédo KONDO, Professeur, Université Paris 6, France	Examineur
Hanbing BIAN, MCF, Université de Lorraine, France	Co-directeur de Thèse
Jian-Fu SHAO, Professeur, Université de Lille I, France	Directeur de Thèse

Acknowledgements

The works presented in this thesis is finished during the period September 2010 to July 2014. It would not have been possible to write this doctoral thesis without the help and support of the kind people around me. I would like to express my great gratitude to these professors and friends.

Foremost, I am deeply grateful to my principal supervisor, Professor Jian-fu Shao at Laboratoire de mécanique de Lille (LML), and to my co-supervisor, Assistant Professor Hanbing Bian at Université de Lorraine, for their continuous support, patience throughout my research, for their care and helps in my daily life.

I think it is a great honor to work with my colleagues during these years. They are Assistant Professor Yun Jia, Assistant Professor Qizhi Zhu, Assistant Professor Rougelot Thomas, Doctor Shouyi Xie, Doctor Lanoye Emma, Doctor Dawei Hu, Doctor Wanqing Shen, Doctor He Yang, Doctor Yue Liang, Doctor Caifeng Jin, Doctor Tao Zeng, Doctor Yun Huang, Doctor Jian Lin, Doctor Chi Yao, Doctor Zaobao Liu, Doctor Yu Zhang, Doctor Long Cheng, Mr Mingyao Li, Mr Qier Wu, Mr Hamid Gorbanbeigi, Miss Xiaotian Zhang, Miss Lin Liu, Mr Taogen Liu, Miss Ling Li, Miss Mei Qi at LML.

Last but not least, I wish to thank my parents, for their unconditional support, for never letting me forget that, even when everything seems to go wrong, life still goes on.

Lifeng Zheng

September 2014

Abstract

In recent years, several great hydraulic projects are taken into construction or were brought into operation. Because of the great height of dams, hydraulic slopes in these projects are normally high and steep. In analyzing the high steep slopes, slope stability is the major research object for dam site selection, engineering construction and geological hazard assessment.

Short-term and long-term stability are two important aspects in analyzing slope stability. The objective of this study is to propose the numerical models to simulate the short and long-term mechanical behaviour of rock matrix and rock joint.

For rock matrix, one elasto-damage model which takes both the compressive and tensile situations into account is employed. One parameter is introduced to emphasize the influence of confining pressures. And then one creep model for rock matrix which considering the damage parameter as a time-dependent variable is proposed. The simulation results show great agreement with experimental results.

Generally, rock joints are the most fragile part in rock structures, the deformations is tend to concentrate in joint part, and then cause the joint surface slip, even the failure of the whole rock structure. For rock joint, the asperity of joint surface is represented by a parameter *JRC*. This parameter is related to the friction angle, and then affects the shear stiffness of joint. In this work, a constitutive model is employed based on this theory, and then the parameter *JRC* is proposed to be a time-dependent variable, which represents the graduate degradation of joint asperity with time passage. One simulation is performed and verified that this model is capable to describe creep phenomena.

The extended finite element (XFEM) theory works by introducing additional degrees of freedom into traditional finite element theory to reflect the fracture position in elements. It is introduced and applied in the joint model to exactly describe the real condition of joint.

A simulation of one complicated structure is performed at last to verify the simulating ability of these models.

Keywords: rock; elasto-damage; rock joint, XFEM, time effect; long-term stability.

Résumé

Au cours des dernières années, plusieurs grands projets hydrauliques ont débuté leur construction ou ont été mis en service. En raison de la grande hauteur des barrages, les pentes des massifs rocheux constitutifs de la structure de l'ouvrage sont raides. L'instabilité de ces pentes pourrait conduire à de graves accidents de barrages. Pour cette raison, elles sont au cœur des problématiques dans le domaine des ouvrages hydrauliques et ont été analysées depuis de nombreuses années. Plus précisément, la stabilité de la pente est l'objet de recherche principal pour la sélection du site de réalisation d'un barrage, sa conception et l'évaluation des risques géologiques.

La stabilité des pentes à court terme n'est pas le seul sujet important dans la construction de barrage : plusieurs accidents dévastateurs des barrages ont eu lieu après des décennies d'années de fonctionnement de ces ouvrages hydrauliques. Par conséquent, la stabilité à court terme et à long terme sont deux aspects importants dans l'analyse de la stabilité des pentes. L'objectif de cette étude est de proposer des modèles numériques pour simuler le comportement mécanique à court et à long termes de la matrice rocheuse et des joints rocheux.

Pour la matrice rocheuse, un modèle élasto-endommageable, tenant compte des effets en traction et en compression, est utilisé. Un paramètre est introduit afin de représenter l'influence de la pression de confinement sur le comportement global. En outre, un modèle de fluage de la matrice rocheuse qui considère le paramètre d'endommagement comme une variable dépendant du temps est proposé. Les résultats des simulations sont en très bon accord avec les résultats expérimentaux.

Généralement, les joints rocheux sont la partie la plus fragile dans les structures rocheuses, les déformations ont tendance à se concentrer sur ces joints, puis engendrent le glissement des surface de joint, voire un effondrement de la structure. Pour les joints rocheux, l'aspérité des surfaces est représenté par un paramètre JRC . Ce paramètre est lié à l'angle de frottement, et donc affecte la rigidité en cisaillement de joint. Dans ce travail, un modèle constitutif est employé sur la base de cette théorie présentée, et le paramètre est proposé comme une variable dépendante du temps, ce qui représente la dégradation de l'aspérité avec le temps. Une simulation est réalisée et permet de vérifier que ce modèle est capable de décrire les phénomènes de fluage.

La méthode des éléments finis étendus (XFEM) permet d'introduire des degrés de liberté supplémentaires dans la théorie traditionnelle des éléments finis pour tenir compte de la position de la fracture dans les éléments. Elle est introduite et utilisée dans le modèle de joint pour décrire le plus précisément possible les conditions réelles qui leur sont appliquées.

Une simulation d'une structure complexe est finalement effectuée pour vérifier la capacité de simulation des modèles proposés.

Mots-clés: roche; élasto-endommageable; joint rocheux, XFEM, effet du temps; stabilité à long terme.

Table of content

Chapter 1. Introduction	1
1.1. Research background	1
1.2. Damage models for hard rock	10
1.3. Constitutive models for rock joint.....	12
1.4. Numerical method for discontinuity simulation.....	13
1.5. Creep models for rock materials	13
1.5.1. Experimental research on the creep.....	14
1.5.2. Numerical models for creep simulation	15
1.6. The main contents of the thesis	16
Chapter 2. Time-dependent elasto-damage constitutive model for hard rock	18
2.1. Introduction	18
2.2. Formulation of damage model for instantaneous mechanical behaviour.....	20
2.3. Identification of model parameters	22
2.4. Numerical simulation of laboratory tests	27
2.4.1. Numerical simulations of triaxial tests of Marble	27
2.4.2. Numerical simulations of triaxial tests of Meta-sandstone	31
2.5. Non-local form of proposed damage model.....	32
2.6. Time effects on the damage	37
2.7. Conclusion.....	42
Chapter 3. Time dependent constitutive model for rock joint.....	43
3.1. Introduction	43
3.2. Instantaneous behaviour of rock joint	44
3.2.1. The normal behaviour of rock joint in traction	46
3.2.2. The normal behaviour of rock joint in compression	47
3.2.3. The tangent behaviour of rock joint in shear.....	50
3.3. Numerical simulation of laboratory tests	54
3.3.1. Identification of model parameters	54
3.3.2. Numerical simulation of laboratory tests	57
3.4. Time effect in crack.....	60
3.4.1. Time effect of friction angle Φ_r	60
3.4.2. Time effect of joint roughness coefficient JRC	62
3.5. Conclusion.....	68
Chapter 4. Numerical method for the jointed rocks	69

4.1. Introduction	69
4.2. Basic theory of XFEM	69
4.3. Numerical implementation	73
4.4. Crack propagation criterions	75
4.4.1. Crack initiation criterion	75
4.4.2. Crack direction	78
4.5. A simple numerical application.....	79
4.6. Conclusion.....	85
Chapter 5. Long-term stability analysis of a jointed rock slope.....	86
5.1. Introduction	86
5.2. The geometry and the boundary conditions	88
5.3. The models and parameters	92
5.4. Numerical results and discussions.....	93
5.4.1. Numerical results for Joint N ^o 1.....	94
5.4.2. Numerical results for Joint N ^o 2.....	97
5.4.3. Numerical results for Joint N ^o 3.....	100
5.4.4. Discussions	103
5.5. Conclusion.....	108
Chapter 6. Conclusion and perspectives	109
6.1. General conclusion	109
6.2. Perspectives	110
References	111

List of figures

Figure 1.1 Big rivers and large hydraulic projects at southwest of China	1
Figure 1.2 Locations of Jinping I and Jinping II at Yalong River	2
Figure 1.3 Jinping I, the largest arch dam in the world in construction.....	3
Figure 1.4 Nuozhadu Hydropower Project	3
Figure 1.5 Xiaowan Hydropower Project under construction.....	4
Figure 1.6 Xiluodu Hydropower Project under construction	5
Figure 1.7 The bird view of the Three Gorges Projects	6
Figure 1.8 A landslide in reservoir area	7
Figure 1.9 (a) The panorama of Vajont Dam before and after the disaster.....	8
Figure 1.10 (b) Illustration of the interlayer (joint) of claystone in left bank of the reservoir where the landslide occurs	8
Figure 2.1 Typical stress-strain curve of the hard rock under uniaxial compression and traction.....	23
Figure 2.2 Influence of parameter B_c on the stress-strain and damage-strain curve	24
Figure 2.3 Influence of parameter Y_{c0} on the stress-strain and damage-strain curve	25
Figure 2.4 Influence of confining pressure and parameter n	26
Figure 2.5 Flow chart of the elasto-damage model for instantaneous mechanical behaviour.....	28
Figure 2.6 Numerical simulations of the triaxial tests of group 1 of marble	29
Figure 2.7 Numerical simulations of the triaxial tests of group 2 of marble	29
Figure 2.8 Numerical simulations of the triaxial tests of group 3 of marble	30
Figure 2.9 Numerical simulations of the triaxial tests of group 4 of marble	30
Figure 2.10 Numerical simulations of the triaxial tests of group 5 of marble	31
Figure 2.11 Numerical simulations of the triaxial tests of group 1 of Meta-sandstone ...	32
Figure 2.12 Numerical simulations of the triaxial tests of group 2 of Meta-sandstone ...	32
Figure 2.13 Simple beam model under uniaxial compression controlled by displacement	33
Figure 2.14 Three meshes with different element densities.....	33
Figure 2.15 The distribution of Damage for three different meshes	34
Figure 2.16 Distribution of damage based on length, local model	34
Figure 2.17 Results of the model non-local	36
Figure 2.18 Distribution of damage based on length, non-local model	36
Figure 2.19 Influence of parameter l_c on the damage distribution.....	37

Figure 2.20 A typical creep curve for hard rock in the first creep stage	38
Figure 2.21 Time effect in damage and Young's modulus	39
Figure 2.22 Influence of parameter m in creep curves.....	40
Figure 2.23 Influence of parameter β in creep curves.....	40
Figure 2.24 Validation with the creep experiments	41
Figure 3.1 Crack in macro-scale	45
Figure 3.2 Idealized rock joint with regular asperities.....	45
Figure 3.3 Fracture energy of in traction.....	47
Figure 3.4 Simulation of Marble of St Pons.....	49
Figure 3.5 Simulation of Granite of Tennesles.....	49
Figure 3.6 Simulation of Schist of Trézazé.....	50
Figure 3.7 Typical roughness profiles for JRC range (Bandis) [80]	53
Figure 3.8 Sensitive analyse of JRC_0	54
Figure 3.9 Sensitive analyse of JCS_0	55
Figure 3.10 Sensitive analyse of Φ_r	55
Figure 3.11 Sensitive analyse of L_n	56
Figure 3.12 Sensitive analyse of L_0	56
Figure 3.13 Sensitive analyse of a	57
Figure 3.14 Sensitive analyse of b	57
Figure 3.15 Results of simulations for joint.....	59
Figure 3.16 Illustration of the friction angle degradation in function of time	61
Figure 3.17 The degradation of residual friction angle in function of time with different velocities.....	61
Figure 3.18 Influence of the degradation of the residual friction angle on the mechanical behaviour of rock joint under constant normal stress	62
Figure 3.19 The degradation of α in function of time with different velocities.....	63
Figure 3.20 Influence of the degradation of α on the mechanical behaviour of rock joint under constant normal stress	63
Figure 3.21 Sensitive analyses of parameter $B (JRC)$	64
Figure 3.22 Sensitive analyses of parameter $B (K_{tt})$	64
Figure 3.23 Sensitive analyses of parameter B (strain).....	65
Figure 3.24 Sensitive analyses of parameter JRC_0 (strain).....	65
Figure 3.25 Sensitive analyses of parameter JRC_∞ (strain)	66
Figure 3.26 Sensitive analyses of parameter $\sigma_n (K_{tt})$	66
Figure 3.27 Sensitive analyses of parameter σ_n (strain).....	67

Figure 3.28 Numerical simulation of direct shear tests compared with experimental data	68
Figure 4.1 A domain crossed by a crack	70
Figure 4.2 A classical finite element mesh crossed by a crack	74
Figure 4.3 The integration schema for a 2D 4node element crossed by crack	75
Figure 4.4 A specimen of concrete under uniaxial traction	76
Figure 4.5 Identification of the critical damage for the crack initiation	77
Figure 4.6 The evolution of stress versus strain in the specimen under uniaxial traction	78
Figure 4.7 The geometry and boundary conditions of a rock mass	79
Figure 4.8 The given mesh and the two pre-existed joints with different incline angles.	80
Figure 4.9 The final displacement of two simulations on the deformed mesh	81
Figure 4.10 The time history of the displacement of Point A and B respectively for the two inclined joint and the time history of the degradation of K_t	82
Figure 4.11 The time history of the displacement of Point A and B respectively for the two inclined joint.....	82
Figure 4.12 The variation of the JRC during the 100years for the two inclined joint	83
Figure 4.13 The variation of α_0 during the 100years for the two inclined joint.....	84
Figure 4.14 The time history of the displacement of Point A and B respectively for the two inclined joint and the time history of the degradation of K_t	84
Figure 5.1 The typical V valley with two high steep rock slopes at both side.....	86
Figure 5.2 The height steep rock slope during the phase of excavation	87
Figure 5.3 Position of the typical section chosen for study	88
Figure 5.4 Geometry, boundary conditions and material groups.....	89
Figure 5.5 The position of the three main joints in the rock mass	91
Figure 5.6 The distribution of the stress in the rock mass due to the gravity	94
Figure 5.7 The distribution of the displacement in section N ¹	95
Figure 5.8 The distribution of the stress in the rock mass due to the joint degradation N ¹	96
Figure 5.9 The distribution of the damage in the rock mass due to the joint degradation N ¹	97
Figure 5.10 The distribution of the displacement in section N ²	98
Figure 5.11 The distribution of the stress in the rock mass due to the joint degradation N ²	99
Figure 5.12 The distribution of the damage in the rock mass due to the joint degradation N ²	100

Figure 5.13 The distribution of the displacement in section N 3.....	101
Figure 5.14 The distribution of the stress in the rock mass due to the joint degradation N 3	102
Figure 5.15 The distribution of the damage in the rock mass due to the joint degradation	103
Figure 5.16 The position of the observation gallery in current section (From internal report).....	104
Figure 5.17 The position of the detectors in the observation gallery (From internal report)	104
Figure 5.18 The historical displacement of each observation points (From internal report)	105
Figure 5.19 The historical displacement in X direction of three observation points induced by the degradation of Joint N 1	106
Figure 5.20 The historical displacement in Y direction of three observation points induced by the degradation of Joint N 1	106
Figure 5.21 The historical displacement in X direction of three observation points induced by the degradation of Joint N 2.....	107
Figure 5.22 The historical displacement in Y direction of three observation points induced by the degradation of Joint N 2.....	107
Figure 5.23 The historical displacement in X direction of three observation points induced by the degradation of Joint N 3.....	108
Figure 5.24 The historical displacement in Y direction of three observation points induced by the degradation of Joint N 3.....	108

List of tables

Table 2.1 Basic parameters for a typical Marble.....	23
Table 2.2 Parameters used for 5 groups of Marble rock	28
Table 2.3 Parameters used for 2 groups of Meta-Sandstone.....	31
Table 2.4 Model parameters for two materials	33
Table 2.5 Model parameter for first creep stage	39
Table 2.6 Model parameters for creep test of a claystone.....	41
Table 3.1 Crack parameters for joint compressive simulations	48
Table 3.2 Basic parameters for the sensitive analyses	54
Table 3.3 Crack parameters for joint shear simulations.....	58
Table 3.4 Basic crack parameters for sensitive analyse	63
Table 3.5 Crack parameters for creep simulation of joints	67
Table 4.1 Model parameters for concrete under uniaxial traction	76
Table 4.2 Parameters for the simulation of simple slope	81
Table 4.3 Model parameters for the JRC degradation	83
Table 5.1 The rock groups in the chosen section	89
Table 5.2 Properties of rocks in different grades (according to [97] and [98]).....	92
Table 5.3 Essential mechanical properties of each rock group	92
Table 5.4 Damage parameters for 7 rock groups	93
Table 5.5 The essential parameters used for the three joints	93

Chapter 1. Introduction

1.1. Research background

China has been putting efforts into the development of hydropower stations in recent decades of years in order to meet the increasing demand of electricity resulting from rapid growth of the economy. Started from 2000, one of the key goals of Western Development Strategy is to exploit numerous rivers for power production in the southwest region, such as Yalong River, Jinsha River and Lancang River as illustrated in Figure 1.1. A number of large scale hydraulic projects are currently being assessed at their feasibility stages; some of them are in construction or have already been put into production, such as the projects Three Gorges, Xiluodu, Xiangjiaba, Nouzhadu, Jinping I, Jinping II, and Xiaowan, etc. These projects are mostly located in Sichuan and Yunnan Provinces, the mountainous southwest of China.

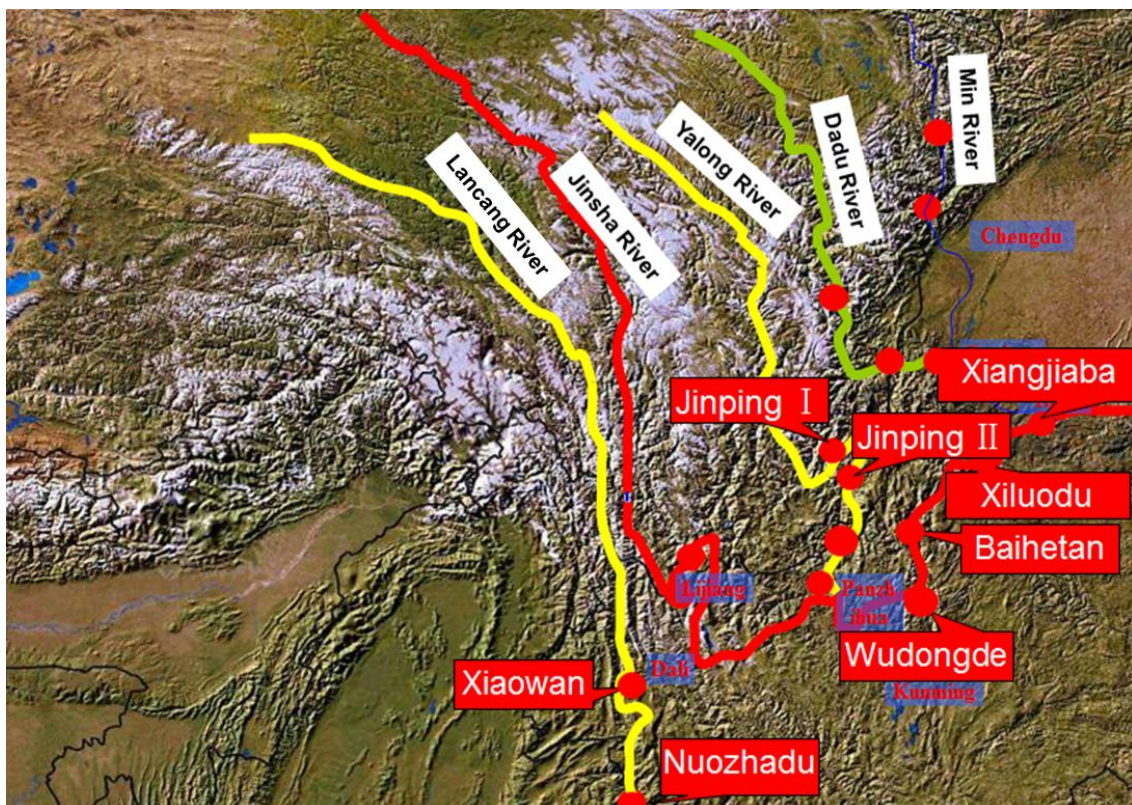


Figure 1.1 Big rivers and large hydraulic projects at southwest of China

The Jinping River bend on the Yalong River is one of famous river bends in China. The length of the bend is about 150 km but the downstream part of the river on the opposite side is

only separated by 16 km, as illustrated in Figure 1.2. The 310 m elevation drop between these two places creates an excellent situation for hydroelectricity production. Two projects were planned for exploiting the bend of the Jinping I and Jinping II with a combined capacity of 8,000 MW. The Jinping I is composed by a dam with a height of 305m which is the highest double-curvature thin arch dam in the world. The total installed capacity of Jinping I is 3,600 MW while that of Jinping II is 4400MW. The waters accumulated at Jinping I will be transferred along four long headrace tunnels of 16.6 km to the Jinping II, which located in 7.5 km downstream of Jinping I, to supply the hydraulic power production.

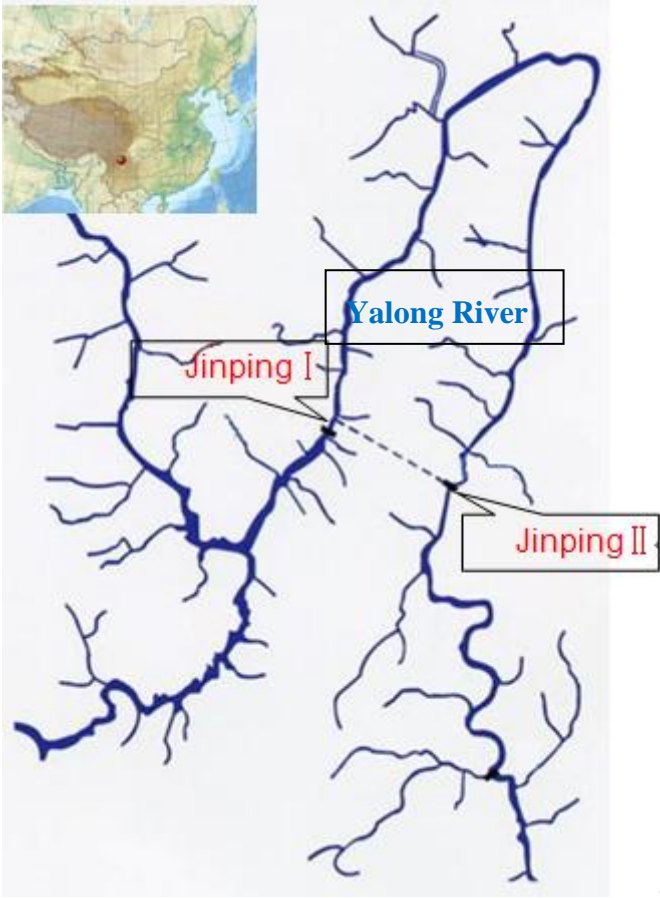


Figure 1.2 Locations of Jinping I and Jinping II at Yalong River

As the largest hydroelectric project on the Upper Lancang River (Mekong River) Basin, in Yunnan Province, southwest China, the Nuozhadu hydraulic power station near Pu'er is the fourth largest hydropower in China. With the height of 261.5 m, the dam is one of the largest earth-rock filled dams over the world, and creates a reservoir with a normal storage capacity of 21,749,000,000 m^3 at a water level of 812m. The main application of the dam is hydroelectric power production, flood control and navigation. The dam will support a power station with nine power generators and each of them generates a capacity of 650 MW. The total generating capacity of the project is 5,850 MW, which is enough for seven months of

power consumption of New York City. The energy generated by Nuozhadu per year is equivalent to the power production of more than nine million tons of coal.



Figure 1.3 Jinping I, the largest arch dam in the world in construction



Figure 1.4 Nuozhadu Hydropower Project

The Xiaowan Hydropower Project is composed by a double-curvature arch dam (292 m high and 902m long in crest) located on the Upper Lancang (Mekong) River in Yunnan Province, southwest China. The primary purpose of the dam is hydroelectric power generation. It has an underground powerhouse on the right bank and one spillway tunnel in the left bank. The flood discharge structures in dam include five surface spillways, six middle outlets, and two bottom outlets. The maximum capacity of flood discharge is $20709 \text{ m}^3 / \text{s}$. The underground powerhouse located on the right bank has six turbines and each of them has 700

MW installed capacity. It is the world's second highest arch dam (292 m) and the third largest hydroelectric power station in China.



Figure 1.5 Xiaowan Hydropower Project under construction

As illustrated in Fig 1.1, Xiangjiaba, Xiluodu, Baihetan and Wudongde are cascade dams located at the Jinsha River, a tributary of the Yangtze River, in Yunnan provinces in the southwest of China. The Wudongde Dam is a large hydroelectric dam currently under construction mainly for power generation, flood control, and sediment trapping. The dam will generate power by utilizing 12 turbines, each with a generating capacity of 725 MW, totaling the generating capacity of 8700 MW. Construction began in 2014, and the first generator is scheduled to be commissioned in 2018 and the entire project will be completed in 2020.

The Baihetan hydraulic power station will generate power by utilizing eighteen turbines, each with a generating capacity of 725 MW, totaling the generating capacity to 13,050 MW. In terms of generating capacity, it will be the fourth largest hydroelectric power plant in the world, after the Three Gorges Dam, Itaipu and Xiluodu Dam. In terms of dam volume, it is the third largest dam in China and the fourth in the world. The complicated underground cavern of the Baihetan hydropower plant is currently the world's largest underground rock cavern group under construction.

The Xiluodu project includes a dam, an underground power generation unit and a flood discharge structure. It is mainly developed for power generation, and sediment and flood

control while improving the downstream navigation of the river. The Xiluodu dam is a concrete double-curvature arch dam with 278m height and 700m width. It is the biggest arch dam over the world and the second largest hydropower project in China just after the Three Gorges Dam. The total generating capacity will be 13,860 MW. It is also expected to replace the consumption of 41MT of coal for electricity generation.

The Xiangjiaba Hydropower Project is the last step of the cascade development on the lower mainstream of Jinsha River. Apart from its main purpose of power generation, the Xiangjiaba Hydropower Project provides multiple benefits of flood control, navigation improvement and irrigation. It also plays the role of sediment trapping and counter regulation for the Xiluodu Hydropower Project. The concrete gravity dam has a crest elevation of 384m, a maximum height of 162m and a crest length of 896.26m. It has a total installed capacity of 6400 MW and an annual power output of 30.747TWh. The Xiangjiaba Hydropower Project has a normal storage level of 380m and a dead storage level of 370m. Its reservoir has the capacity of partial seasonal regulation with a total storage capacity of 5.163 billion cubic meters and a regulation capacity of 903 million cubic meters.



Figure 1.6 Xiluodu Hydropower Project under construction

As the largest power station in the world until now, the Three Gorges Project should be introduced in detail. The total electric generating capacity of the dam is about 22,5MW. In 2012, the amount of electricity production of the dam was similar to the amount generated by the Itaipu Dam, the second largest dam in the world. As well as producing electricity, the dam is designed to increase the shipping capacity of Yangtze River and to reduce the potential

floods downstream. The Three Gorges reservoir has created a buffer which mitigates the periodic floods in the Yangtzi Valley.



Figure 1.7 The bird view of the Three Gorges Projects

After the construction of the Three Gorges Dam, the water level of the Three Gorges reservoir fluctuates between 145 and 175 meters every year. It has destabilized the slopes of the Yangtzi Valley, and increased serious risks of erosion and landslides. More than 150 dangerous geological events were recorded within months after the reservoir was firstly impounded. Erosion affects slightly more than half the reservoir area, and 178 kilometers of riverbanks are in risk of collapsing. The landslide is now one of the main concerns of the hydraulic projects.

These hydraulic projects are mostly located in mountainous region with deep valley. The rock slopes are generally steep and high and evidently fractured. And certain slopes are usually excavated for the dam construction and the short-term stability guarantee. During the exploration stage of these hydraulic projects, the water level will increase remarkably with the impounding of the reservoir. Water leakage from the reservoir and the precipitation may considerably reduce the shear strength of the rock mass and more importantly of the rock joint. Therefore, the slope stability is influenced, especially for the long period in engineering lifetimes. So it is of great necessary to take this degradation into consideration when analyzing these jointed rock slopes in the reservoir regions.



Figure 1.8 A landslide in reservoir area

With a height of 262m, the Vajont Dam was one of the tallest arc dams in the world. It was accomplished in 1959 in the valley of the Vajont River under Monte Toc, 100 km north of Venice, Italy. From February 1960, the Vajont reservoir was put into work. Since the dam construction, the stability of the slopes in upstream was under strict monitoring, and some detectors were placed to observe the slope deformation and to detect out the potential landslide surface. In 1963 the deformation of left bank slope was observed dynamically varied with the water level of reservoir, hence the water level was manipulated carefully to avoid the instability of left bank slope. In October 1963, a heavy rainfall caused a great increase of reservoir water level in a very short time. On 9 October during the third reservoir emptying operation, the catastrophic landslide occurred and the whole rock mass collapsed into the reservoir in less than 45 seconds. The slide mass of a volume of approximately 270 million m³ generated a wave which crested 140 meters above the top of the dam and that still had a height of about 70 m downstream at the confluence of the valley. The wave arrived at the town of Longarone and other nearby villages and almost 2000 people lost their lives.

After the accident, many studies and researches were carried out in the aspects of geological and geomechanical. Several attempts were made to explain the kinematics and dynamics of the landslide, and back analysis is also applied to study the factors involved in the landslide development. In fact, a gravely fractured zone, extending about 1.5 km along the left side of the valley corresponding to the sliding plane of the prehistoric landslide, has been identified during the survey stage. Nevertheless, the designers of the dam concluded that a

deep-seated landslide was very unlikely to occur mainly because of both the asymmetric form of the syncline which was expected to act as a natural break on possible slope movements and the good quality of in situ rock masses as derived from seismic surveys.

As shown in Fig 1.9, it is now generally agreed that failure occurred along bands of clay within the limestone mass. With the water filling of the reservoir, the water level increases and the clay shear strength decreases. It is supposed that the total shear resistance of interlayers decreases progressively with the increase of water level, and the mass moves slowly towards the downstream under the effect of its own gravity as that reported by the in situ observation. Once the resistance attains its critical value, the disaster is unavoidable.

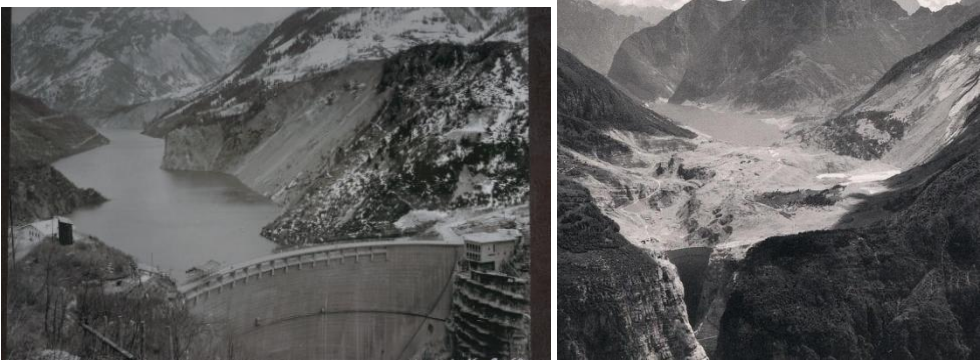


Figure 1.9 (a) The panorama of Vajont Dam before and after the disaster

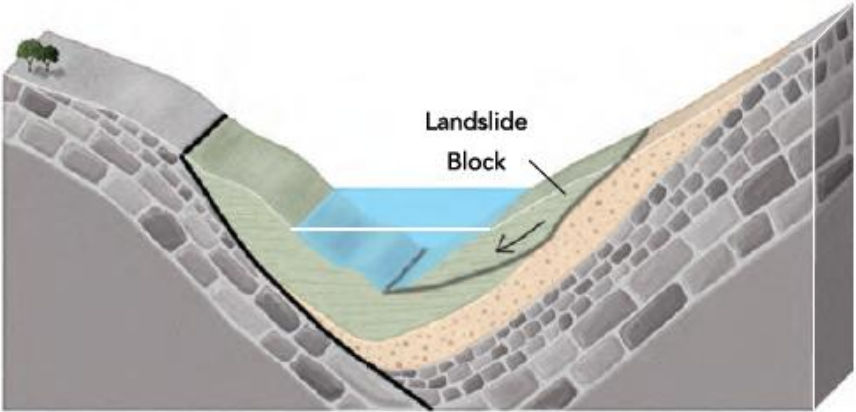


Figure 1.10 (b) Illustration of the interlayer (joint) of claystone in left bank of the reservoir where the landslide occurs

The occurrence of landslides is related to variations in external conditions[1]: rainfall, groundwater, earthquake and manual excavation. Besides that, internal conditions controls the factors include the local and regional morphological and lithological setting, the presence and abundance of geological discontinuities, including bedding planes, faults, joints, and cleavage systems, the type and depth of rocks, the extent and type of the vegetation cover, and the mechanical and hydrological properties of rocks [2, 3]. The weathering effect and time effect

reduce rock strength on the joint surface. They can also result in the instability of slope and increase landslide possibility.

The main internal factors that could influence the slope stability are discussed separately as below:

1) Property of rock matrix

The property of rock materials determines the mechanical behaviour of the whole slope, it related to the mechanical responses of structure under external loading, it is the foundation of sorts of material degradations (damage, weathering, etc.). The property of rock materials is certainly one basic factor affecting the slope stability.

2) Structural plane (crack, joint)

The stability of rock slope is decided not only by the property of rock material, but also by the rock structures. The presence of structural plane reduces the strength of the rock, increases the deformation properties of the rock mass, enhances rheological properties and other time effect of rock, and deepens the heterogeneity and anisotropic property of rock. A number of studies of rock slope accident showed that most of the landslides happen along one or several structural plane. Therefore, structural plane is an important issue in slope analysis, especially in long-term stability analysis

3) Weathering and erosion effect

Weathering is the breaking down of rocks, soil and minerals as well as artificial materials through contact with the Earth's atmosphere, biota and waters. It is also one frequently happened phenomenon in hydraulic structure slope. Two important classifications of weathering processes exist: physical and chemical weathering; each of them sometimes involves a biological component. Mechanical or physical weathering involves the breakdown of rocks and soils through direct contact with atmospheric conditions, such as heat, water, ice and pressure; the second classification, chemical weathering, involves the direct effect of atmospheric chemicals or biologically produced chemicals also known as biological weathering in the breakdown of rocks, soils and minerals[4].

The presence of water in hydraulic structure cannot be negligible when estimating the slope stability. Most slope accident were partly related to water presence, the physical and chemical effect caused by water can apparently expand the existing fissure in rock, enhance the weathering effect, and decrease the material properties.

4) Time effect

Some destruction and instability of rock do not happen immediately in the moment when the loading is taken place. With time passing, the stress and deformation state of rock also varies, and it would take a long period to arrive a stably state. This phenomenon is named

rheology. It is one important issue in analyzing long-term stability of slopes. The instantaneous mechanical response and material degradation (damage) of rock matrix, the influence of the existence and propagation of discontinuities and the time effect for both the rock matrix and rock joint are discussed in detail in this work.

1.2. Damage models for hard rock

The typical rock studied in the geoenvironment generally shows nonlinear mechanical response and irreversible behaviour. Generally, in geomaterials the dominant causes of irreversible deformations are plastic flow and damage process. The plastic flow is controlled by the presence of local shear stresses (deviatoric stress) which cause dislocation of some preferential elements due to existing defects. However, during this process, the elastic properties and the stiffness of the material are insensitive to the plastic flow. The main cause of irreversible changes in quasi-brittle materials, such as rock, is the damage process occurring within the material. From the viewpoint of microscopic, damage initiates with the nucleation and growth of microcracks. When the length of microcracks reaches a critical value, the coalescence of microcracks occurs and localized macrocracks appear. The macroscopic and phenomenological consequence of damage process is stiffness degradation, dilatation, softening and significant difference in tensile and compressive response.

Lots of researches have been carried out to study the mechanisms of damage evolution, *e.g.* the microcracks initiation and propagation in hard rock [5]. In fact, the evolution of the damage state in the hard rock during loading is accompanied by typical evolutions of various physical properties such as elastic stiffness, permeability, electric resistance, ultrasonic wave velocity and acoustic emissions [6]. Therefore, the damage determined in laboratory is generally based on these physical parameters.

Two typical microcrack evolutions are often mentioned, namely, the propagation of pre-existing cracks and the nucleation and the growth of new cracks [7]. Most of the microcracks observed in laboratory are tensile cracks even if in a compressive test. The absence of shear cracks in direct observations was explained by the possible closure of these cracks once the sample was unloaded [8] or by the fact that their thicknesses could not be observed by the technical devices used in these studies. Some authors [5, 8] have found that the total number and the total length of cracks increased with the deviatoric stress augmentation. However, the mean crack length was quasi-constant. Some researchers suggested that cracking evolution at low deviatoric stress is mostly the result of the initiation of new cracks. On the other hand, at higher stress levels the coalescence of cracks is suggested to occur in the direction of the

maximum principal stress. In contrast, Hadley [9] suggested that cracking evolution is mostly due to pre-existing crack propagation. Mode I tensile wing crack growth at the tips of sliding crack was often considered as a principal microscopic mechanism of pre-existing crack propagation [10]. For the damage during creep in hard rock, it is also an important issue from practical or theoretical viewpoint. In the case of hard rocks, experimental data have shown the development of volumetric creep deformation. This is essentially related to the sub-critical propagation of microcracks [10].

Based on the experimental observation, many criteria are proposed to describe the cracking evolution. For example, the cracking evolution in quasi-brittle rock samples undergoing a compression test could be monitored by measuring the Young's modulus. This is one of the most commonly cited evidence for inducing damage in the laboratory context because it is the simplest method to obtain through testing. It is sufficient to carry out unloading– reloading cycles test and measure the slope of strain-stress curves in order to assess the damage value.

Consequently, based on the fracture mechanics principles, the initiation, growth, opening, closure, friction, and interaction conditions of microcracks are studied and then damage evolution laws are proposed. The macroscopic behaviour of material is then obtained through a homogenization procedure. However, the micromechanical mechanism in numerical models, particularly in 3D models, is difficult to implement. Recently, some micromechanical models based on continuum damage mechanics are proposed [11-16] [17, 18].

In late 1970s, the continuum damage mechanics theory is applied to brittle material, such as rock and concrete. In the damage mechanics theory the continuum behaviour of a solid is studied within the framework of thermodynamic fundamental, internal state variables, degradation rule and damage yield function which do not consider interacting microcracks and infinitesimal deformations. The main advantage of continuum damage models is that the macroscopic constitutive equations they provide can be easily implemented and applied to the engineering analyses. The weakness of these models is that some of the concepts and parameters involved do not have clear physical explanations. Beside the isotropic models, anisotropic damage models were proposed by some authors [19-22]. Generally, the damage process has been described within the framework of principle thermodynamic. Most of these works employed a thermodynamic potential function, which is dissipative, and irreversible in their studies.

Description of failure processes in cohesive-frictional materials such as rock requires constitutive laws of strain softening, *i.e.* decrease of stress under increasing strain. If these constitutive laws are local, *i.e.* the stress state at a point depends uniquely on the strain history

at that point itself, strain softening leads to an ill-posed boundary value problem. A solution to the pathological mesh dependence is non-local constitutive laws [20, 23-28], for which the stress at one point depends on the strain history not only of that point but also of its neighborhoods or even of the entire body. In these models, a characteristic length is incorporated, which allows mesh-independent description of energy dissipation in a localized failure process. Typically, the deformations remain continuous even in the localized zone. For integral type non-local models, the interaction between neighboring points is taken into account by weighted spatial averaging. Such formulations were initially proposed in the context of elasticity and hardening plasticity, and they were applied as localization limiters for the first time by Pijaudier-Cabot and Bazant [29] in the context of damage mechanics.

1.3. Constitutive models for rock joint

Shear behaviour of a discontinuity plane is mainly controlled by its surface roughness. Surface roughness is an important factor to be evaluated in determining the stability of structures in jointed rock body. Several approaches can be adopted for the determination of surface roughness of discontinuities. Based on a series of direct shear tests of slight weathered rock joint in granite under constant normal stress, Johansson [30] has studied the basic friction angle and dilation angle, together with shear and normal stiffness. Woo [31] has conducted a series of direct shear tests on the porphyritic granite joints sampled from granitic rock slopes along a highway in the area of Jechon in South Korea, these samples were classified according to their initial weathering state and morphological conditions of the joint surface before direct shear tests. The experimental results showed that the joint compressive strength (JCS) can be reduced by 20-25% of the initial JCS value for a fresh joint wall by weathering processes and that the residual friction angle depends mainly on the weathering state of the joint surface. Rafek [32] presents a simple approach, in the form of two polynomial equations to correlate the peak friction angle with the Joint Roughness Coefficient (JRC) for discontinuity plane in fresh and slightly weathered schist. By using a three-dimensional (3D) image-processing technique, the roughness of naturally fractured rock joint surfaces is estimated by Mohd-Nordin [33]. The classification of the JRC is enhanced by introducing the scan line technique. The peak-to-valley height is selected as a key indicator for JRC classification. Meanwhile, the effects of degradation on the JRC have been also discussed. However, because of the lack of experimental data, the long-term behaviour of the joint concerning the weathering effects is still a difficult issue in joint analysis.

1.4. Numerical method for discontinuity simulation

Long-term mechanical behaviour of jointed rock mass is poorly studied in laboratory due to the limited condition of long-term observations and the complex degradation process of rock mass and its joints. The degradation includes several interactions among hydrogeological, mechanical, chemical and morphological processes. However, some numerical models are proposed to fill this blank.

With the efforts and advances made in recent years in both the numerical simulation methods and computational techniques, the jointed rocks can be simulated by various numerical methods. The finite element method, which has been widely used in the geoenvironment, has also been used to study the jointed rocks. For example, by using the FEM, Grasselli [34] has analyzed the 3D behaviour of bolted rock joints; Lacroix [35] has used the FEM for the long-term dynamics of rockslides and damage propagation analysis. The shortcoming of such method is evident, especially for the propagated cracks, the remeshing is needed.

Other methods, such as the boundary element method (BEM) [36], the discrete element method (DEM) [37], the numerical manifold method (NMM) [38] and the meshless methods [39], have been also widely used to simulate the jointed rock. In addition to the above numerical methods, the extended finite element method (XFEM) [40], which based on the theory of FEM, was widely used for predicting the behaviour of pre-existing crack and describing the crack initiation and propagation.

As the first method for analyzing crack growth without remeshing, the XFEM theory works by adding enrichment shape functions into the traditional FEM theory in the simulation of discontinuous in fixed meshes. In the numerical simulation of cracked structures under statically and later under dynamically loading, XFEM has been successfully applied for several years. It is now becoming an efficient method to reduce the mesh dependencies in macrocracks growth simulation. XFEM has been adopted in this work for the numerical simulation of discontinuous analysis in hard rocks, and both the pre-exist rock joints and crack propagation are considered.

1.5. Creep models for rock materials

As mentioned in previous section, because of the long work period which would during decades or even hundreds of years, for the high slopes in great hydraulic projects, besides the instantaneous mechanical behaviour, the creep phenomenon is another factor that cannot be negligible. Therefore, it is important to evaluate and to predict the long-term stability of

jointed rock slopes by taking into account of the mechanical degradation of rock joint. It is discussed as experimental part and numerical one.

1.5.1. Experimental research on the creep

The performance of creep experiments is an important part in analyzing creep phenomenon. Different test methods, using different loading methods in different environments would lead to different results. So the target should be very precise before the experiments.

Experiments of creep are performed early. In 1939, Griggs [41] firstly started the creep experiments of shale, limestone, siltstone and argillite. He concluded that the creep phenomenon can take place when the stress loaded arrive only 12.5%~80% of the material failure load, and impressed that creep curves by logarithmic function.

For soft rocks, with low strength, the creep phenomenon can easily take place, so lots of experiments are carried out in these materials. Haupt [42] analyzed the stress relaxation characteristic of salt rock, and pointed out that the micro-structure of salt rock can remain complete in the procedure of stress relaxation. E. Maranini and M. Brignoli [43] performed series of axial and triaxial creep experiments of limestone, and found that creep of that material is mainly because of fissure propagation under low confining pressure and the elimination of pores under high stress, and the creep phenomenon can the yield stress of limestone. Y. Fujii [44] performed triaxial creep experiments of Granite and sandstone, and pointed out that the circumferential strain can also be one important induce of material damage in these experiments. Gasc Barbier [45] started lots of triaxial creep experiments of argillite in different loading method and different temperature to see the influences of these two factors, in result, the strain and strain rate is proportional with deviatoric stress and temperature.

When dealing with the stability of rock slopes, in most situations, most part of rock slopes matrix is tended to be hard rocks. Comparing with soft rocks, hard rocks are not so sensitive in creep experiments. However, under high level of stress, creep phenomenon of some hard rocks is still very obvious. D.P. Singh [46] performed compress creep experiments of marble, and the curves obtained showed typical three stages of creep (primary stage, secondary stage and tertiary stage). Robert [34] focused on the fissure propagation in creep experiments of Granite. M. Ohnaka [47] studied acoustic emission characteristics in the process of brittle rock rheology. G. N. Boukharov [48] analyzed the creep phenomenon of brittle crystalline in experiments. Kazuhiko Miura [49] studied the prediction of creep failure

of hard rock for long-term safety of high-level radioactive waste disposal system. J. F. Shao [10] performed creep experiments with Granite of Lac du Bonnet.

1.5.2. Numerical models for creep simulation

In general, the creep constitutive models of rock can be classified into three distinct approaches, namely empirical models, component models, and mechanism-based creep constitutive models. The empirical models, which are based on experiments, need fewer parameters and thus have been widely used to predict creep deformation of rock [4]. The duration of an experimental study, however, is usually much shorter than a real engineering project. The difference in time scale between an experimental study and a real engineering project leads to an error between the predicted and measured creep deformations. On the other hand, the component models, which are based on a combination of standard elements such as the Newtonian dashpot, the Hooke spring and the frictional element, have the advantage of flexible description of different creep deformations [50-52], but the disadvantage of a mathematical complexity of a creep constitutive equation, result in difficulty in determination of parameters in component models. The mechanism-based creep constitutive model, as a distinct approach, focuses on the mechanical response such as cracking and damage growth at the micro-scale [49].

Many efforts have been directed toward the study on time-dependent behaviour of hard rocks and a variety of models have been proposed. Jin and Cristescu [53] suggested a new elastic/viscoplastic transient creep model based on triaxial experimental data. Yang [54] considered the effects of confining pressure and axial pressure on the time-dependent strain-stress behaviour and suggested an exponential function to characterize the creep strain from transient to steady-state creep of rock. By applying the concept of damage accelerating limit to the Carter creep model, Wang [55] presented a new constitutive creep-damage model to describe the third stage creep of rock. By introducing the concept of a damage accelerating limit to the Carter creep model, Wang [56] presented a new constitutive creep-damage model to describe the tertiary creep of salt rock. Mol-ladavoodi and Mortazavi [57] proposed a damage-based numerical analysis method for describing brittle rock failure mechanisms. Xie [58] presented a micromechanics-based elastoplastic damage model for quasi-brittle rocks under a compressive stress state with a proposed coulomb-type friction criterion based on the strain energy release rate. Although there have been many endeavors to investigate and construct a time-dependent damage constitutive model that can describe the time-dependent damage characteristics of rock masses and solve the time-dependent mechanics problems encountered in rock mechanics and engineering, the time-dependent damage characteristics

and yield strength's time-dependent evolution law of deeply buried hard rock are always investigated separately. It is not enough to accurately describe time-dependent damage characteristics of rock material, further investigations are required.

Many authors have proposed unified approaches for the modelling of instantaneous and long term damage of brittle rocks in which creep deformation is described as an extension of short term anisotropic damage by assuming a subcritical crack growth mechanism [59]. Although all authors tend to concur that both the propagation of pre-existing cracks and nucleation and the growth of new cracks could be presented in rocks under loading, the results of direct microscopic observations on natural rock do not give a clear view of the role of each mechanism.

1.6. The main contents of the thesis

Based on the theoretical and experimental investigations, the basic mechanical behaviour of the rock matrix in long term under the quasi static mechanical loads could be characterized as the damage due to the initiation and propagation of microcracks in the rock. In this thesis, similar with the visco-plastic model, a damage model is proposed for describing the mechanical behaviour of rock matrix. While for the fracture in the rock, an empirical constitutive law relating stress and displacement has been proposed. The value of the peak-shear strength is expressed as a function of the material strength, the load conditions, the basic friction angle and the morphological description of the surface. The most important aspect of this model is the introduction of quantitative time-dependent degradation of the surface morphology. Based on XFEM, the two models have been implemented into a numerical calculation code. And then several numerical examples have been studied.

The thesis is organized as below:

Chapter 2 mainly introduces an elasto-damage model which considers the influence of confining pressure, and this model is also applied to some experimental results. Non-local method is employed in this chapter to solve the mesh dependency problem.

In chapter 3, numerical models are presented to describe the mechanical response of rock joint respectively under normal traction, normal compression and shear stress under constant normal stress. And then the shear model is improved to consider the time effect. Numerical tests have been conducted to test the model with the experimental results.

In chapter 4, the extended finite element method (XFEM) is briefly introduced. And then the numerical implementation techniques are discussed. Based on physical analysis, a crack initiation criterion which based on the critical damage has been proposed and illustrated by a

simple example. The crack propagation direction is determined by the average criterion. The influence of joint incline angle is analyzed by a simple pre-cracked rock mass.

In the last, chapter 5, the whole proposed numerical model is used to investigate the long term stability of a jointed rock slope in a large scale hydraulic project. In this simulation, the main external loading affects the mechanical degradation of rock joints is gravity, three typical joints with different incline angles and geometrical position are investigated. The numerical results have been interpreted and discussed.

Chapter 2. Time-dependent elasto-damage constitutive model for hard rock

2.1. Introduction

The physical mechanism of material failure of rock and concrete is generally due to the nucleation and propagation of microcracks. For example in concrete, because of the heterogeneity, *i.e.* the different stiffness of granular and cement paste, under the mechanical or other solicitations, the microcracks are generally observed firstly at the interfaces of aggregates and cement paste matrix. With the increase of the solicitation, the density of the microcracks increases. Furthermore, the existing microcracks will propagate and nucleate. The propagate orientation of microcrack usually geometrically depends on the loading history. Under different solicitations it would be opened, propagated or closed. The influence of closed crack is generally different from that of opened crack. However, for the sake of simplicity and in view of numerical implementation for engineering applications, an isotropic damage state is assumed and a scalar damage model which does not account for directionality of microcracks is adopted in this section.

In isotropic models, it is assumed that the microcracks distribute randomly in space. The scalar damage variable can be physically identified as a microcrack density defined as $\omega = Na^3 / \Omega$ [60], where ω the damage effect caused by the microcracks, Ω stands for representative volume element, N the number of microcracks which supposed have a penny shape with radius of a .

However, it is well known that the mechanical behaviour of geomaterials depends on the mechanical stress state and loading history. There is a strong difference between the responses under tensile and compression. This difference is directly related to the microcrack opening state. Under a tensile stress, the microcracks are opening and probably propagate. In compression, the microcracks are generally closed and their propagation is associated with the sliding friction along microcrack surfaces. The kinetics of damage is therefore different in compression and tension. So even in isotropic model, the damage in traction and in compression state should be clearly distinguished.

With the further increase in the solicitation, the material attains the failure stage. The macroscopic failure usually occurs as the result of coalescence of microcracks, and leads to the formation of macroscopic cracks, *i.e.* the localization of deformation, therefore the diffuse damage is the precursor of macroscopic failure. However, in the framework of "the mechanics

of continuous medium", such phenomena will cause certain problems. The localization corresponds to the occurrence of bifurcation, and leads to the appearance and development of a band of discontinuity of the strain rate. When such a solution is possible, strains and damage concentrate into a zone of zero volume, and the energy dissipation in a finite volume of material tends to zero. However, this is physically incorrect [61]. For such ill posed problem, in the framework of numerical simulation using the finite element method (FEM), the results are generally mesh-dependent.

Various methods are proposed to solve this problem. The basic idea is to incorporate a length, the so-called "internal length", into the constitutive relation to avoid localization in a region of zero volume. The "internal length" controls the size of the region in which damage may localize. In the "non-local damage model", this length is incorporated in the variable which controls damage growth with a spatial average of the local equivalent strain.

When rock and concrete subjected to a constant stress, *i.e.* in creep conditions, they deform at a strain rate variable with time. The study of the fracture and deformation of rocks under creep is necessary for better analyze the behaviour of geological structures, such as landslides, rock massifs, and faults, which are subjected to a long-term loading. Three regimes are usually observed during creep experiments: primary creep (decreasing strain rate), secondary creep (constant strain rate), when under large enough stress, tertiary creep (increasing strain rate), and finally, ending by failure. During primary creep, the strain rate usually decreases as a power-law of the time since the stress change. The strain rate during secondary creep is nearly constant, and strongly depends on the applied stress. The secondary creep regime is not always clearly observed. In some cases, there is rather a cross-over between decaying primary creep and accelerating tertiary creep than a purely stationary regime. During tertiary creep stage, similar power-law accelerations of either strain rate acoustic emission rate before rupture have also been observed in natural structures such as landslides [62]. Experimental observations, such as an increase of dilatancy and hydraulic permeability, a decrease of elastic modulus, and the recording of acoustic emission, attest that crack propagation is acting during creep [63].

In this chapter, the formulation of an elasto-damage model for hard rock is firstly presented. In presented isotropic damage model, the damages in traction and in compression state have been clearly distinguished. Moreover, the influence of the confining pressure has also been taken into consideration, and then the mesh dependent problem with the damage model has been discussed, the "non-local" method has been adopted to resolve this problem. Finally, the proposed model has been extended to consider the time effects under constant stress states and has been verified and validated by simulating several laboratory tests.

2.2. Formulation of damage model for instantaneous mechanical behaviour

The damage evolution depends on loading path. In both traction and compression states, the damage effects have been observed but with different evolutions. Therefore, it is necessary to distinguish the damage caused by traction from that by compression. Based on the works of Mazars [64] the total damage ω could be decomposed into two parts: a tensile part ω_t and a compressive part ω_c as:

$$\omega = (1 - \alpha_t)\omega_c + \alpha_t\omega_t \quad (2.0)$$

in which the combination coefficient α_t depends on the stress state. It is determined as following:

$$\alpha_t = \frac{\|\bar{\underline{\sigma}}^+\|}{\|\bar{\underline{\sigma}}\|} \quad (2.0)$$

$\bar{\underline{\sigma}}^+$ is the positive part of the current stress tensor. $\|\bar{x}\|$ represents the norm of tensor \bar{x} . To determine the actual mechanical properties of the damaged material, the existence of a thermodynamic potential is assumed. In this case, the free energy is described as the general form which is widely applied for geomaterials:

$$\psi(\underline{\underline{\varepsilon}}, \omega) = \frac{1}{2} \left[K(\omega) \text{tr}(\underline{\underline{\varepsilon}})^2 + 2G(\omega) \underline{\underline{e}} : \underline{\underline{e}} \right] \text{ with } \underline{\underline{e}} = \underline{\underline{\varepsilon}} - \frac{\text{tr}(\underline{\underline{\varepsilon}})}{3} \underline{\underline{\delta}} \quad (2.0)$$

where $\underline{\underline{\varepsilon}}$ represents the total strain tensor while $\underline{\underline{e}}$ denotes the deviatoric strain tensor. $\underline{\underline{\delta}}$ is the second order unit tensor. tr represents the trace operator. The specific forms of the two functions $K(\omega)$ and $G(\omega)$, are respectively the bulk modulus and shear modulus of material in function of damage, which should be determined from relevant experimental data. For the reason of simplicity, the following linear functions are proposed to describe the degradation caused by damage of the two elastic moduli:

$$K(\omega) = K_0(1 - \omega), \quad G(\omega) = G_0(1 - \omega) \quad (2.0)$$

In these equations, K_0 and G_0 are respectively the initial bulk and shear moduli in undamaged state. These forms are equivalent to that proposed by the classical Lemaitre's model [65] for metal materials and by Mazars' model [64] which is widely used for geomaterials, such as concrete. In this case, only Young's modulus is affected by damage, e.g. $E(\omega) = E_0(1 - \omega)$, while the Poisson ratio remains constant.

The stress-strain relation of damaged material is derived directly from the free energy function used as the thermodynamics potential:

$$\underline{\underline{\sigma}} = \frac{\partial \psi(\underline{\underline{\varepsilon}}, \omega)}{\partial \underline{\underline{\varepsilon}}} = K(\omega) \text{tr}(\underline{\underline{\varepsilon}}) \underline{\underline{\delta}} + 2G(\omega) \underline{\underline{e}} \quad (2.0)$$

The conjugate thermodynamic force associated with the damage variable is deduced from the free energy function:

$$F_d = -\frac{\partial \psi(\underline{\underline{\varepsilon}}, \omega)}{\partial \omega} \quad (2.0)$$

In the framework of irreversible thermodynamics, the damage evolution is determined by an appropriate damage criterion which is a function of damage conjugate forces given in(2.0). However, in practice, the experimental determination of such damage criterion is complex. Some physics-based approaches are generally preferred. For hard rock, it is well known that the damage induced by microcracks in traction state is inherently related to the tensile strains [64-66]. Therefore, by considering such effects, the following equivalent tensile strain is defined for damage in traction state:

$$\varepsilon_{eq}^t = 2\sqrt{\sum_{i=1}^3 \langle \varepsilon_i \rangle^2} \quad (2.0)$$

in which ε_i denotes the principal strains. The bracket $\langle x \rangle$ means that only the positive value will be taken into consideration, as:

$$\begin{cases} \langle x \rangle = 0 & \text{if } x \leq 0 \\ \langle x \rangle = x & \text{if } x > 0 \end{cases} \quad (2.0)$$

While in compression state, the damage evolution is generally related with the equivalent deviatoric strain, which is given directly as:

$$\varepsilon_{eq}^c = \sqrt{\frac{2}{3} e_{ij} e_{ij}} \quad (2.0)$$

However, unlike that in traction state, the influence of confining pressure could not be neglected in the compression state. With the increase of the confining pressure, the propagation of existed microcracks become more and more difficult; most "opened" microcracks closed progressively; the probability of the initiation of "new microcrack" decrease. As a result, the material transfers from "brittle material" to "ductile material". For taking such effects into consideration, we proposed to modify the equivalent strain in compression state (2.0) as follows:

$$\varepsilon_{eq}^c = \sqrt{\frac{2}{3} e_{ij} e_{ij}} - \varepsilon_v^n \quad (2.0)$$

in which ε_v is the volumetric strain in compression state, as:

$$\varepsilon_v = \varepsilon_{xx} + \varepsilon_{yy} + \varepsilon_{zz} \quad \text{and} \quad \varepsilon_v \leq 0 \quad (2.0)$$

While the parameter n controls the influence of volumetric strain on the compression damage evolution.

The conjugated damage driving force is then defined, respectively for that in traction state and compression state, as:

$$Y_{dt} = \max(\varepsilon_{eq}^t, Y_{this}) \quad (2.0)$$

$$Y_{dc} = \max(\varepsilon_{eq}^c, Y_{chis}) \quad (2.0)$$

with Y_{this} and Y_{chis} are the maximum values of Y_{dt} and Y_{dc} reached in the previous loading history, these two variables assure the irreversibility of the damage effects in both traction state and compression state.

The evolution of each damage component (traction and compression) can be expressed as the function of the conjugated damaged force Y_{dt} and Y_{dc} . For most geomaterials, the following exponential forms are adopted for the descriptions of damage evolution:

$$\omega_c = A_c - \frac{A_c}{\exp[B_c(Y_{dc} - Y_{c0})]} \quad (2.0)$$

$$\omega_t = A_t - \frac{A_t}{\exp[B_t(Y_{dt} - Y_{t0})]} \quad (2.0)$$

In the above equations, A_c and A_t represent respectively the critical value of damage corresponding to residual strength of damaged material in compression and traction. For the reason of simplify, the two parameters are usually set as unit. B_c and B_t control the kinetics of damage evaluation in compression state and traction state, respectively. Y_{c0} and Y_{t0} define the initial threshold of damage force. Note that the proposed damage criterion is similar to that proposed by Mazars [64].

2.3. Identification of model parameters

For the proposed elasto-damage model, there are only 7 parameters including two basic isotropic elastic parameters, they are listed as in the follows:

E : Yong's modulus of undamaged material;

ν : Poisson ratio;

B_c : The parameter controls the kinetics of damage in compression;

B_t : The parameter controls the kinetics of damage in traction;

Y_{c0} : The threshold for damage in compression;

Y_{t0} : The threshold for damage in traction;

n : The parameter controls the influence of confining pressure on the compression damage evolution.

The Young's modulus and Poisson's ratio could be measured directly from a uniaxial compression test. A uniaxial tensile test and a uniaxial compression test could provide the parameters which are related to the damage evolution in traction and compression, respectively. The parameter n is determined by the best fitting of the responses of the material under triaxial compression test. Because the damage evaluations in traction and in compression are clearly distinguished and controlled by different driving forces, the mechanical behaviour of hard rock in compression and in traction could be reproduced, as shown in Fig. 2.1.

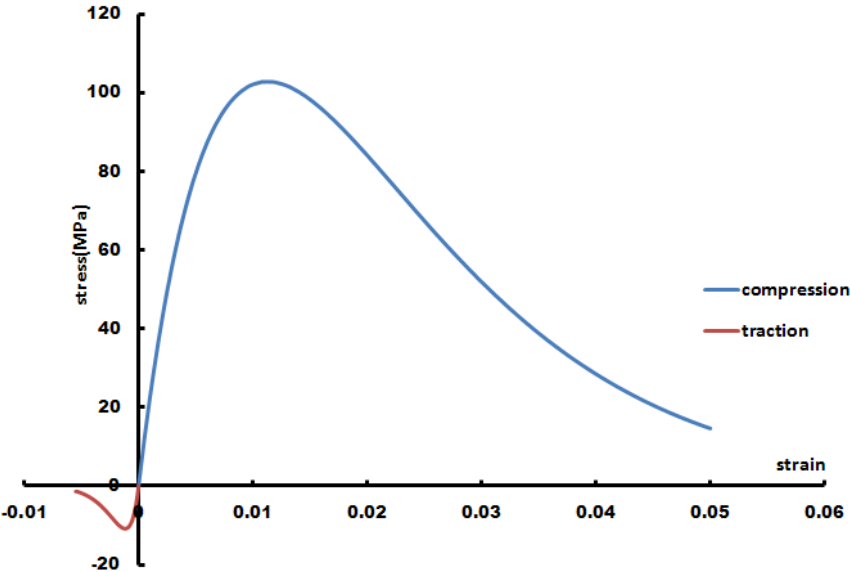


Figure 2.1 Typical stress-strain curve of the hard rock under uniaxial compression and traction

In case of the rock slope stability, compression is the most usually encountered stress state, therefore, according to equation(2.0), the combination coefficient α_i is always zero. Only the damage in compression will be taken into consideration and B_c , Y_{c0} and n are the most important parameters should be determined. The representative value for a typical marble is given in Tab. 2.1. Based on these determined parameters, the parametric study has been done for the latter 3 parameters B_c , Y_{c0} and n , as shown in Fig. 2.2-2.4.

Table 2.1 Basic parameters for a typical Marble

E (GPa)	ν	B_c	Y_{c0}	n
20	0.25	100	0	1

The parameter B_c controls the kinematic of damage in compression, as shown in Fig. 2.2. With the same axial deformation, which means the same equivalent deviatoric strain as given by equation(2.0), the damage is more important for a greater B_c . According to equation(2.0), the peak value of stress depends on only the damage. As consequence, with a bigger value of

B_c , the peak value of the stress will be smaller, as compared in Fig. 2.2. From the strain-stress curve, it can be seen that, the parameter B_c has significant influence of the curvature of the strain-stress curve.

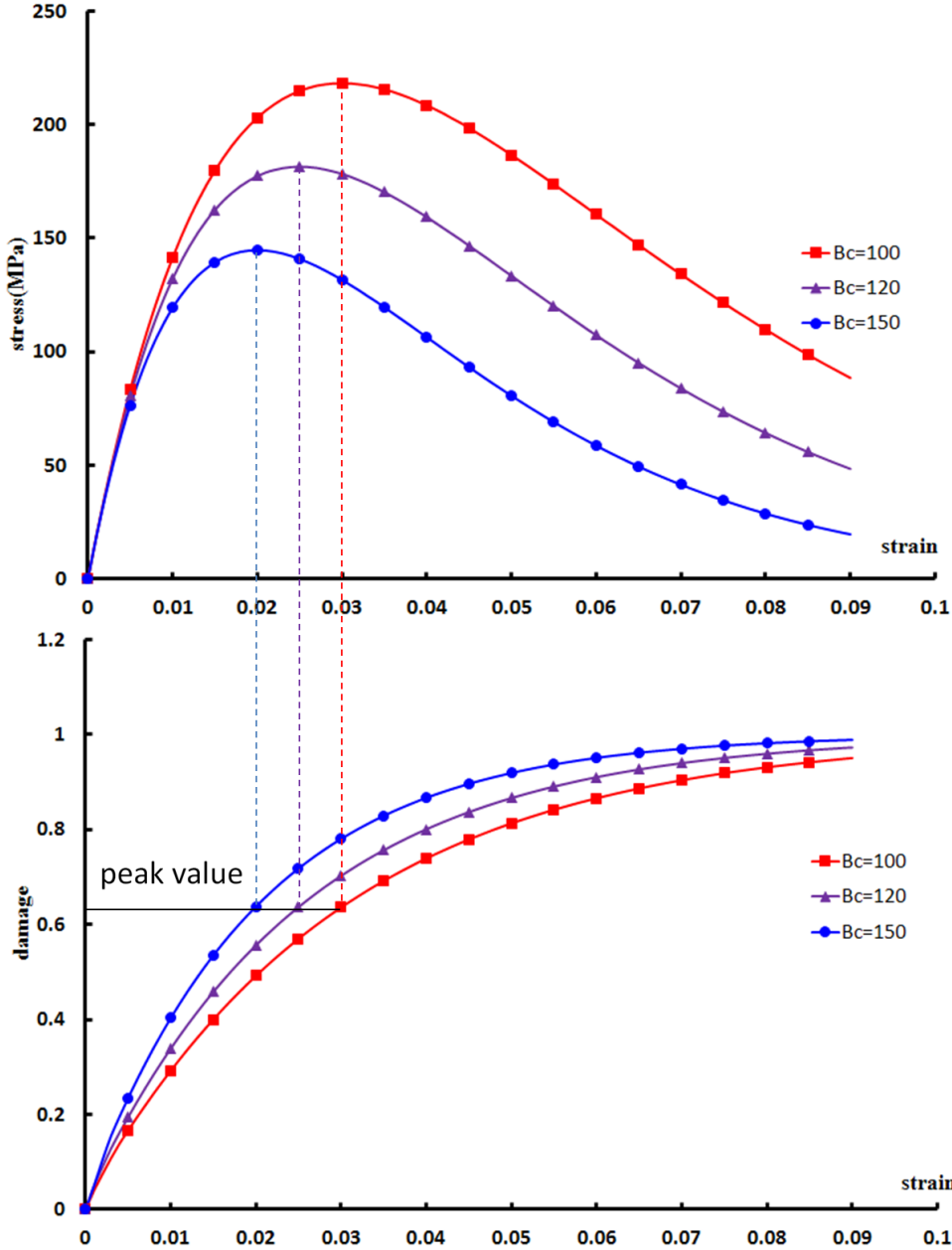


Figure 2.2 Influence of parameter B_c on the stress-strain and damage-strain curve

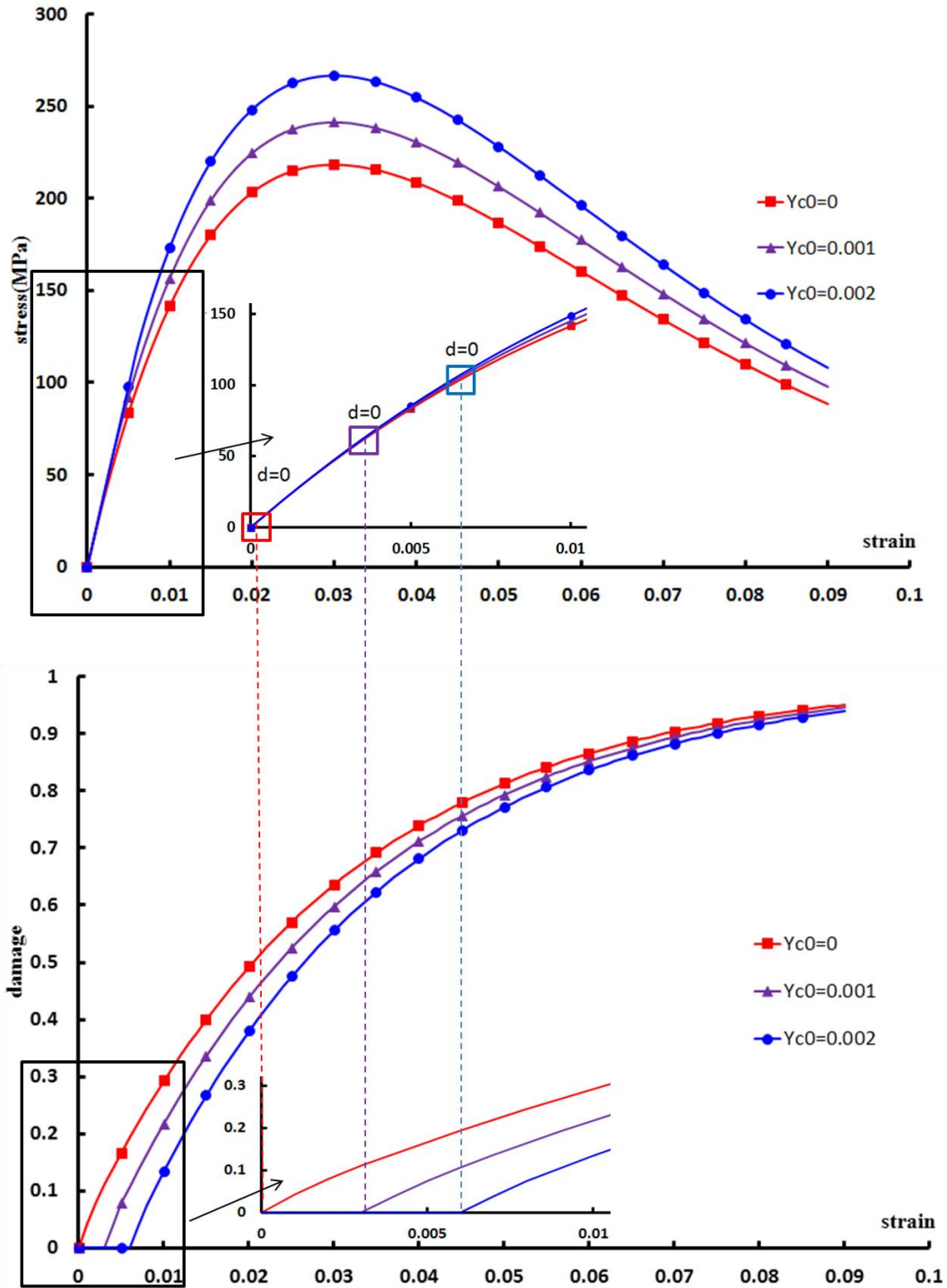
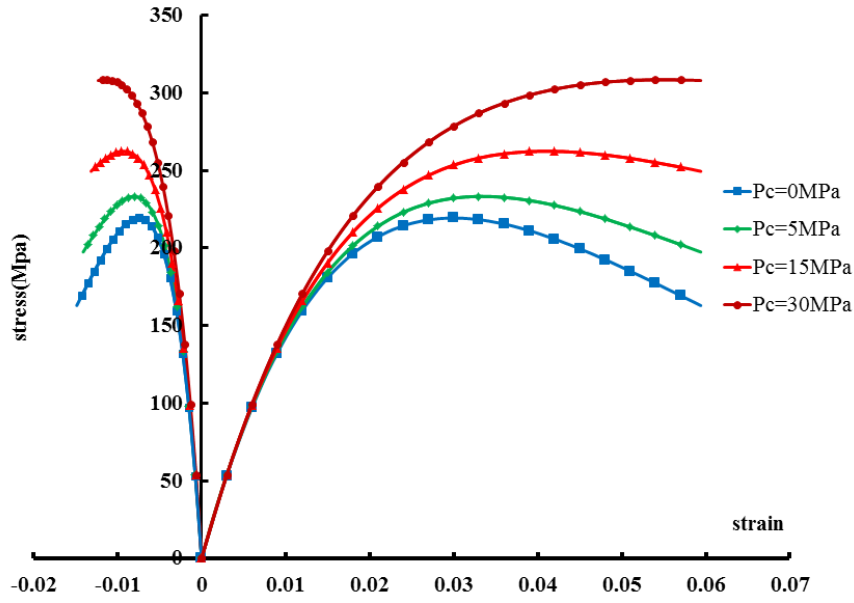
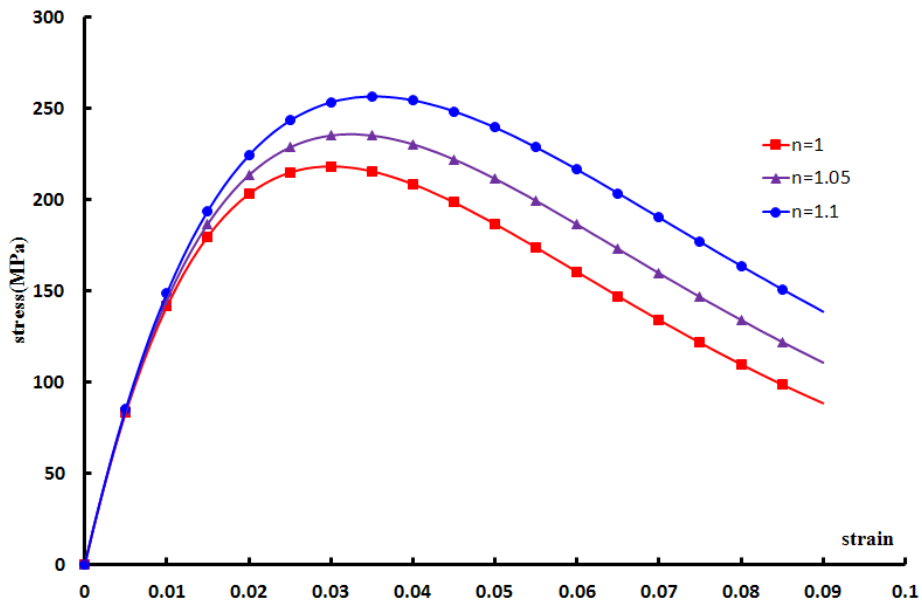


Figure 2.3 Influence of parameter Y_{c0} on the stress-strain and damage-strain curve

An important innovation in current model is that the effects of confining pressure has been taking into consideration, as shown in Fig. 2.4 (a), three tests are performed with the same parameter under different confining pressure for a typical hard rock. It can be seen that the main features of the rock in triaxial tests have been captured: the increase of the deviatoric stress with the increase of confining pressure, and the transition from brittle material to ductile material.



(a) Influence of confining pressure on the stress-strain curve



(b) Influence of parameter n on the stress-strain curve

Figure 2.4 Influence of confining pressure and parameter n

The parameter n controls the contribution of the “confining pressure”, *i.e.* the volumetric strain in compression. In fact, from equation(2.0), we can see that, the effects of parameter n are similar to that of Y_{c0} . However, as shown in Fig. 2.4 (b), the big difference is that, the parameter Y_{c0} is constant, while the effects of the volumetric strain increases during the entire loading path.

2.4. Numerical simulation of laboratory tests

The proposed model has been programmed and implemented in the calculation code. According to the formulations in section 2.2, a big advantage of the proposed model is that the damage could be determined implicitly from the deformation. The stress at each integration point needs no correction and can be calculated directly with current damage. The flow chart of the proposed model has been given in Figure 2.5.

Because in the latter work, the hard rocks, such as marbles and meta-sandstones, are the material encountered in slope analysis, the proposed model has been used firstly to simulate the laboratory tests on these rocks: on one hand, for the determination and verification of model parameters; on the other hand, for the verification of the proposed model. The experimental data for marble are from the thesis of Yang [67], and the sandstone data applied in the works are from Meng [68].

2.4.1. Numerical simulations of triaxial tests of Marble

Marble is a non-foliated metamorphic rock composed of recrystallized carbonate minerals, most commonly calcite or dolomite. Marble is widespread used as a building material and is frequently encountered in the nature rock slopes. Five groups of experiments are chosen for the numerical simulations. The experimental data for these five groups tests are from the thesis of Yang [67]. The experiments are realized at Hohai University. For the first 2 groups, the rocks are the marble rock with “fine-particle”, while for the third group, it is the marble with “medium-particle” and for the two last groups, they are marble with “coarse-particle”. The model parameters for these 5 group tests are listed in Table 2.2. It can be seen that, the mechanical behaviour is quite different for these marbles. That may be explained by the different microstructures of these rocks. It is worth mentioned that, for each group, different confining pressures have been used for the tests, however, the model parameters are the same for these confining pressure. As illustrated in the Fig 2.6-2.10, the numerical results are compared with the experimental data. Globally, the numerical results have a good concordance with experimental results.

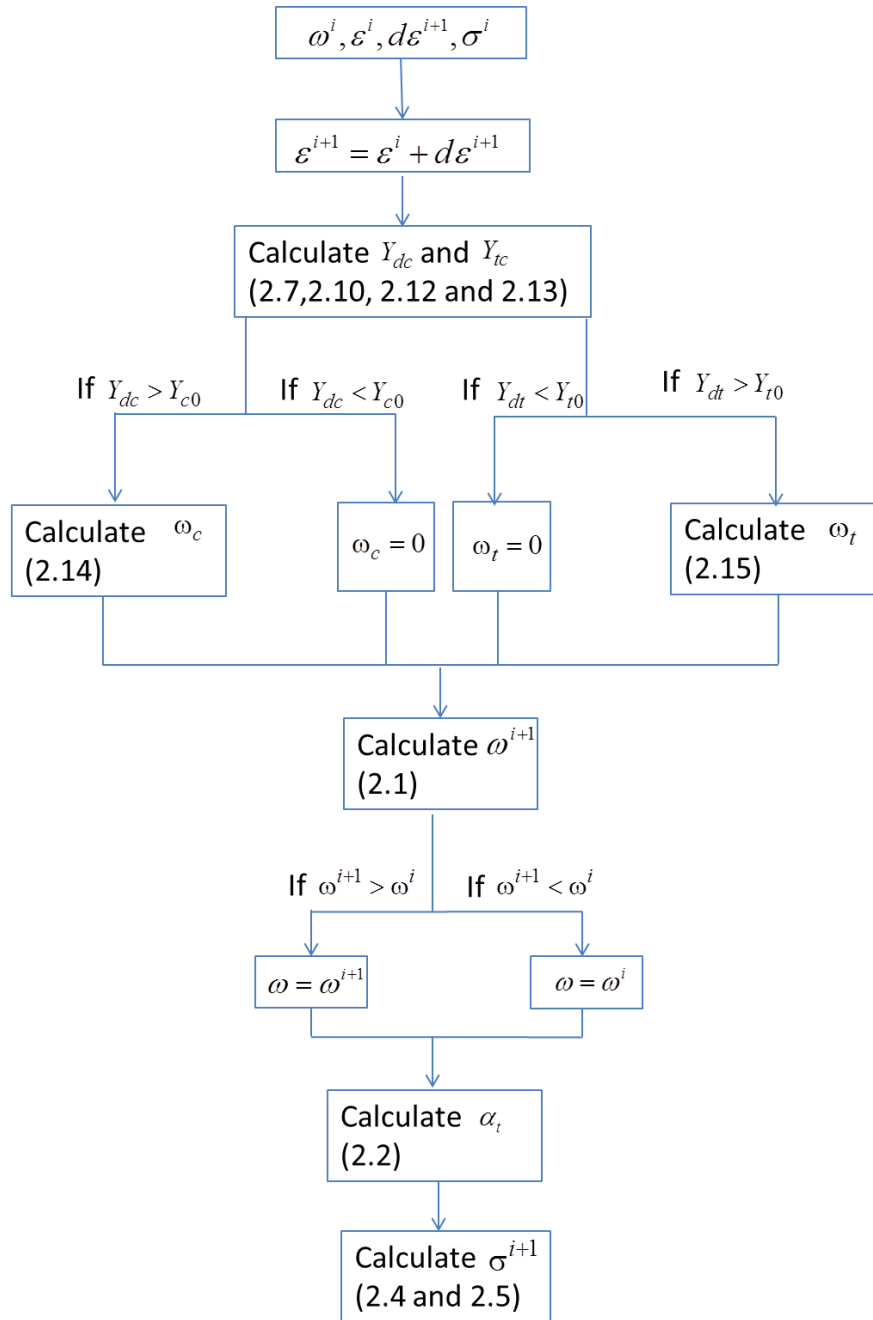


Figure 2.5 Flow chart of the elasto-damage model for instantaneous mechanical behaviour

Table 2.2 Parameters used for 5 groups of Marble rock

Group	E(Gpa)	ν	B_c	Y_{c0}	n
1	50	0.25	850	3.00E-04	1.05
2	50	0.25	900	3.00E-04	1.02
3	50	0.25	600	9.00E-04	1.01
4	35	0.25	450	3.00E-04	1.08
5	25	0.25	800	3.00E-04	0.95

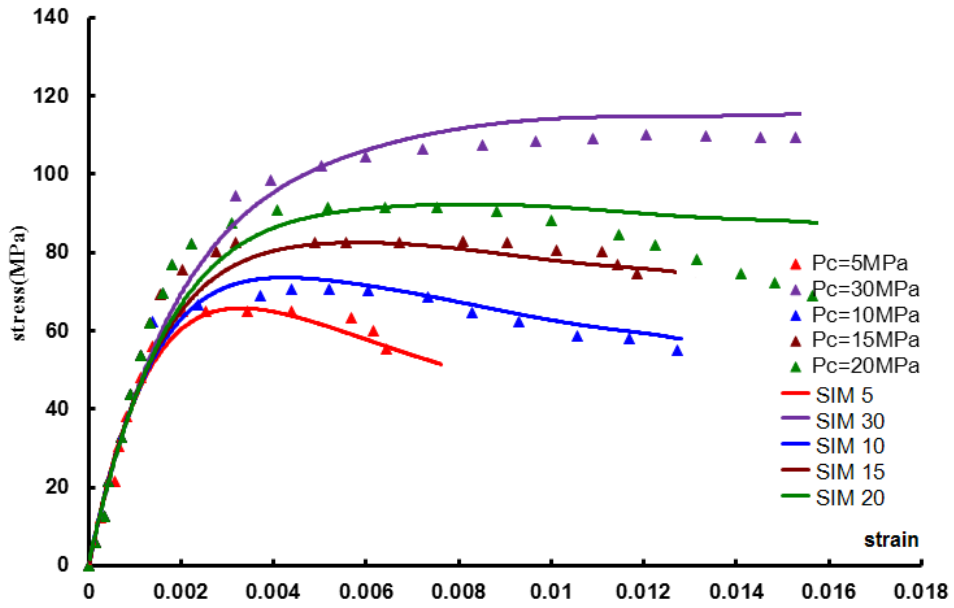


Figure 2.6 Numerical simulations of the triaxial tests of group 1 of marble

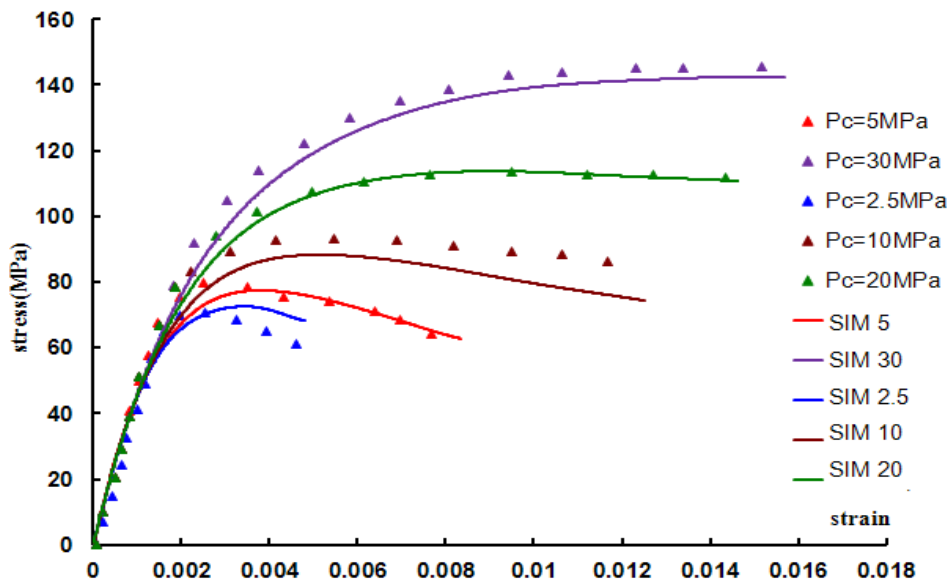


Figure 2.7 Numerical simulations of the triaxial tests of group 2 of marble

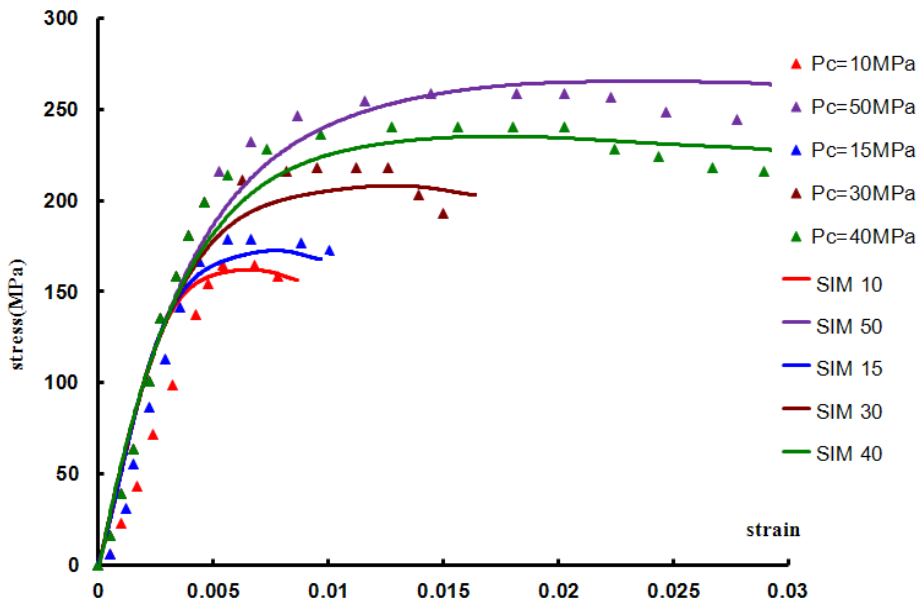


Figure 2.8 Numerical simulations of the triaxial tests of group 3 of marble

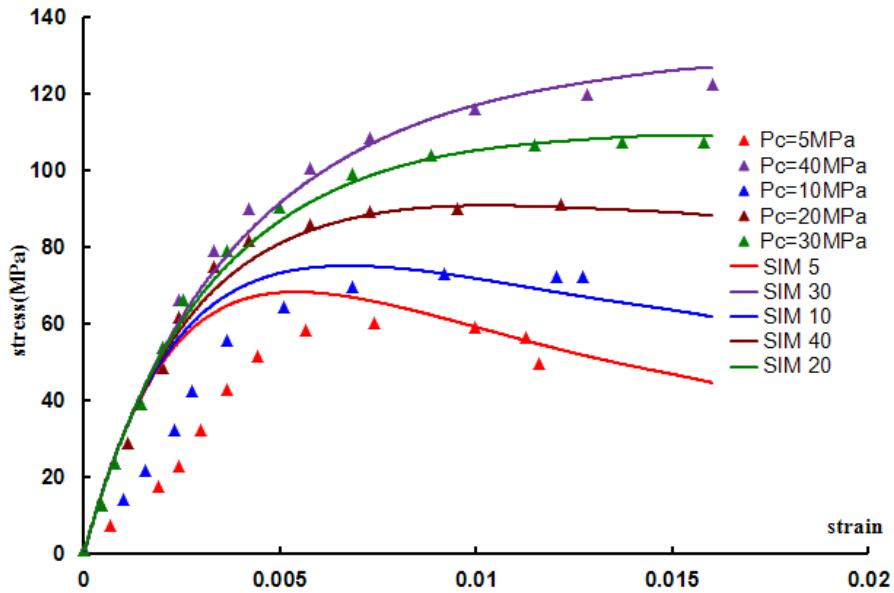


Figure 2.9 Numerical simulations of the triaxial tests of group 4 of marble

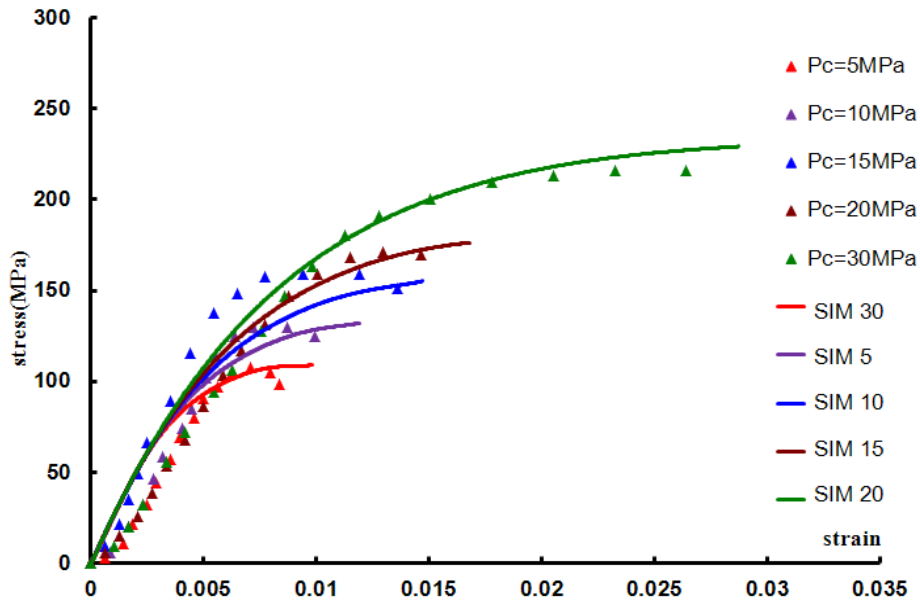


Figure 2.10 Numerical simulations of the triaxial tests of group 5 of marble

2.4.2. Numerical simulations of triaxial tests of Meta-sandstone

Meta-sandstones are also frequently encountered rock in the geoen지니어ing. However, the microstructure of meta-sandstones is more complicated than that of marble rock. The experimental data are taking from Meng [68]. The experimental results seem a little scatter, so only three groups of tests with the specimens from different locations are simulated. The model parameters are listed in Table 3. For each group, three different confining pressures (10MPa, 30MPa and 50MPa) are used. As that for marble rock, the parameters are the same for the three confining pressures. The numerical results are compared with the experimental data in the Fig 2.11 and Fig 2.12 respectively for group 1 and 2. Even the experimental data has an important dispersion, the numerical results reproduce well the tendency of mechanical behaviour of the meta-sandstone.

Table 2.3 Parameters used for 2 groups of Meta-Sandstone

Group	E (Gpa)	ν	B_c	Y_{c0}	n
1	18	0.25	250	1.00E-03	1.18
2	50	0.25	1050	3.00E-04	0.97

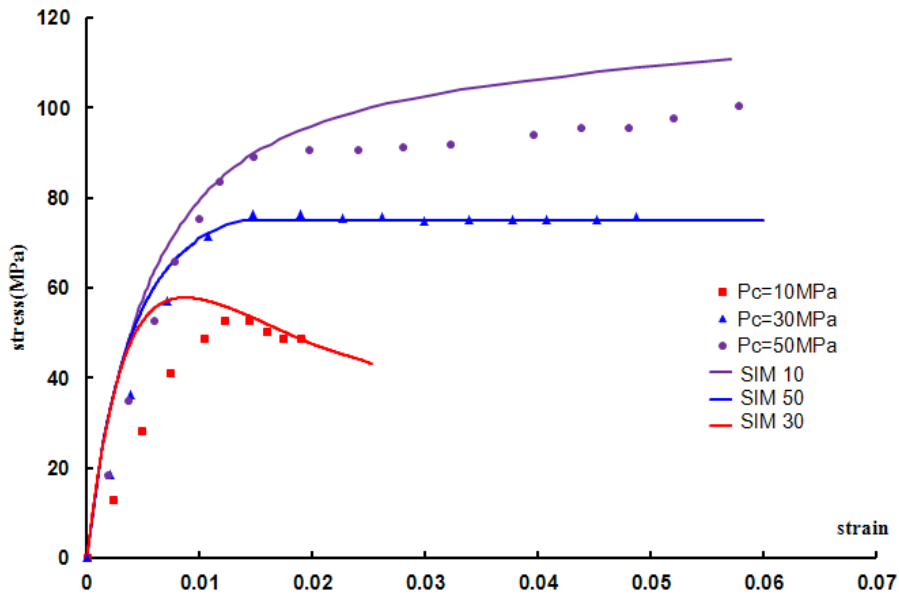


Figure 2.11 Numerical simulations of the triaxial tests of group 1 of Meta-sandstone

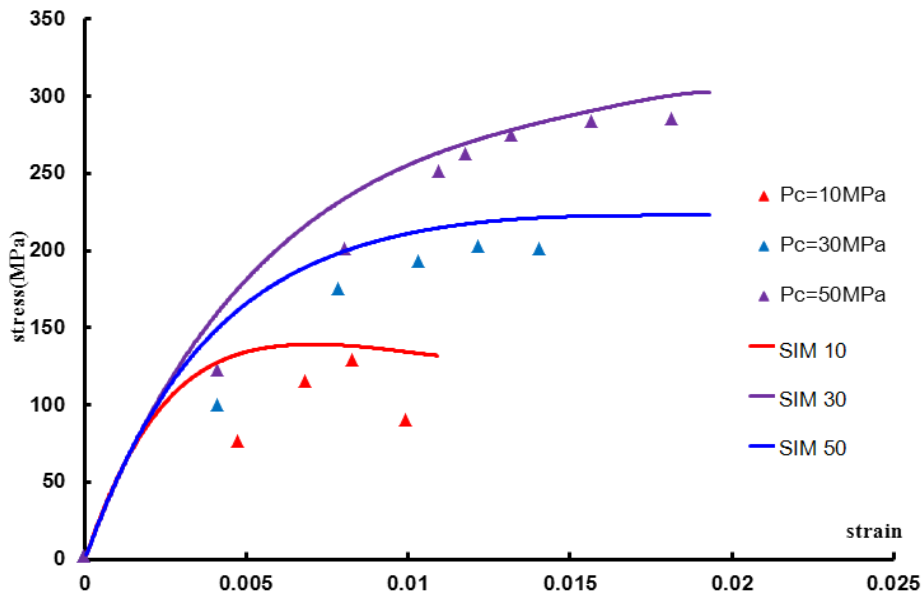


Figure 2.12 Numerical simulations of the triaxial tests of group 2 of Meta-sandstone

2.5. Non-local form of proposed damage model

With the damage model, after the stress attains its peak value, the deformation begins to localize to form a band and the numerical results will be “mesh dependent”. In this section, the mesh dependent problem is analysed. As shown in Fig. 2.13, a simple beam with a length of 10cm, while the height of 1cm, under a compression load has been studied. The boundary conditions are: a prescribed zero horizontal displacement is applied at the left side; while the vertical displacement at the bottom of beam has been blocked; at the right side, a prescribed

horizontal displacement of -0.01cm has been applied. For the configuration illustrated in Fig. 2.13, when the damage model proposed in Section 2.2 has been used, the distribution of damage is uniform. For the localisation of deformation, two different materials are used, as shown in Fig. 2.13, at the centre of the beam, a “weaker” material is used, with width as 1cm.

The elasto-damage model of section 2.2 is employed for these two materials. As the model parameters listed in Tab. 2.4, the only difference between the two materials is the Young’s modulus. Three different meshes, respectively with 11 elements, 22 elements, 44 elements are used for the numerical simulations as shown in Fig. 2.14.

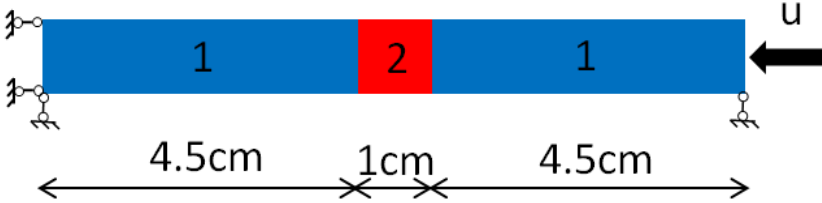


Figure 2.13 Simple beam model under uniaxial compression controlled by displacement

Table 2.4 Model parameters for two materials

Material	E (GPa)	ν	B_c	Y_{c0}
1	25	0.2	800	0
2	22	0.2	800	0

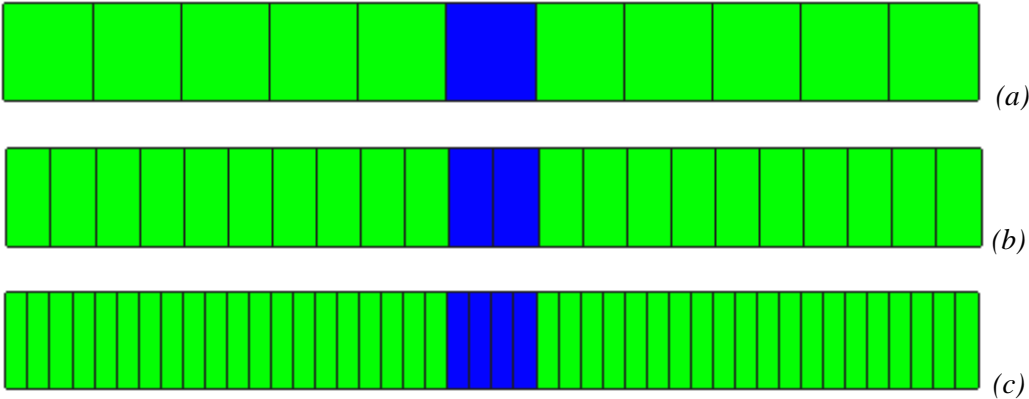


Figure 2.14 Three meshes with different element densities
(a) 11elements; (b) 22elements; (c) 44elements.

The damage distributions at the end of calculation for the three different meshes are given in Figure 2.15 and 2.16. In fact, for the three calculations: the geometry, the boundary conditions, the constitutive model and its parameters are the same. The only difference is the mesh density. From the results, we can see that the mesh density has a big influence on the

results. With the increase of the mesh density, the width of the band of damage decreases and the peak value of the damage increases. It is evident that the results are mesh dependent.

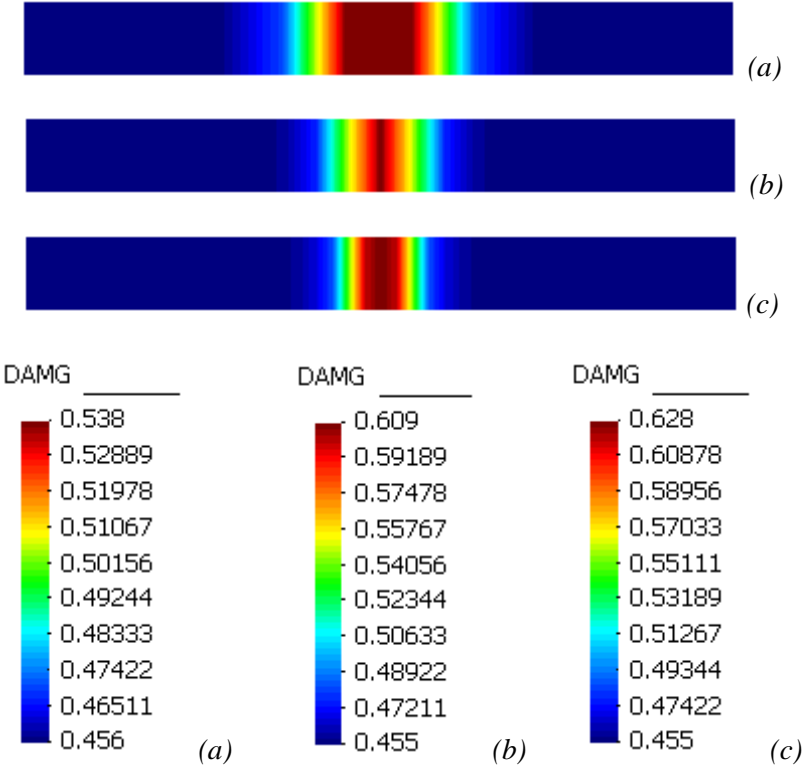


Figure 2.15 The distribution of Damage for three different meshes
(a) 11 elements; (b) 22 elements; (c) 44 elements

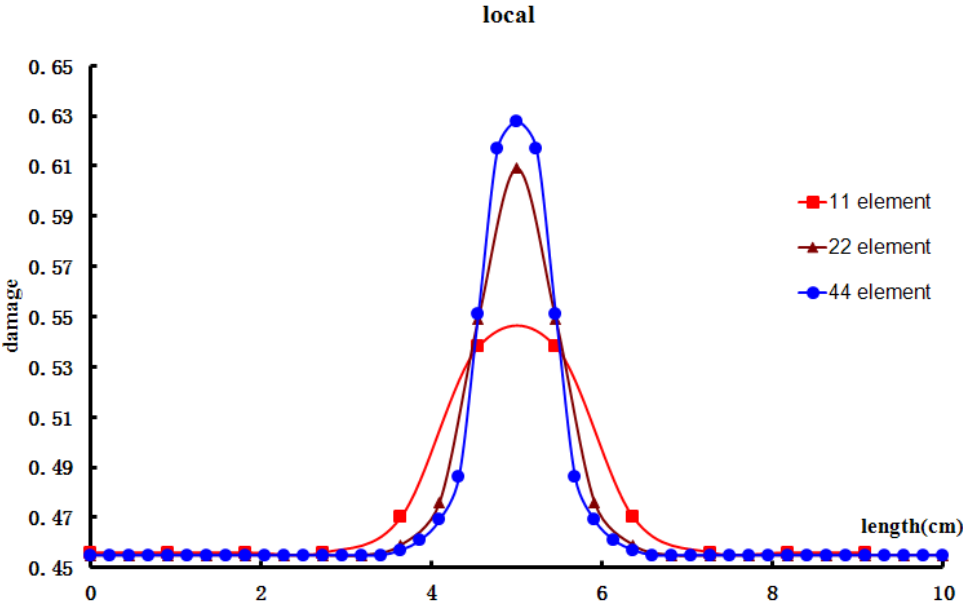


Figure 2.16 Distribution of damage based on length, local model

For reducing the "mesh dependency", various methods have been proposed, the most widely used may be the "non-local" approach. The essential idea of this theory is to

incorporate a so-called "internal length" into the constitutive relation to avoid the "deformation localization". Based on the work of Bazant et al. [61], the proposed model in section 2.2 is modified to avoid the problem of localisation. The non-local driving force \bar{Y}_d is defined to replace the driving force Y_d defined in the section 2.2 ((2.0) and(2.0)):

$$\bar{Y}_d = \frac{\int_{V_r} Y_d dV}{V_r} \quad (2.0)$$

\bar{Y}_d is the average value of Y_d on a representative volume element (RVE) V_r , a weighting function based on the so called "internal length" $w(x, y)$ is introduced for integration on the calculation domain Ω of analyzed structure:

$$\bar{Y}_d = \frac{1}{\Psi} \int_{\Omega} Y_d(x, y) \cdot w(x, y) d\Omega \quad (2.0)$$

where

$$\Psi = \int_{\Omega} w(x, y) d\Omega \quad (2.0)$$

The value of power function $w(x, y)$ depends on its location and the distance r to the aimed integration point. In this work, one Gauss type distribution function is applied, as:

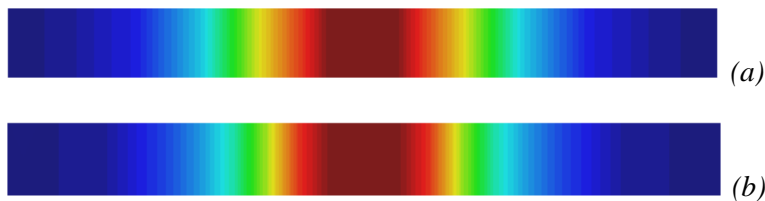
$$w = \frac{1}{(2\pi)^{3/2} l_c^3} \exp\left(-\frac{r^2}{2l_c^2}\right) \quad (2.0)$$

in which l_c is a material characteristic length which determines the extent of interaction zone. The value of l_c depends on characteristic element size, and in 2D problem is proposed to equal to:

$$l_c = \sqrt{A_e} \quad (2.0)$$

in which A_e the average element surface in 2D mesh.

The "non-local" damage model has been used to deal with the same problem proposed at the beginning of this section. In this work, we suppose that the characteristic length is $l_c = 1cm$. The same parameters as listed in Table 2.4 are used. The distributions of damage are given in Figure 2.17 and 2.18. It can be clearly observed that, even with different mesh (different density with 11, 22 and 44 elements), the results are quasi identic. The damage is neither "local" nor mesh dependent. Because the conjugated damage force is the average value on a region with the character length, the maximum damage in the "non-local" model is greatly reduced comparing with that in the "local" model.



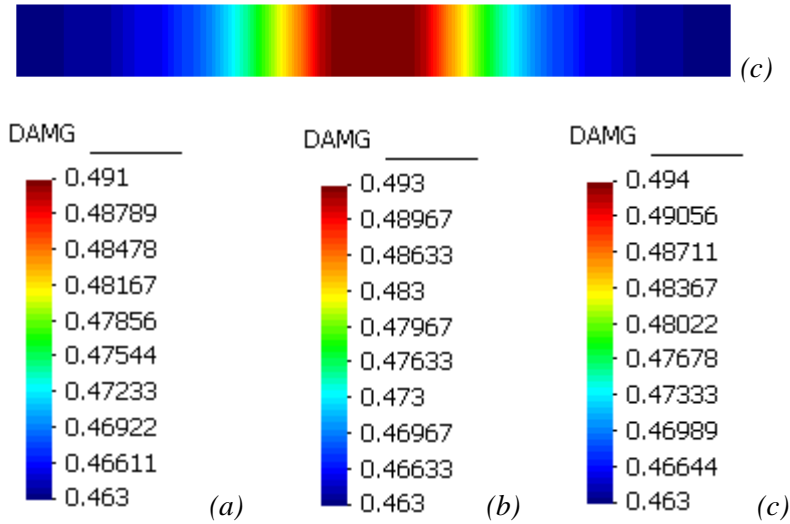


Figure 2.17 Results of the model non-local
(a) 11 elements; (b) 22 elements; (c) 44 elements

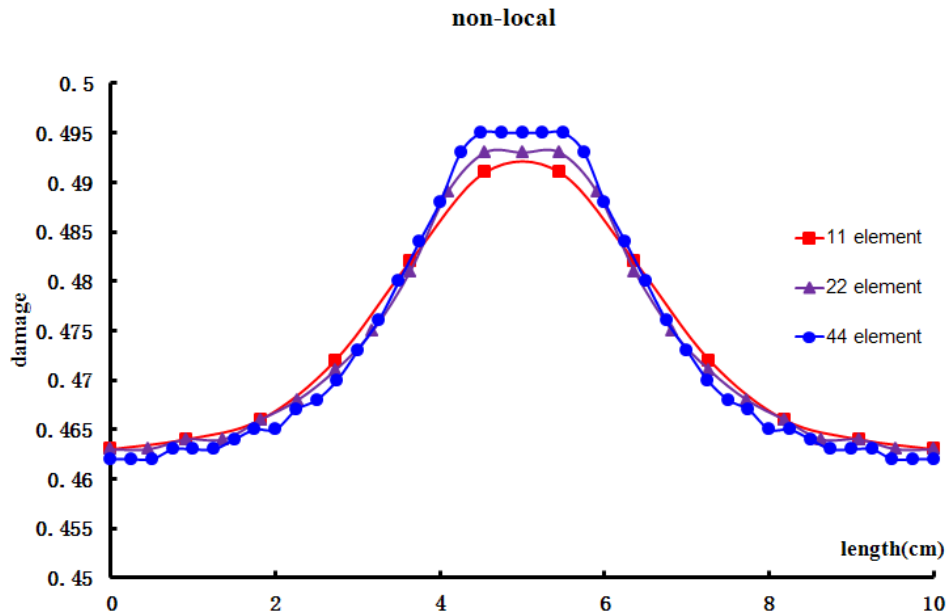


Figure 2.18 Distribution of damage based on length, non-local model

However, in the "non-local" model, the physical meaning of the so called "character length" is a little ambiguity and the determination of its value is sometimes difficult. Generally, the character length l_c defines the zone in which the conjugated damage force will be averaged. For the parametric study of l_c , as shown in Fig. 2.19, with the decline of l_c , the width of localized band will decrease too, while the value of the maximum damage will increase. Another disadvantage of the "non-local" model is that, comparing to the "local" model, the "non-local" model calculation is time consuming, especially for a big structure. That is because, for each integration point, the conjugated damage force should be calculated by using that of its neighbors.

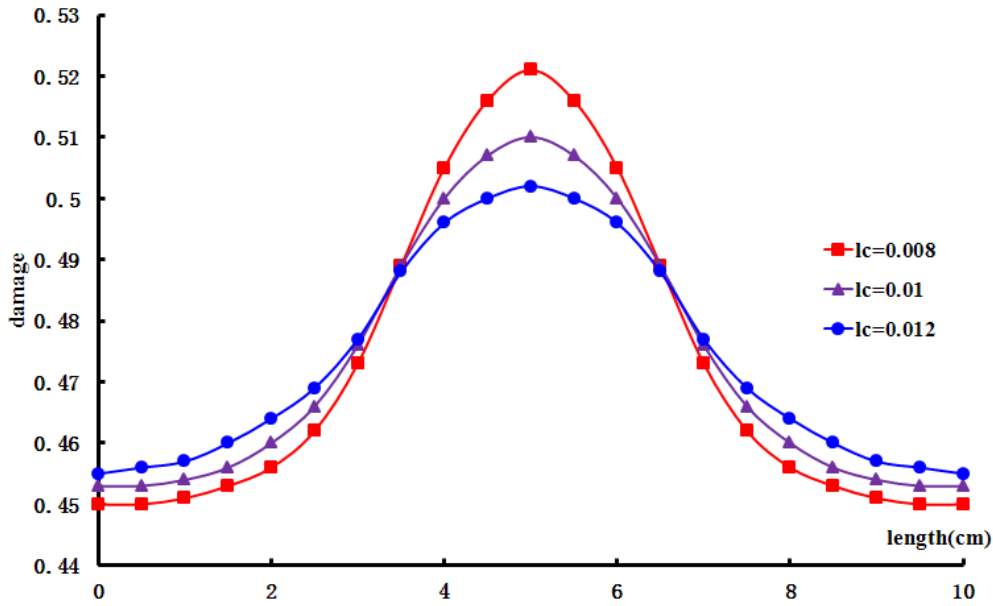


Figure 2.19 Influence of parameter l_c on the damage distribution

Another approach, maybe the ideal approach, is that: when the damage arrive its value corresponding to the peak stress value, instead of the continuous approach, a discontinuous approach would be employed. By means of various discontinuous approach, the extended finite element method (XFEM) has been adopted later in this thesis, which be detailed in Chapter 4.

2.6. Time effects on the damage

The study of the deformation of rocks under creep is useful to better analyze the behaviour of geological structures *e.g.* the landslides and the long-term stability of rock slope, *etc.* in which the rock is subjected to a long-term loading. Experimental observations, such as an increase of dilatancy and hydraulic permeability, a decrease of elastic modulus, and the recording of acoustic emission, attest that microcrack propagation, *i.e.* the damage increase during creep [63]. According to the applied stress level, three damage evaluation models could be identified, which correspond to different creep stages: decreasing damage rate, constant damage rate and increasing damage rate. However, for the jointed rock structure, it is generally controlled by the rock joint which will be detailed in the next chapter. Therefore, only the creep in the first stage will be discussed in this section.

As shown in Fig. 2.20, a typical creep curve of a hard rock under uniaxial compression stress state is considered. We consider two neighbour states of point 1 and 2, with an infinitesimal time increment dt , according to Hook's law and equation(2.0), we can obtained:

$$\dot{\sigma} = \dot{\varepsilon}E + \varepsilon\dot{E} = 0 \quad (2.0)$$

The first term represents the effect of deformation variation and the second represents the effect of material soften. In case of creep state, the imposed stress is kept in constant, the sum of these two terms is zero, so according to the equation above:

$$\frac{\dot{E}}{E} = -\frac{\dot{\varepsilon}}{\varepsilon} \quad (2.0)$$

$$\dot{E} = -\frac{\dot{\varepsilon}}{\varepsilon} E \quad (2.0)$$

After some simple mathematic manipulations, we can easily get the formulation as:

$$E_2 = E_1 + \dot{E} = E_1 \left(1 - \frac{\dot{\varepsilon}}{\varepsilon} \right) \quad (2.0)$$

This formulation can be interpreted in term of damage, as:

$$E = E_0 (1 - \omega) \quad (2.0)$$

The above equation is exactly the same formulation we used for the proposed damage model, *i.e.* equation(2.0). Therefore the material softening in creep phenomenon can be explained and described by damage model. For the damage evolution in the first creep stage, one simple damage model is proposed:

$$\omega_{time} = \beta(1 - \exp(-mt)) \quad (2.0)$$

where β and m are model parameters. β represent the total damage evolution during the first creep stage, while parameter m controls the kinematic of creep damage evolution. t denotes the time. The two parameters can be easily identified from a uniaxial creep test.

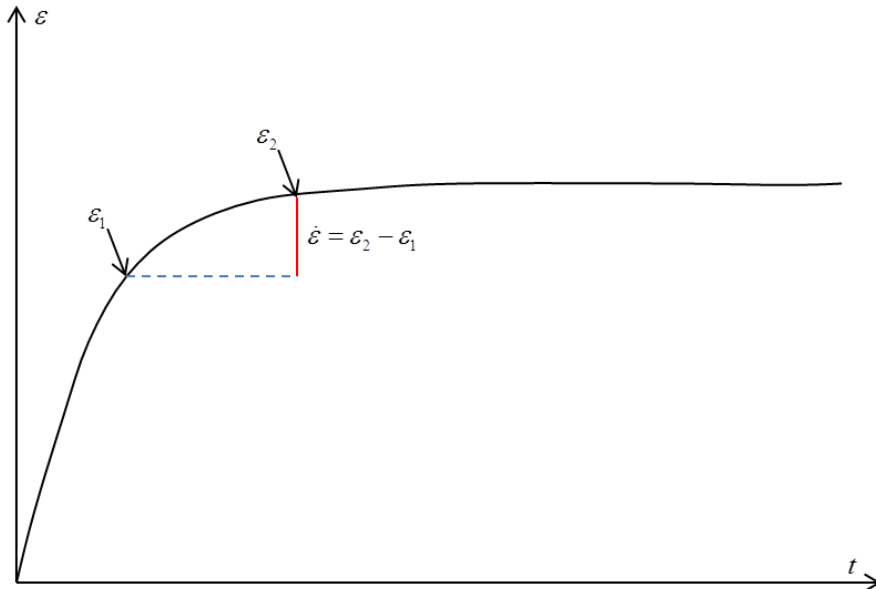


Figure 2.20 A typical creep curve for hard rock in the first creep stage

With the typical parameters for claystone listed in Tab. 2.5, the creep test for a claystone is simulated with the proposed model. The time effect on damage and Young's modulus are

respectively illustrated in Fig. 2.21. With the increase of time, the damage increases exponentially and the Young's modulus decrease in the inverse direction. Based on these parameters, two parametric studies have been conducted respectively for the two parameters, as shown in Fig. 2.22 and Fig. 2.23.

Table 2.5 Model parameter for first creep stage

E (GPa)	ν	m	β
4	0.3	1	0.1

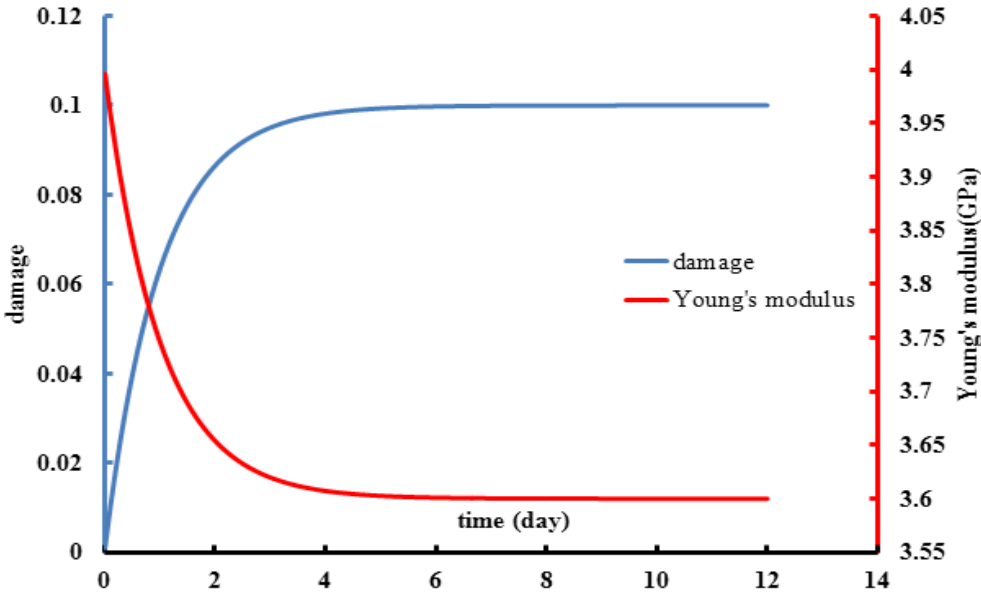


Figure 2.21 Time effect in damage and Young's modulus

Parameter m controls the kinematic of the damage. With a higher m value, the damage increases rapider. As a consequence, as illustrated in Fig. 2.22, the material becomes more “soft”, under the same stress level, the strain increases rapider. However, the final strains are the same, because the parameter β is identic for the three cases. The parameter β represents the total damage variation during the first creep stage. With a bigger β , the final strain will be increased as illustrated in Fig. 2.23.

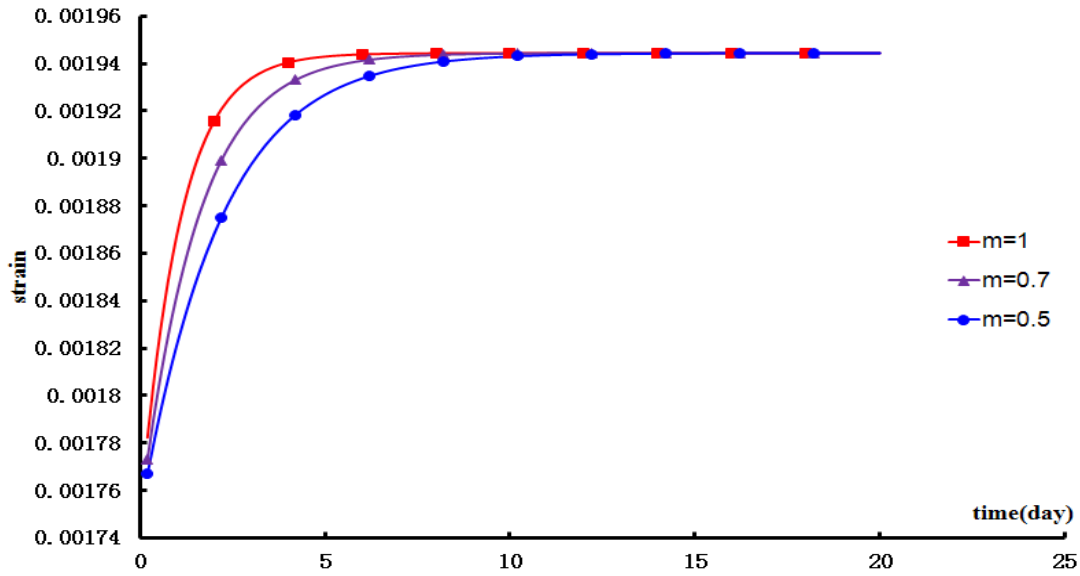


Figure 2.22 Influence of parameter m in creep curves

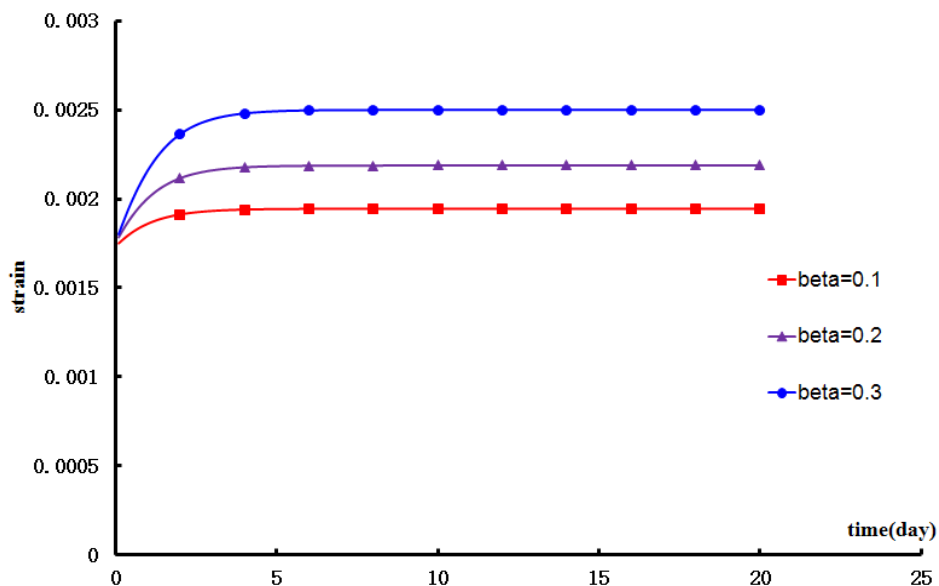


Figure 2.23 Influence of parameter β in creep curves

The creep damage model is then used to simulate the creep tests on a claystone which have been conducted in LML. The model parameters are listed in Table 2.6. The Young's modulus and Poisson's ratio are determined from the triaxial experiments of the same materials, m and β are determined by analyzing the creep experimental curves. The numerical results compared with the experimental data are illustrated in Fig. 2.24. There are good concordance between the numerical results and experimental data for both axial and lateral deformations.

Table 2.6 Model parameters for creep test of a claystone

E (GPa)	ν	m	β
4	0.3	0.8	0.28

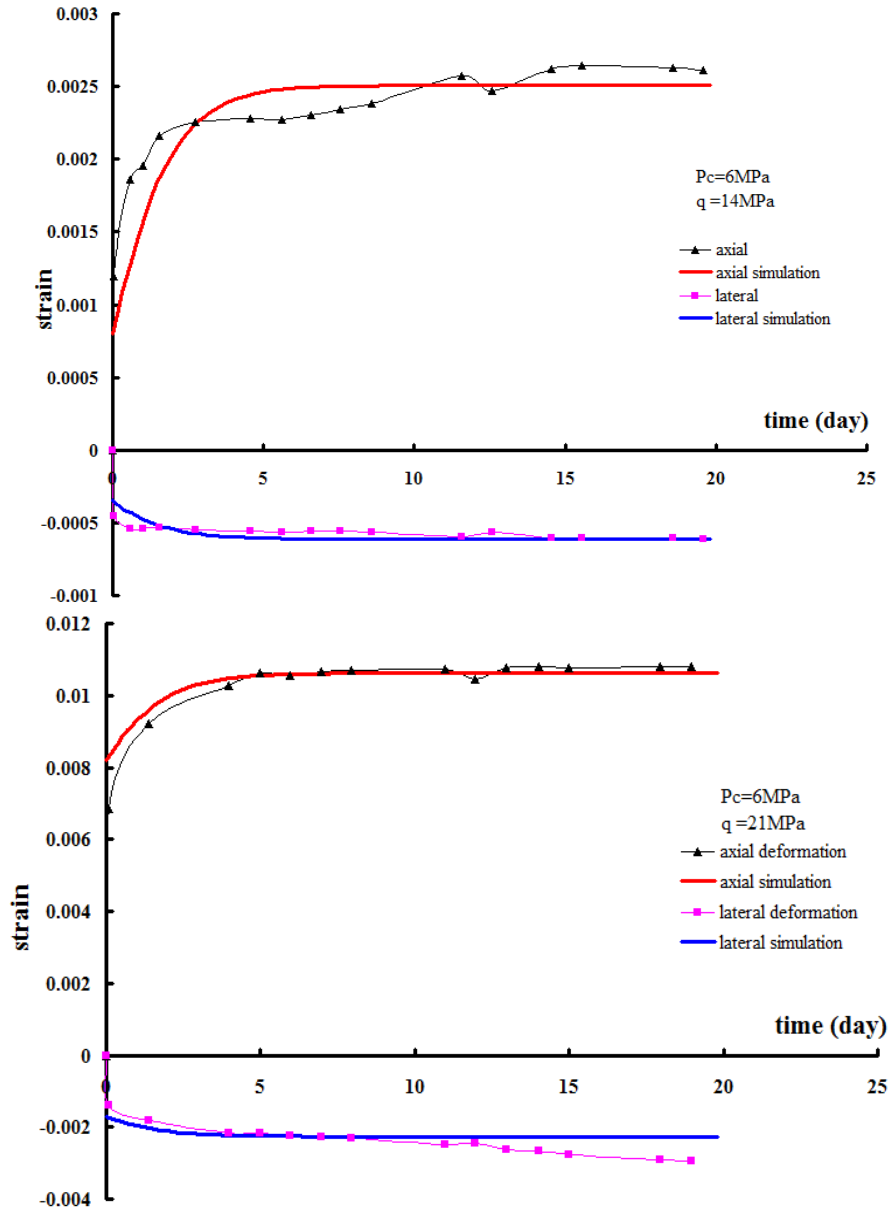


Figure 2.24 Validation with the creep experiments

2.7. Conclusion

In this chapter, an elasto-damage model for hard rock is proposed, this model considers the influence of volumetric deformation, so it has the ability in describing the mechanical response of rock under different confining pressures. A number of simulations of experimental results are performed to validate the prediction ability of this model. Non-local theory is employed in this elasto-damage model to eliminate the influence of element density. And then for analysing the long-term stability of rocks, one time-dependent model is developed, and the simulating results show a good agreement with the creep experimental data.

Chapter 3. Time dependent constitutive model for rock joint

3.1. Introduction

The jointed rocks are frequently analysed in the geo-engineering, such as the rock slope. The term "joint" here represents various discontinuities represented in the rock mass, such as fracture, joints and faults, etc. It is well known that the "joint" dominates the mechanical behaviour of rock mass. In case of the jointed rock slope, the mechanical behaviour of joint controls the stability of the slope.

In the natural conditions, the joints within the rock slopes undergo various coupling actions, which involve the mechanical, hydraulic, chemical and eventually thermal solicitations. Consequently, the mechanical properties of the rock matrix and joints degrade with time. Due to the degradation of the mechanical properties of rock matrix, and more importantly, with the decrease of the resistance of rock joint in the jointed rock slope, the possibility of "lost stability" increase with time. Therefore it is of great interest to evaluate and to predict the long-term stability of jointed rock slopes by taking into account of the mechanical degradation of rock joint.

Many models have been developed to reproduce specific experimental results and then to interpret and predict the mechanical behaviour of jointed rock mass. The difficulty is that, in practice, the loading conditions of joints are more complicated than those exhibited in laboratory shear tests.

Goodman [69] presents an approach for predicting the shear response of a joint under constant normal displacement. This method assumes a series of curves is available for shear tests under constant normal stress. Goodman [69] argues that changing the confinement of the joint to constant normal displacement corresponds to constantly moving from one constant normal stress test to another. Goodman [69] assumes that the instantaneous dilation angle is zero initially and reaches a peak approximately at peak shear stress after which it gradually drops. Saeb and Amadei [70, 71] followed the spirit of the approach used by Goodman [69] and developed a model where the behaviour of the joint is tied explicitly to the combination of shear displacement and confining stress. For example, the presentation of their model starts with model curves of shear stress as a function of shear displacement for different values of confining stress. Key events in the shear tests occur at fixed values of shear displacement. For example, peak shear stress is achieved at a constant value of shear displacement. Among the sample curves that Saeb and Amadei [70] present for their model, all of them commence

dilation immediately with any shear displacement. In one of their examples, dilation ceases at peak stress, while in another example the dilation continues well beyond peak stress.

Plesha [72] introduced a yield surface and plastic potential function to describe the response of the joint. This model was subsequently extended by Nguyen and Selvadurai [73] to account for hydraulic behaviour. Prior to yield, the joint response is elastic. When yielding, the displacement on the joint has an elastic and plastic component. These plastic components of displacement can include dilatant effects. In the model, plastic deformation leads to degradation of the joint asperities and a reduction in friction angle. The theory leads to an elasto-plastic stiffness matrix which contains gradients of the yield function and plastic potential.

Bandis [74] analysed the effect of roughness and alteration on the mechanical fracture under normal stress behaviour. It is showed that it was easier to close a smooth joint than a rough joint. Barton [75] also proposed one model which has been widely used. In these models, the influences of normal stress and the scale effects have been taken into consideration. Another advantage is that the model parameters could be determined easily from the in-situ measurements and laboratory tests. Based on these models, Bart [76] extended these models for considering the effect of the hydro-mechanical behaviour of rock joint.

In this chapter, a constitutive model for rock joint has been presented. Firstly, the instantaneous behaviour has been presented. And then, the time effect, e.g. the long-term behaviour has been integrated in the proposed model via either the degradation of residual friction angle or the roughness of rock joint surface JRC. The proposed model then has been validated by simulating laboratory tests.

3.2. Instantaneous behaviour of rock joint

We consider a segment of rock fracture in its local coordinate system, as shown in Fig. 3.1 and 3.2, the contact surface is idealized as an infinitesimal area of material, thus the general elasto-plastic equations can be used. The normal and shear displacement increments are composed of two parts: an elastic part and a plastic part:

$$du_n = du_n^e + du_n^p; \quad du_t = du_t^e + du_t^p \quad (3.0)$$

where du_n and du_t are respectively the normal and shear displacement increment. The subscript n and t respectively indicates the normal and tangential direction. The superscript e and p respectively indicates the elastic and plastic parts. The plastic displacement corresponds to the permanent sliding and the dilatancy due to the asperities degradation.



Figure 3.1 Crack in macro-scale

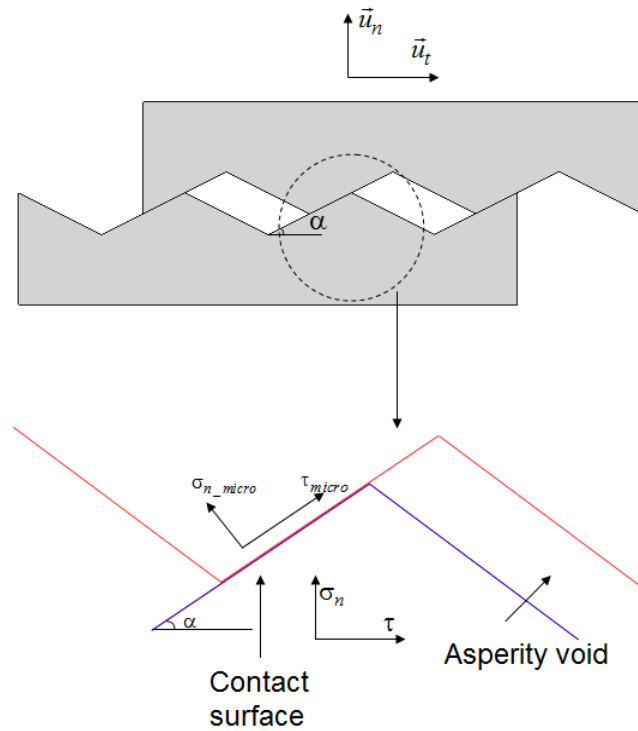


Figure 3.2 Idealized rock joint with regular asperities

The stress variations are related to the elastic displacement increments by simple elastic constitutive law as:

$$\begin{Bmatrix} d\sigma_n \\ d\tau \end{Bmatrix} = \begin{bmatrix} K_{nn} & K_{nt} \\ K_{tn} & K_{tt} \end{bmatrix} \begin{Bmatrix} du_n^e \\ du_t^e \end{Bmatrix} \quad (3.0)$$

where K_{ij} relates the stress increment in i direction ($i = n, t$) and the displacement increment in j direction ($j = n, t$). Generally, these elastic stiffness coefficients K_{ij} are in function of

the normal stress. For simplicity, the two components K_{nt} and K_{mt} are taken as zero. The normal and shear stiffness K_{nn} and K_{tt} will be introduced in the latter parts.

3.2.1. The normal behaviour of rock joint in traction

The stress-strain curve of rock and concrete loaded in uniaxial tension shows an ascending branch, a peak which is called the tensile strength, and a descending branch of softening branch. The post-peak behaviour, where macroscopic fracture appears, can only be measured by using a stiff servo-controlled testing machine. Experimental results shown that beyond the peak, localization of deformations in a small region of the test specimen occurs. The behaviour of geomaterial under tensile loading can be divided into a stress-strain relation for the uncracked part and a stress-crack opening relation for the crack itself.

The elasto-damage model discussed in chapter 2 is implemented in the calculation code for simulating the non-linear mechanical behaviour of rock on a macro level, where the unjointed rock is assumed to be homogeneous. The softening behaviour measured in tension is then considered to be a material property. This behaviour has to be derived from a stable displacement controlled uniaxial tensile test. The parameters that defined the first part of the measured response are the initial Young's modulus and the Poisson's ratio, and the parameter controlling the damage kinematic and the damage threshold. For the second part of the response, the softening curve, *i.e.* the mechanical behaviour of the joint in traction, should be introduced. Based on the experimental measurements, an empirical formulation has been given as (similar to that of [77]):

$$\sigma = f_t \left[\exp\left(-c_1 \frac{[u_n]}{[u_n]_m}\right) - \frac{[u_n]}{[u_n]_m} \exp(-c_1) \right] \quad (3.0)$$

where f_t is the tensile strength of the material, $[u_n]_m$ is the maximum crack opening when no stress is transferred any more, and c_1 is an empirical constant, which controls the shape of stress-crack opening curve. From the post-peak diagram, as shown in Fig 3.3, the fracture energy G_f can be determined. G_f represents the area under the curve, the various parameters are assumed to be material properties, and can be identified directly from the uniaxial tensile test. In this model, one damage threshold ω_0 could be defined to determine the start point of the crack opening.

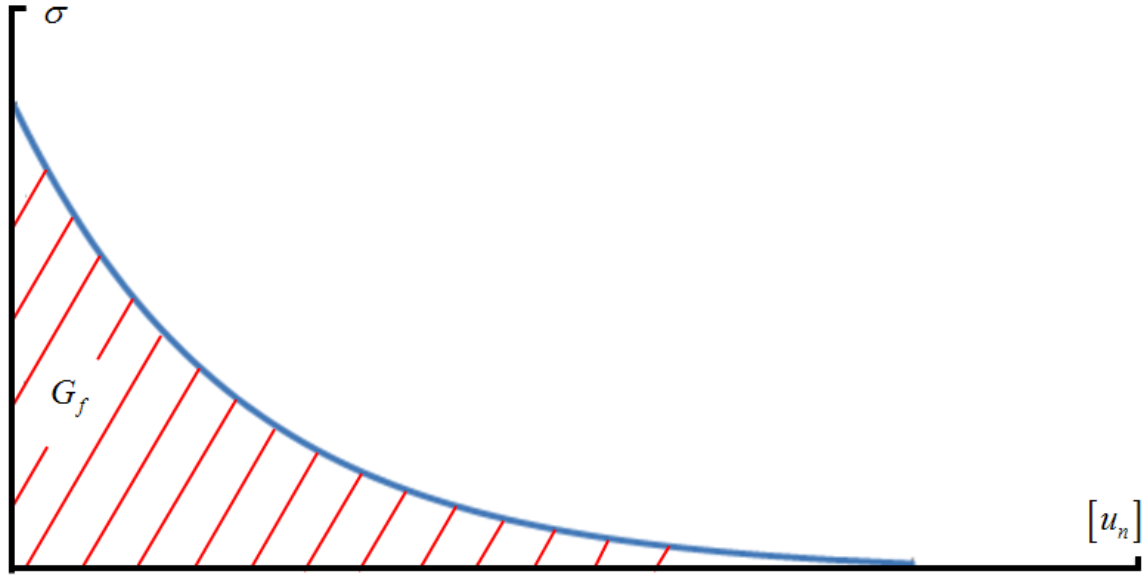


Figure 3.3 Fracture energy of in traction

3.2.2. The normal behaviour of rock joint in compression

A hyperbolic relation fitting the fracture closure-normal stress behaviour, similar to that of Bandis [74], is given as:

$$\sigma_n = \frac{K_n^0 [u_n]}{1 - [u_n]/[u_n]_m} \quad (3.0)$$

where K_n^0 is an empirical parameter representing the initial normal stiffness in compression, $[u_n]_m$ is the maximum possible fracture closure. According to equation(3.0), the fracture closure $[u_n]$ can be given in function of normal stress σ_n as:

$$[u_n] = \frac{K_n^0 [u_n]_m}{K_n^0 [u_n]_m + \sigma_n} \quad (3.0)$$

Derived from equation(3.0) , the normal stiffness K_n of the fracture can be written as:

$$K_n = \frac{d\sigma_n}{d[u_n]} = \frac{K_n^0}{(1 - [u_n]/[u_n]_m)^2} \quad (3.0)$$

Based on the experimental data, it is well known that the relationship between the variation of the fracture aperture and the normal stress is high nonlinear and the relation is always in the incremental form, as:

$$d\sigma_n = K_n([u_n])d[u_n] \quad (3.0)$$

$d\sigma_n$ is the increment of the normal stress, K_n is the tangent normal modulus (expressed in MPa) and $d[u_n]$ is the increment of the fracture aperture.

The most widely adopted model for a nonlinear behaviour of fracture under normal stress is the hyperbolic function for normal closure of fracture with consideration of normal stress

[78]. The fracture closure $[u_n]$ is related to the normal stress σ_n through an empirical hyperbolic formation, as given:

$$\sigma_n = \sigma_{n0} \left[1 + \left(\frac{[u_n]}{[u_n]_m - [u_n]} \right)^D \right] \text{ for } \sigma_n \geq \sigma_{n0} \quad (3.0)$$

σ_{n0} is the initial normal stress or the so-called low seating normal stress, D is a dimensionless empirical exponent, approached asymptotically as the normal stress increases.

In(3.0), two model parameters: the initial normal stiffness K_n^0 and the maximum possible fracture closure $[u_n]_m$ have to be established. In the framework of XFEM, for the reason of simplification, it can be assumed that the maximum possible fracture closure $[u_n]_m$ equals to the initial fracture aperture. However, some experimental investigations show that there is always a residual flow even at high normal stress. Therefore, the maximum possible fracture closure is less than initial aperture. For taking the residual flow into account, we assume that the maximum possible fracture closure $[u_n]_m$ is equal to 90% of the initial crack aperture.

Some experimental results[74] are employed for validate this compressive model. According to the tests in laboratory, the parameters of the fracture are established directly:

Table 3.1 Crack parameters for joint compressive simulations

Materials	$K_n^0 (MPa / \mu m)$	$[u_n]_m (\mu m)$
Marble of St Pons	0.0161	-123
Granite of Tennesles	0.0157	-103
Schist of Tr é daz é	0.1205	-65

From the simulation results shown as belows (Fig. 3.4-3.6), it can be seen that the model can reflect exactly the relationship $[u_n] \sim stress$.

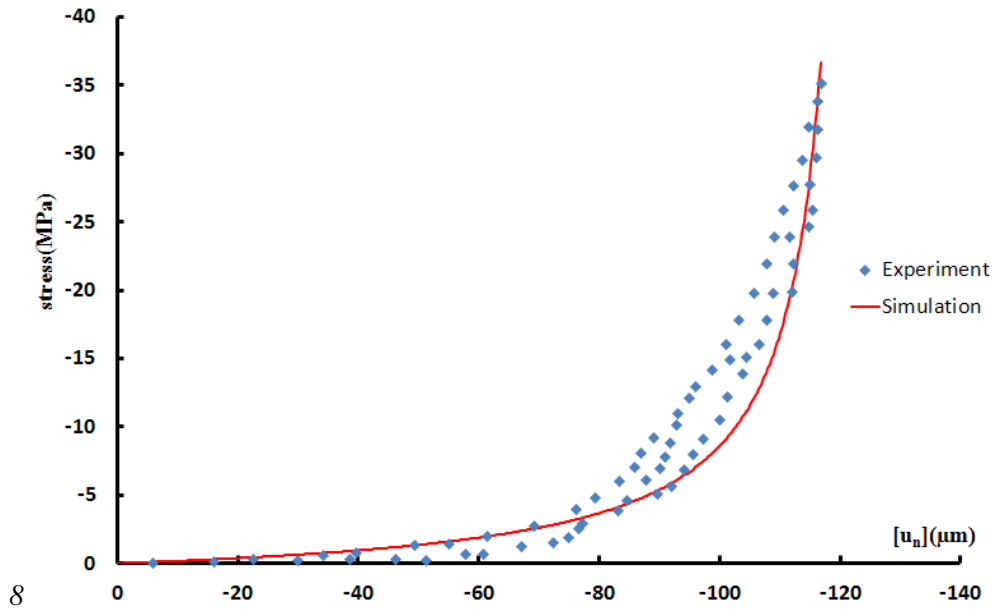


Figure 3.4 Simulation of Marble of St Pons

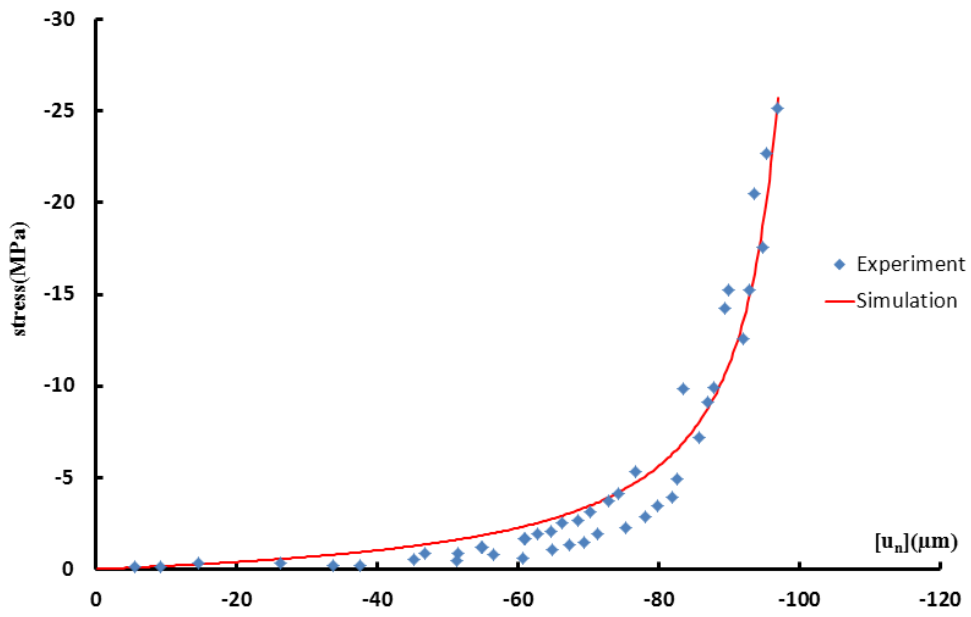


Figure 3.5 Simulation of Granite of Tennessees

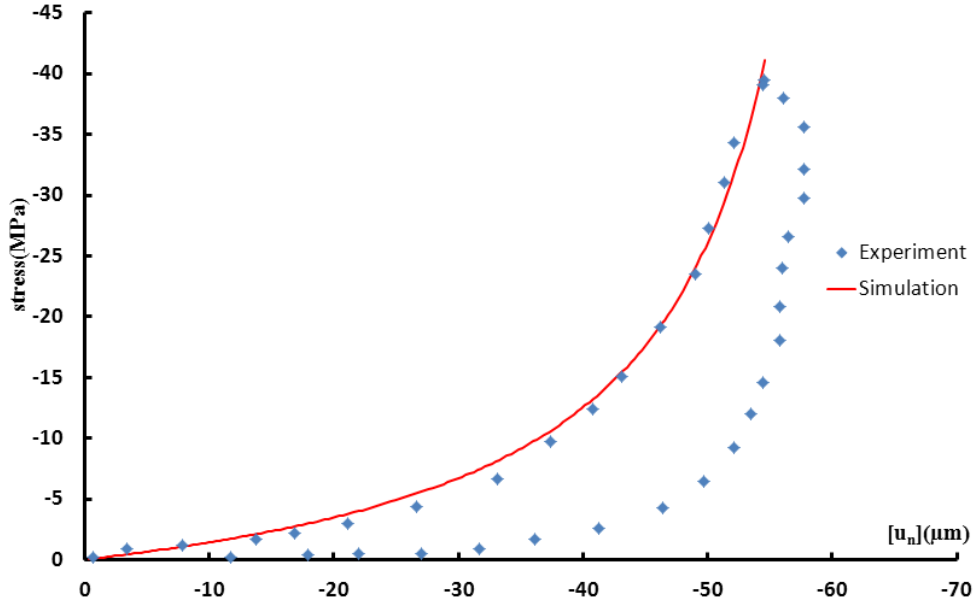


Figure 3.6 Simulation of Schist of Tr ěaz ě

3.2.3. The tangent behaviour of rock joint in shear

The plastic shear displacement or the permanent sliding between the two surfaces of rock joint, accompanying with the degradation of asperities, are given by the following plastic flow:

$$\begin{aligned} du_i^p &= 0 && \text{if } F(\sigma_n, \tau, H) < 0 \text{ or } \dot{F} < 0 \\ du_i^p &= \lambda \frac{\partial G}{\partial \tau} && \text{if } F(\sigma_n, \tau, H) = 0 \text{ and } \dot{F} = 0 \end{aligned} \quad (3.0)$$

where F is the loading surface and G is the plastic potential. λ is the plastic multiplier and H is the hardening function. Both the loading surface and the plastic potential are given in latter part.

The simplest interface, from the viewpoint of the microstructure, is the complete smooth surfaces. Assuming that the criterion of Coulomb is valid for this simplest surface, the loading surface is given by:

$$F = |\tau| + \tan(\Phi_r) \sigma_n \quad (3.0)$$

where τ and σ_n are respectively the shear stress and the normal compressive stress on the surface, while Φ_r is the residual friction angle.

The plastic potential is then given by Michalowski and Mroz [79]:

$$G = |\tau| \quad (3.0)$$

However, it is evident that this assumption is not valid for rough surfaces fractures. As indicated by Bandis [80], the roughness, different sizes of asperities, has an important effects on the mechanical behaviour of rock joint. So the effects of roughness, *i.e.* the “microstructure”, should be taken into account in the numerical model of the rock joint. Plesha [72] idealized the asperities into two simple models: the saw tooth model and the

sinusoidal model. The model employed in this work is based on the saw tooth model, as shown in Fig. 3.2, where the angle α represents the roughness of the rock joint surface. The normal stress σ_{n_micro} and shear stress τ_{micro} on the asperities surface, which have been taken into consideration in the scale of asperities, have been regarded as microscopic variables. Contrary, the normal stress σ_n and shear stress τ on the rock joint surface have been considered as macroscopic variables. As illustrated in Fig. 3.2, the stress in microscopic scale can be determined from that of macroscopic scale as:

$$\sigma_{n_micro} = \sigma_n \cos \alpha - \tau \sin \alpha \quad (3.0)$$

$$\tau_{micro} = \sigma_n \sin \alpha + \tau \cos \alpha \quad (3.0)$$

Assuming that the asperity surface is completely smooth with a friction angle as ϕ , and the Coulomb model is valid on this type surface. By taking equation (3.0) and (3.0) into equation (3.0), we have the loading surface of the “rough” rock joint (the roughness is represented by a series of saw tooth with angle α as:

$$F = |\sigma_n \sin \alpha + \tau \cos \alpha| + \tan(\Phi_r)(\sigma_n \cos \alpha - \tau \sin \alpha) \quad (3.0)$$

By taking the equation (3.0) into equation(3.0), we get the plastic potential as:

$$G = |\sigma_n \sin \alpha + \tau \cos \alpha| \quad (3.0)$$

During shearing processes, under high normal stress, the asperity degraded, and as a consequence, the roughness of the rock joint decreases. In fact, the shearing load could translate the roughness surface to a smooth one. That means the angle α is not a constant during shearing, it decreases with the increase of plastic work. The definition of the angle α during shearing is then based on the description of the phenomenon of asperity degradation. Plesha [72] provides a simple expression of this angle as:

$$\alpha = \alpha_0 \exp(-cW^p) \quad (3.0)$$

where α_0 is the initial angle of the asperities, while W^p represent the plastic work, as defined as:

$$W^p = \int_0^{u_t^p} \tau du_t^p \quad (3.0)$$

where du_t^p is the plastic shear displacement.

and c is the constant expressing the effect of the degradation of asperity, according to Benjelloun and Nguyen [73, 81], it can be calculated as:

$$c = a \left(\frac{|\sigma_n|}{P_{atm}} \right)^b \quad \text{and } a>0, b<0 \quad (3.0)$$

The asperities of a real rock joint are not a series of triangle we can measure directly the incline angle α . In fact, the asperities are so complicated that it is difficult to measure and identify. Generally, it is represented by JRC , joint roughness coefficient. Based upon

experiments, Barton [75] determined the following relationship between α_0 , normal stress σ_n , joint compressive strength JCS and joint roughness coefficient JRC as:

$$\alpha_0 = JRC \cdot \text{Log} \left(\frac{JCS}{|\sigma_n|} \right) \quad (3.0)$$

where JCS is the joint compressive strength, it can be obtained either indirectly from representative rock material or directly from the joint surfaces themselves by means of simple test. JRC is the joint roughness coefficient which varies from 20 to 0 (Fig. 3.7) representing from the roughest to smoothest surfaces. JRC can be either an approximate value can be predicted by matching surface profiles from the joints of interest with typical profiles proposed by Barton and Choubey [82]:

$$JRC = \frac{\alpha - \Phi_r}{\log(JCS / \sigma_{n0})} \quad (3.0)$$

σ_{n0} is the effective stress value when the slide happens, Φ_r is the residual friction angle.

JRC can also be back-calculated from the experiment results [75]:

$$JRC = JRC_0 \left(\frac{L_n}{L_0} \right)^{-0.02JRC_0} \quad (3.0)$$

$$JCS = JCS_0 \left(\frac{L_n}{L_0} \right)^{-0.03JRC_0} \quad (3.0)$$

Finally, just as that of Barton's model [75], the following expression is used to define the shear stiffness K_{tt} :

$$K_{tt} = \frac{|\tau_{pic}|}{u_t^{pic}} = \frac{\left| \sigma_n \tan \left(JRC \log \left(\frac{JCS}{|\sigma_n|} \right) + \Phi_r \right) \right|}{u_t^{pic}} \quad (3.1)$$

where u_t^{pic} is the shear displacement corresponding to the peak shear stress, and it is defined by Barton and Bandis [75] as:

$$u_t^{pic} = \frac{L}{500} \left(\frac{JRC}{L} \right)^{0.33} \quad (3.2)$$

where L is the initial length of the fracture. We can find that when the shear displacement equal or less than u_t^{pic} , the shear stress is always lower than the peak value τ_{pic} ; the stress state is always inside the loading surface and it is in the elastic state. Thus, a standard shear displacement - shear stress curve given by the proposed model will be divided into two phases: a linear phase until the peak shear strength τ_{pic} and a phase softening.

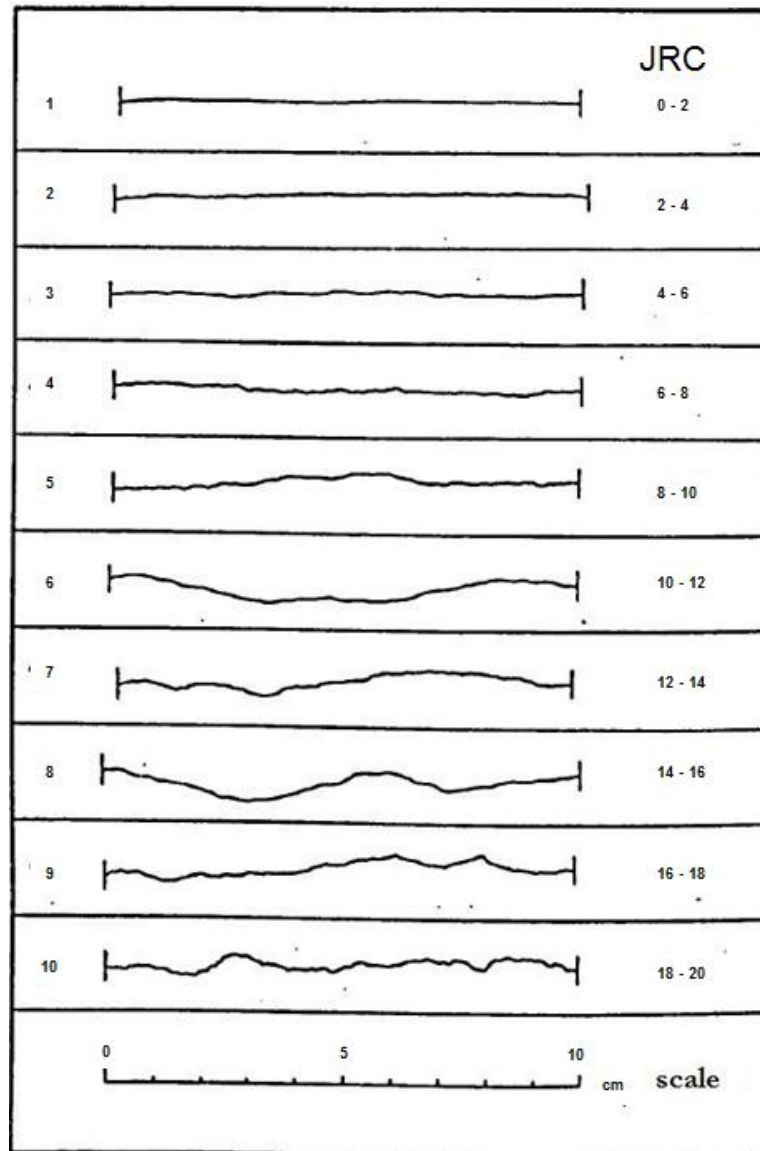


Figure 3.7 Typical roughness profiles for JRC range (Bandis) [80]

This model is appropriate to describe the mechanical response of rock joints. Firstly, because of the simplicity of this mathematical formulation, it is easy to be implemented in a calculation code. Secondly, it is based on physical considerations: the loading surface and plastic potential are defined from the microstructure of rock joint. By relating the average asperities angle α_0 to the joint roughness coefficient JRC , the proposed model initially for idealized rock joint with a series saw-tooth is valid for all types of joints with different microstructure of the interface.

3.3. Numerical simulation of laboratory tests

3.3.1. Identification of model parameters

A number of parameters are introduced when employing this joint shear model, so sensitive analyses are necessarily needed to investigate the effect of these parameters. 7 parameters mentioned before are involved respectively:

- 1) JRC_0 , initial joint roughness coefficient;
- 2) JCS_0 , initial joint compressive strength;
- 3) Φ_r , residual friction angle;
- 4) L_n , initial length of the fracture;
- 5) L_0 , initial length of the fracture determined in laboratory;
- 6) a and b , parameters in determination of α .

JRC_0 , JCS_0 , Φ_r , L_n and L_0 can be determined in laboratory tests, variables a and b should be adjusted in simulations.

One simple numerical model is built to perform these sensitive analyses:

The Young's modulus of matrix is set to be extremely big to make the deformations concentrate in joint, the original crack parameters employed are as below (Tab 3.2):

Table 3.2 Basic parameters for the sensitive analyses

JRC_0	JCS_0 (MPa)	Φ_r (°)	L_n (m)	L_0 (m)	a (m/MN)	b
10.6	2	32	0.09	0.09	1000	0

The results of the sensitive analyses (Fig. 3.9-3.15):

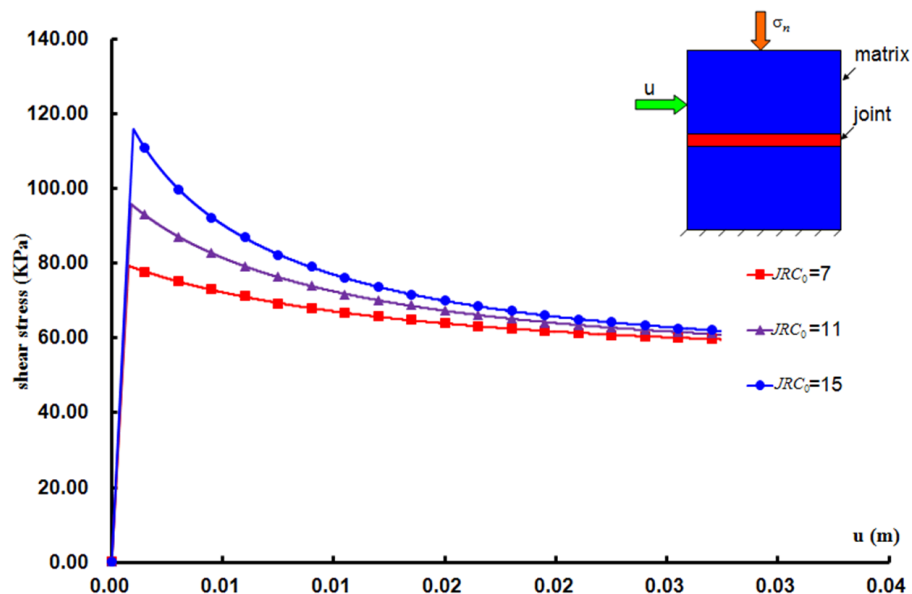


Figure 3.8 Sensitive analysis of JRC_0

As shown in Fig. 3.7, the bigger value of JRC_0 represents the higher joint roughness, the same shear displacement corresponds the higher shear stress (Fig. 3.8).

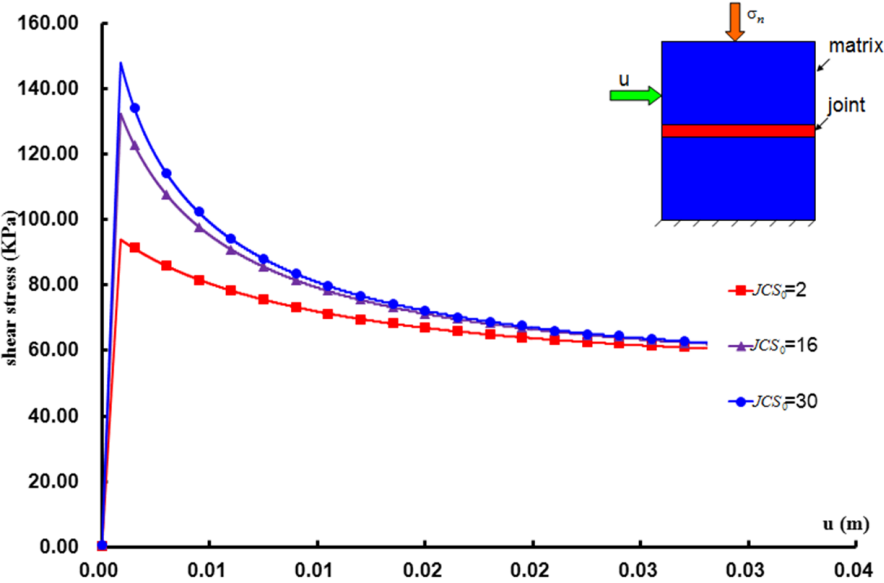


Figure 3.9 Sensitive analysis of JCS_0

Different initial joint compressive strength JCS_0 would cause the variation of joint friction coefficients, and then influence the stress level (Fig. 3.9).

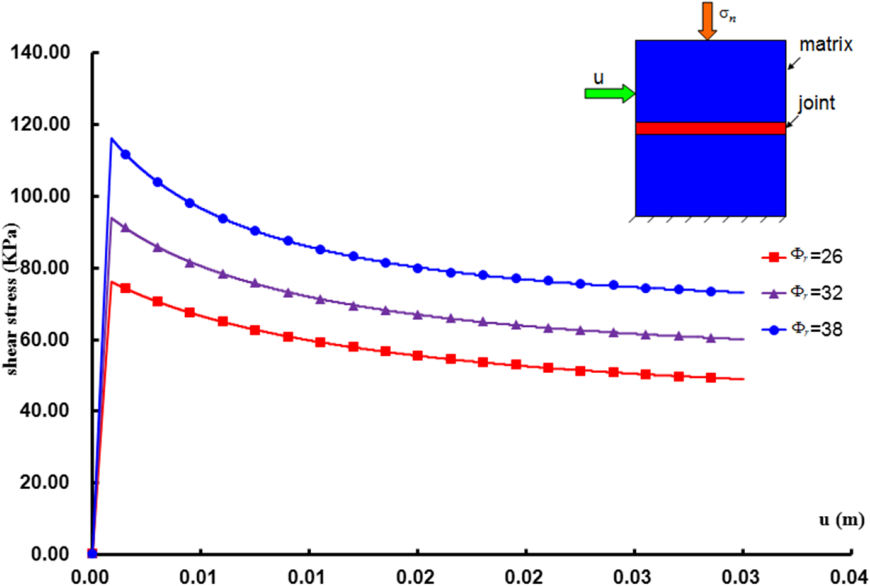


Figure 3.10 Sensitive analysis of Φ_r

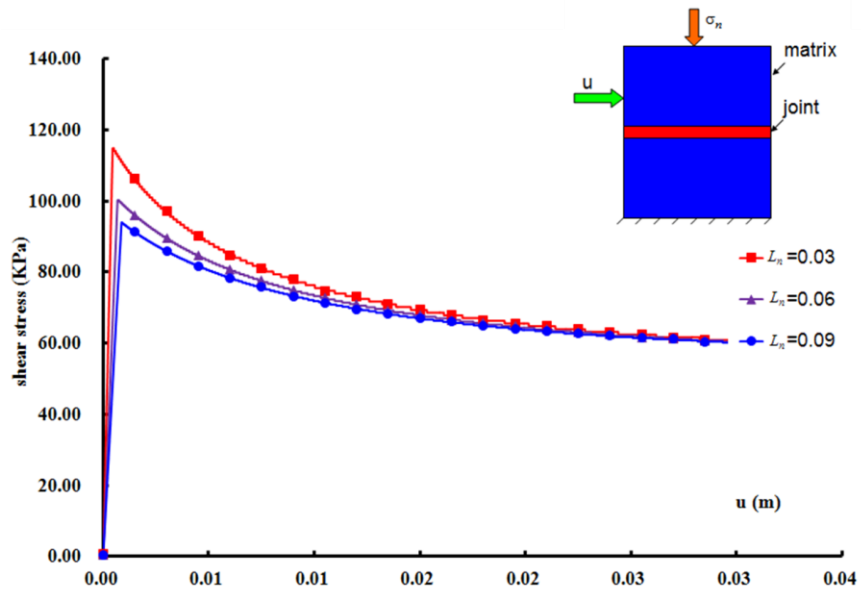


Figure 3.11 Sensitive analysis of L_n

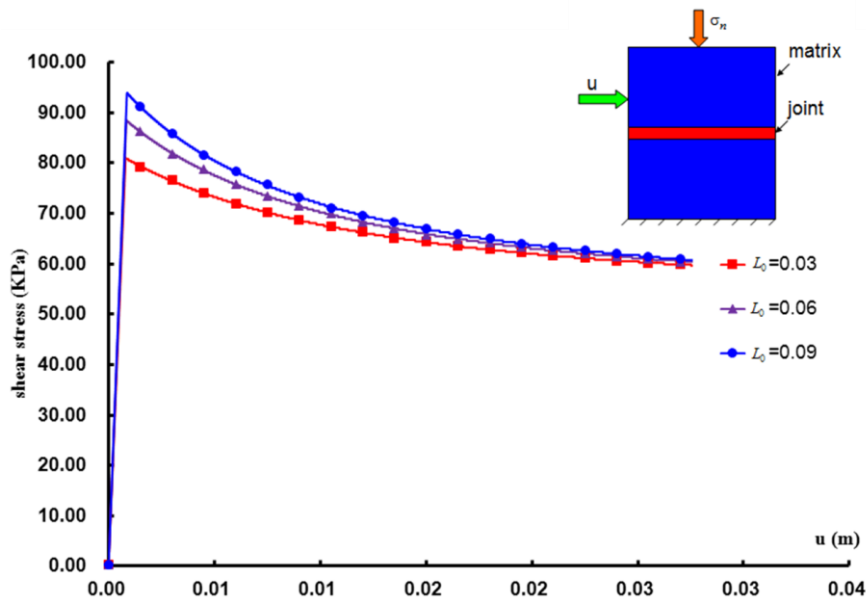


Figure 3.12 Sensitive analysis of L_0

As in (3.0) and (3.0), the initial crack length L_n and L_0 work as a ratio $\frac{L_n}{L_0}$, the value of JRC_0 and JCS_0 decrease with the augment of this ratio value, and then decrease the peak value of the curves (Fig. 3.11 and Fig. 3.12).

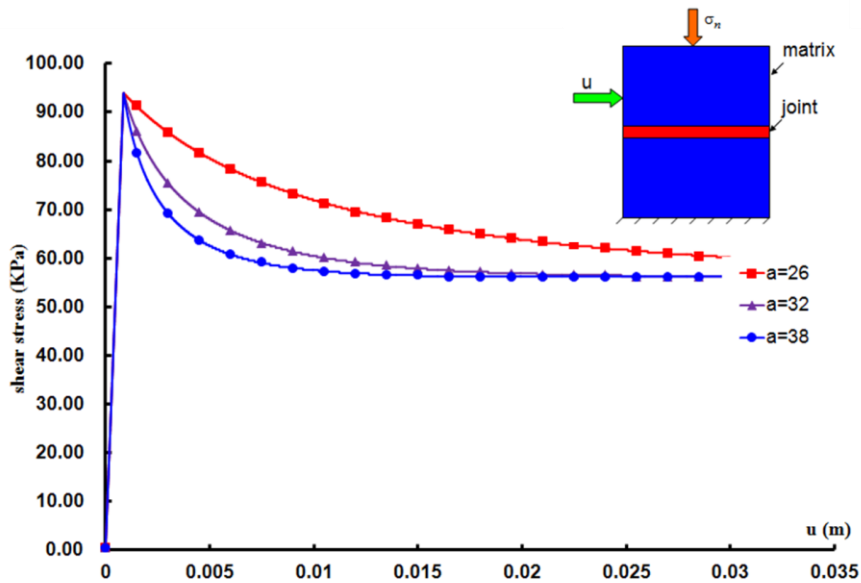


Figure 3.13 Sensitive analysis of a

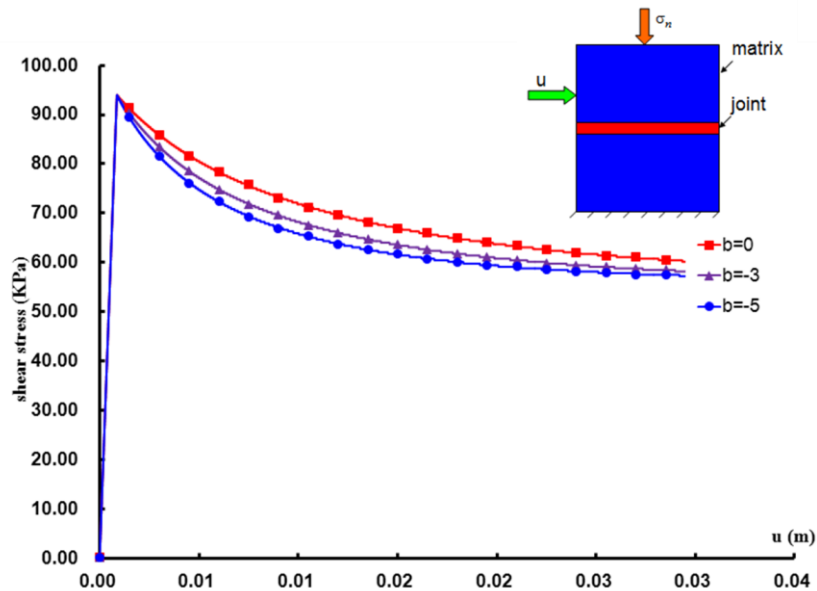


Figure 3.14 Sensitive analysis of b

The coefficients a and b affect the angle of the asperities α , ((3.0) and(3.0)), and then cause the variation of the displacement-stress curves (Fig. 3.13 and Fig. 3.14).

3.3.2. Numerical simulation of laboratory tests

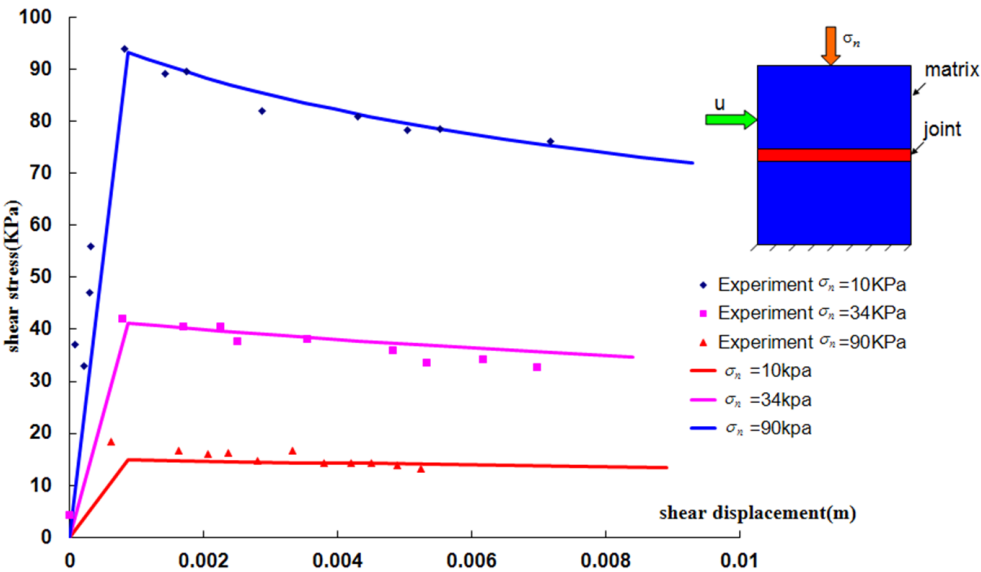
In the base of these sensitive analyses, simulations of the experimental results are performed to verify the numerical model we employed. The same numerical mesh model of previous section is used.

According to the experiments, the curves shear stress- shear displacement under different normal stress and different L_0 are quoted for the calibrations (Tab. 3.3): (a) results of

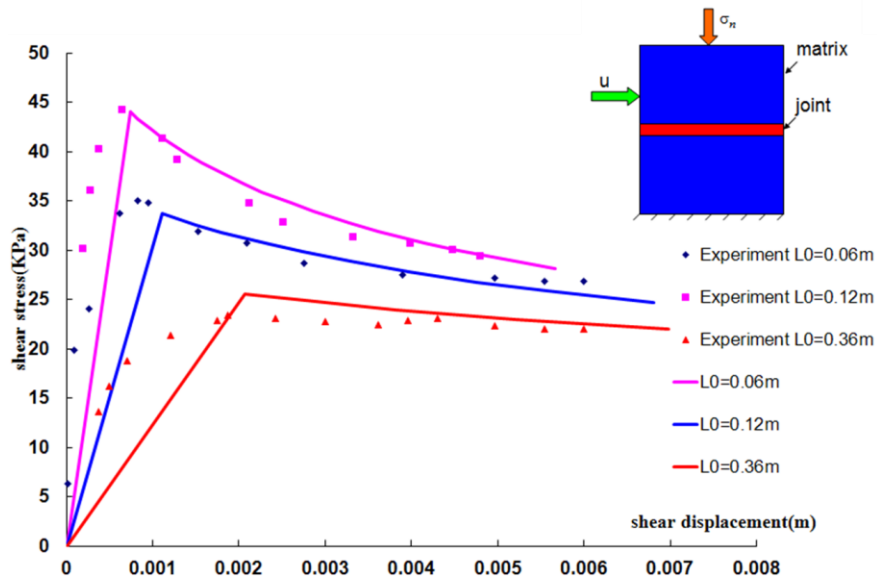
experiments Bandis [83], these experiments analysed the influence of different normal stresses; (b) results of experiments Bandis [80], it shown the different results under divers initial crack length L_0 ; (c) results of experiments Skinas [84]. These experiments analysed the influence of different normal stresses in a higher scale than (a).

Table 3.3 Crack parameters for joint shear simulations

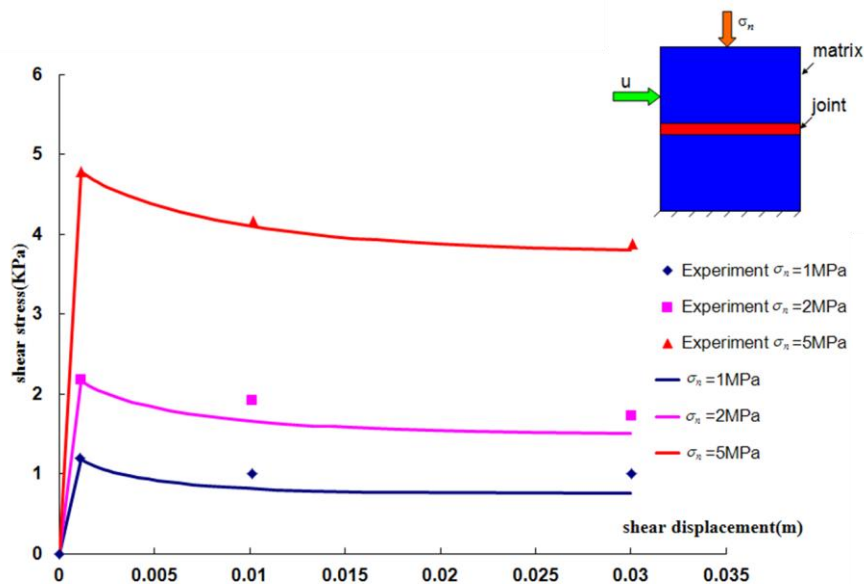
N °of experiments	Author	Main parameters of fracture	remarks	Model parameters a and b
1	Bandis (1981)	$JRC_0 = 10.6$ $JCS_0 = 2MPa$ $L_0 = L_n = 0.09m$ $\Phi_r = 32^\circ$	3 normal stresses are tested : $\sigma_n = -90kPa,$ $-34kPa, -10kPa$	$a = 1000m / MN$ $b = 0$
2	Bandis (1980)	$JRC_0 = 15$ $JCS_0 = 2MPa$ $L_0 = L_n = 0.09m$ $\Phi_r = 32^\circ$	The normal stress: $\sigma_n = -25kPa$ 3 lengths are tested: $L_0 = 0.06m,$ $0.12m, 0.36m$	$a = 3000m / MN$ $b = 0$
3	Skinas (1990)	$JRC_0 = 9$ $JCS_0 = 28MPa$ $L_0 = L_n = 0.15m$ $\Phi_r = 37^\circ$	3 normal stresses are tested : $\sigma_n = -1MPa,$ $-2MPa, -5MPa$	$a = 2891m / MN$ $b = -1.22$



(a) Test of Bandis (1981)



(b) Test of Bandis (1980)



(c) Test of Skinas (1990)

Figure 3.15 Results of simulations for joint

A short summary can be made for these parameters (Fig. 3.8-3.14) and simulations (Fig. 3.15). The parameters JRC_0 , JCS_0 , L_n and L_0 control the values of JRC and JCS , which are the variables in calculating the shear stiffness of rock joint K_n , and then influence the mechanical responses of joints. Therefore, as can be observed in sensitive analyses, it can be concluded that with the increase of parameters JRC_0 , JCS_0 , the shear modulus grows and results the augment of shear stress peak value, the increase of initial crack length L_n and that laboratorial value L_0 will cause the decrease of material shear modulus. Parameters a and b only influence the variable α , so they don't affect the peak value of the curves but the only

the decrease velocity of the curves. From the results (Fig. 3.15), it can be seen that the numerical results agree well with the experimental ones.

3.4. Time effect in crack

Based on the experimental and in-situ observation, both the friction angle and the morphology of rock joint surface evaluated with time (generally decrease with the increase of time), resulting from the weathering, the freeze-thaw cycle and the interaction water-rock, etc.

3.4.1. Time effect of friction angle Φ_r

Gutierrez et al. [85] conducted an experimental study on the effects of fluid content on the mechanical behaviour of natural fractures in chalk. It is found that the weakening in shear strength of rock joint is attributed partly to the reduction of the basic friction angle, and this reduction was verified in a series of tilt tests to measure the frictional resistance between smooth edges of core samples of chalk. The reduction of the basic friction angle implies that the interaction of chalk with water is governed not only by capillary forces, as postulated in several previous studies, but also by chemical and/or physic-chemical effects. Woo et al. [86] conducted a series of experiments to investigate the influence of weathering on shear strength of joints in a porphyritic granite rock mass. It is found that the residual friction angle depends mainly on the weathering state of the joint surface. However, there is no enough experimental data to observe exactly the degradation of the friction angle. We suppose an exponential function to describe the friction angle degradation as:

$$\Phi_r = \Phi_{r\infty} + (\Phi_{r0} - \Phi_{r\infty})Exp(-At) \quad (3.2)$$

where Φ_{r0} represent the initial friction angle of fresh rock joint surface, while $\Phi_{r\infty}$ represent the residual friction angle of weathered rock joint surface. t is time and parameter A controls the kinetic of the friction angle degradation. The friction angle degradation process has been illustrated in Fig. 3.16.

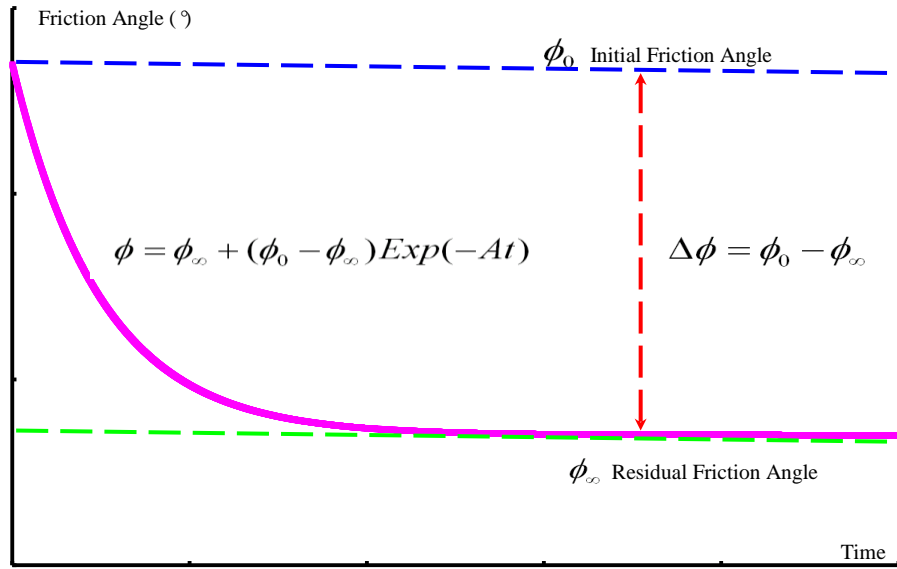


Figure 3.16 Illustration of the friction angle degradation in function of time

To clarify the influence of this time effect, some sensitive analyses are performed. The initial residual friction angle is given as 37° , and the final residual friction angle is given as 17° , and the time considered is supposed as 10 years. Four different velocities represented by parameter A are given, as illustrated in Fig. 3.17. When parameter A equal to 0, that means no degradation for the residual friction angle, while for A equal to 1, it means a total degradation, after 10 years, the residual friction angle attends the final value, *i.e.* 17° . With these four different degradation velocities, the shear displacement-shear stress relations are given in Fig. 3.18.

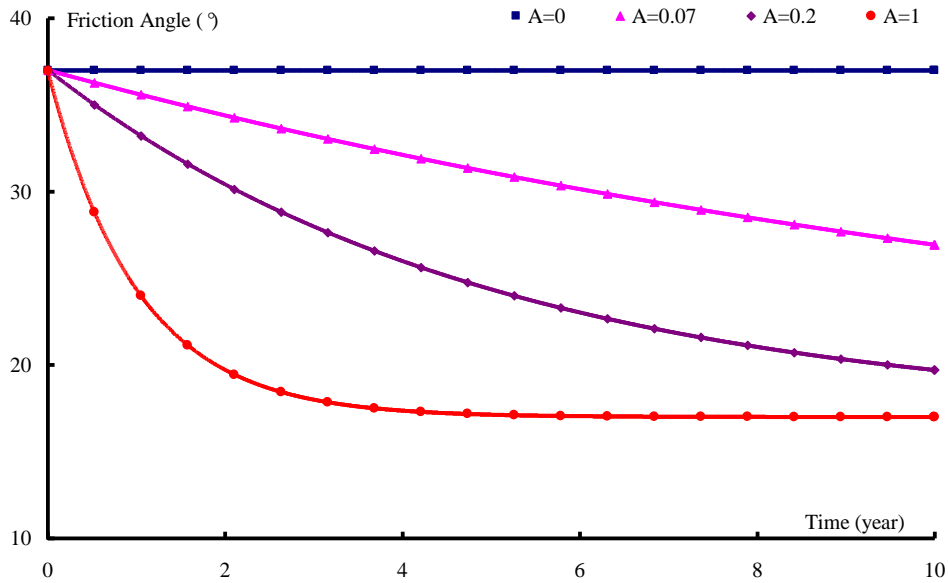


Figure 3.17 The degradation of residual friction angle in function of time with different velocities

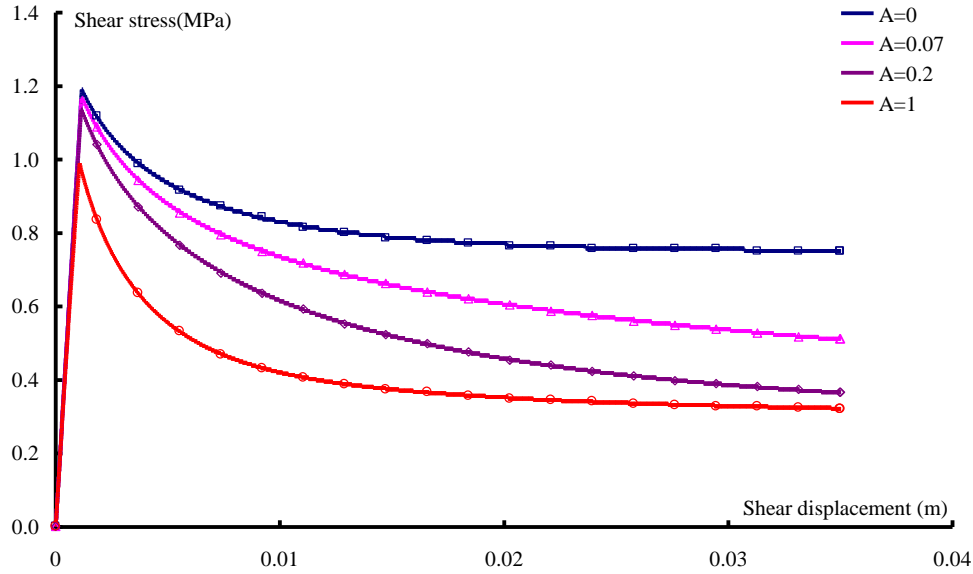


Figure 3.18 Influence of the degradation of the residual friction angle on the mechanical behaviour of rock joint under constant normal stress

3.4.2. Time effect of joint roughness coefficient JRC

The asperities of the rock joint surface degraded under the weathering effect, the joint surface has the tendency to be smoother with time passage. As consequence, the joint roughness coefficient JRC decreases. Similar to that of residual friction angle, we propose the following formulation to describe the morphology degradation of the rock joint as:

$$JRC = JRC_{\infty} + (JRC_0 - JRC_{\infty})Exp(-Bt) \quad (3.2)$$

where JRC_0 and JRC_{∞} represent the initial and the residual value of JRC , respectively. The parameter B controls the kinetic of the joint roughness coefficient degradation. If taking equation (3.2) into equation(3.0), we can get degradation function of the regular asperities angle α_0 . Theoretically, the degradation may finally create an idealized smooth surface. That means with the time trends to infinite, the regular asperities angle trends to zero.

Similarly as that of residual friction angle, the influences of the degradation of rock joint asperities are given in Fig. 3.19 and Fig. 3.20. According to equation(3.2), the joint roughness coefficient JRC decreases with the time. As a consequence, the regular asperity's angle decreases also with time as indicated by equation(3.0). Four different velocities represented by parameter B are employed, as illustrated in Fig. 3.19, while for the fourth velocity, *i.e.* $B=1$, after 10 years, the initial rough joint surface becomes as a total smooth surface.

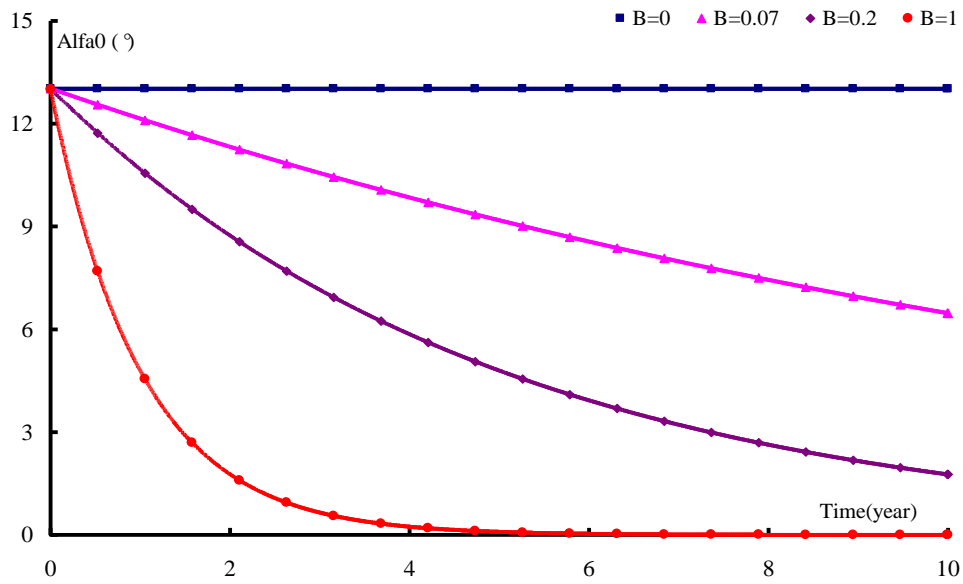


Figure 3.19 The degradation of α in function of time with different velocities

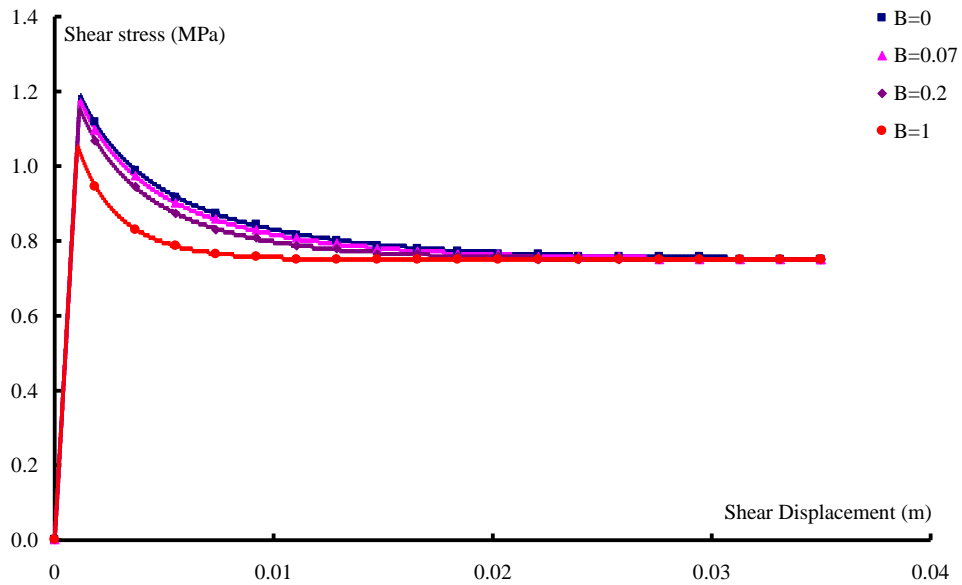


Figure 3.20 Influence of the degradation of α on the mechanical behaviour of rock joint under constant normal stress

Lots of variables mentioned in previous part vary with the variation of this time-dependent JRC . Some simple sensitive analyses are performed to discuss this influence in detail (Tab. 3.4):

Table 3.4 Basic crack parameters for sensitive analyse

parameters	σ_n (KPa)	F (Kpa)	Φ (°)	B	JRC_0	JRC_∞	JCS_0 (MPa)	L (m)	L_0 (m)
value	100	50	32	0.03	18	3	20	0.09	0.09

The sensitive analyses are performed by adjusting these time related parameters to see their influence:

1) Sensitive analyses of parameter B :

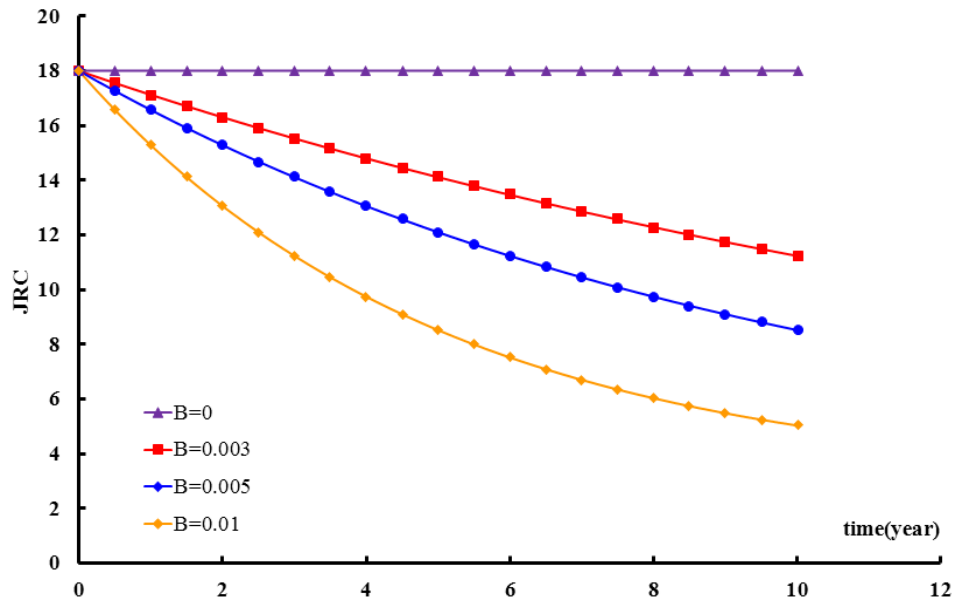


Figure 3.21 Sensitive analyses of parameter B (JRC)

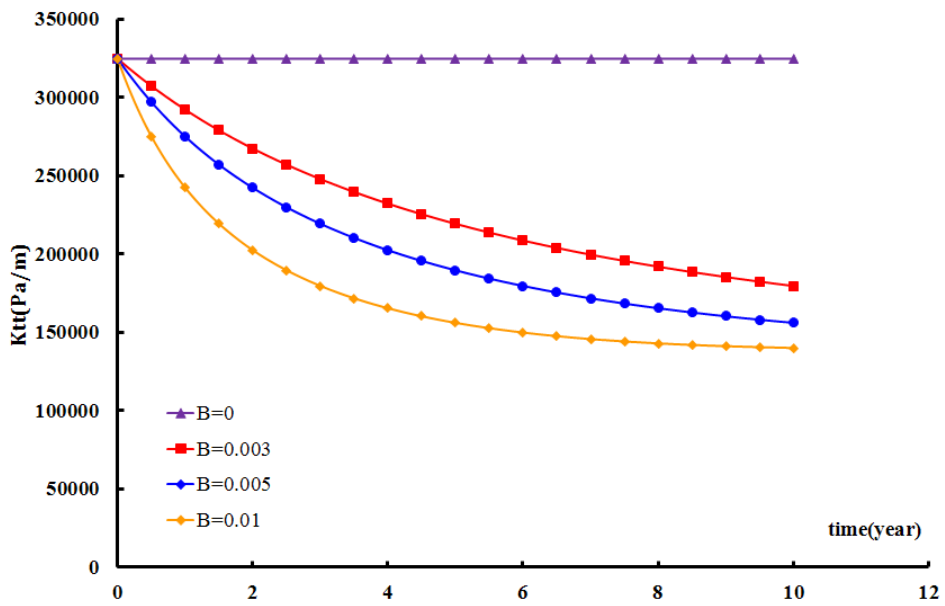


Figure 3.22 Sensitive analyses of parameter B (K_u)

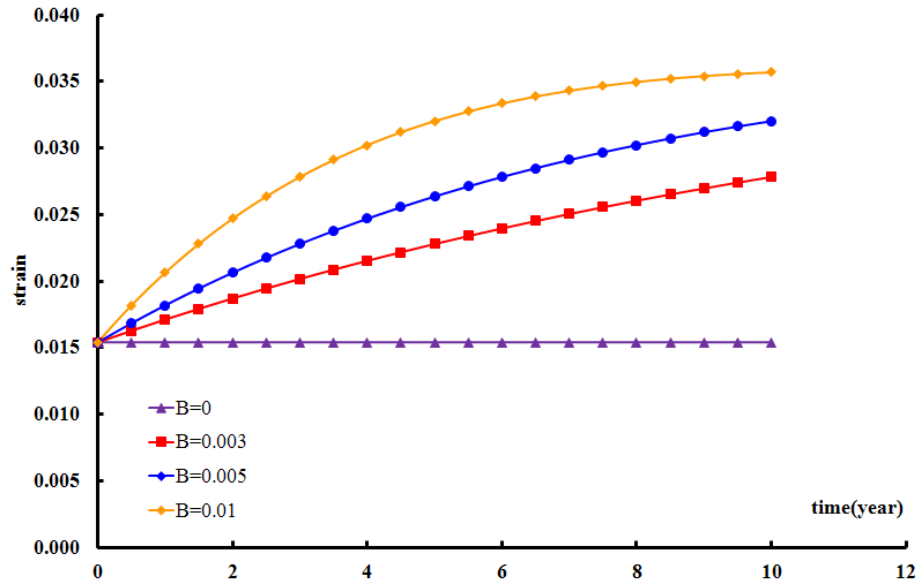


Figure 3.23 Sensitive analyses of parameter B (strain)

Four values of parameter a (0, 0.003, 0.005 and 0.01) are chosen. From the curves we can observe that, the augmentation of the parameter a accelerate the variation rate of JRC with time (Fig. 3.21). Physically, this parameter controls the velocity of the rock joint asperity variation, reduce the resistance ability of rock joint which respected by the K_u value (Fig. 3.22), and then finally induce the time-dependent shear deformation variation (Fig. 3.23), which is exactly creep phenomenon.

2) Sensitive analyses of parameter JRC_0 :

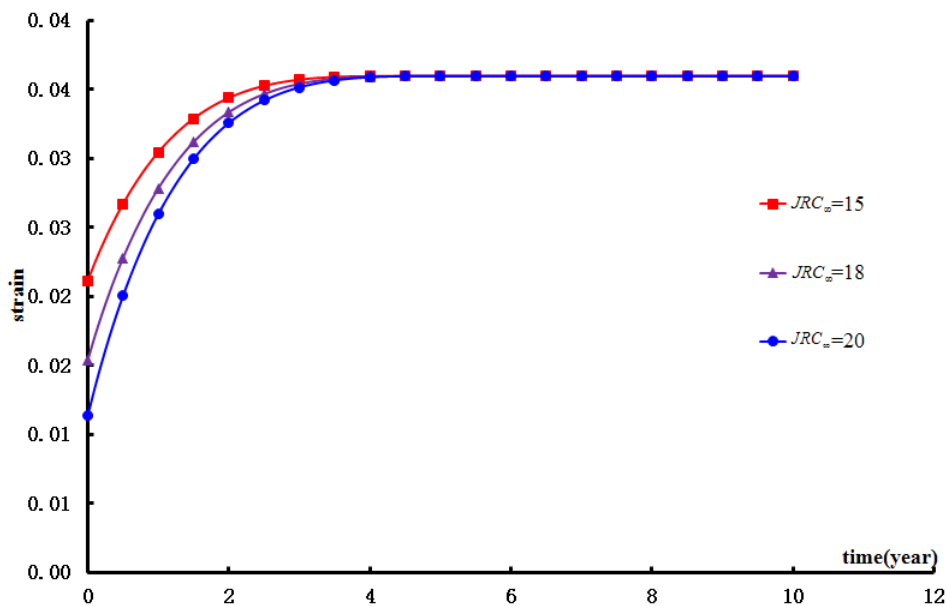


Figure 3.24 Sensitive analyses of parameter JRC_0 (strain)

This parameter JRC_0 of (15) controls the initial point of the variable JRC , which respects the initial asperity state of rock joint. Therefore JRC_0 can also express the initial mechanical property of rock joint, high value of JRC_0 induce the high start point of K_{tt} value and then the low initial value of shear deformation (Fig. 3.24).

3) Sensitive analyses of parameter JRC_∞ :

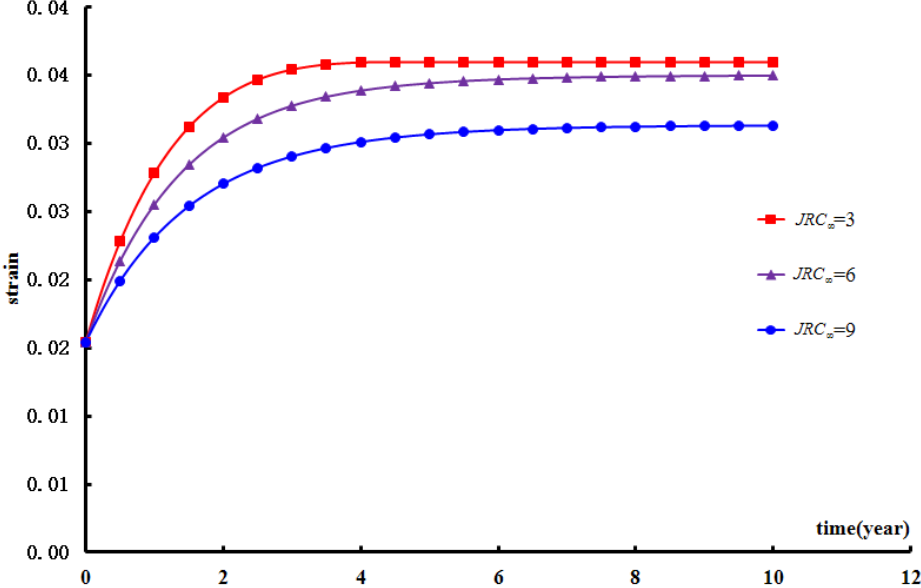


Figure 3.25 Sensitive analyses of parameter JRC_∞ (strain)

Similarly with JRC_0 , the parameter JRC_∞ represents the ultimate state of JRC , K_{tt} , and shear deformation (Fig. 3.25).

4) Influence of normal stress σ_n :

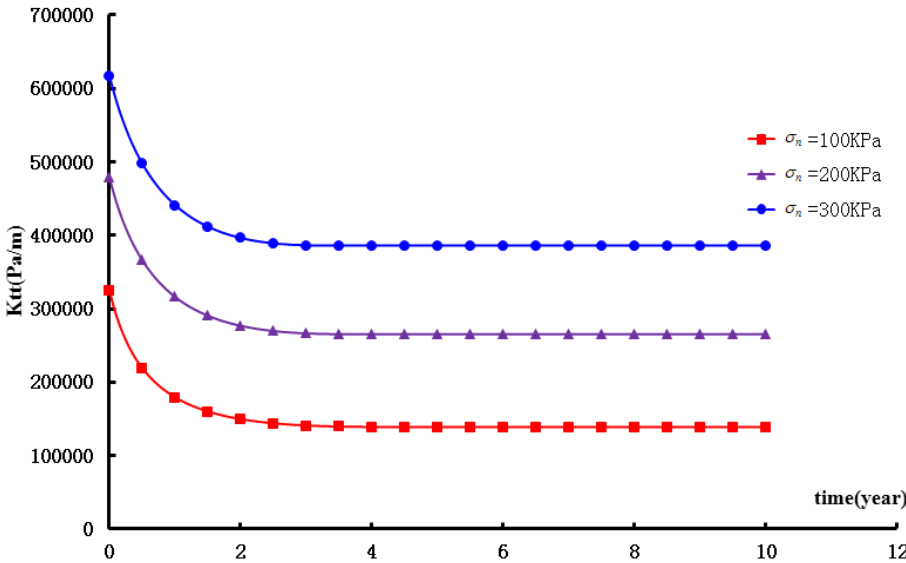


Figure 3.26 Sensitive analyses of parameter σ_n (K_{tt})

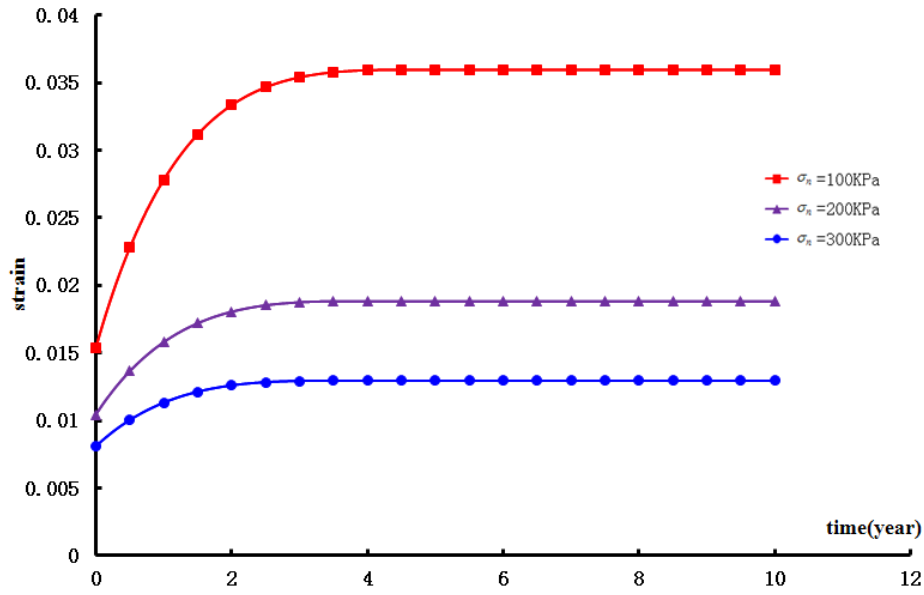


Figure 3.27 Sensitive analyses of parameter σ_n (strain)

When compressed by normal stress, the two surfaces of rock joint are easier to be firmed by grapping each other. Therefore, with the augmentation of normal stress σ_n , the shear stiffness of joint K_n increases (Fig. 3.26), the value of shear deformation of joint decreases (Fig. 3.27).

And then simulations of creep experiments are performed to test the time effect part of this numerical model. The experimental data of slope rocks of Jinping project [87] are applied in the numerical model validation.

With the same normal stress $\sigma_n = 0.75\text{MPa}$, four different shear stresses are imposed: $F = 0.294\text{MPa}$, 0.22MPa , 0.147MPa , 0.073MPa , the model parameters employed are listed in table 3.5.

Table 3.5 Crack parameters for creep simulation of joints

parameters	$\Phi(^{\circ})$	B	JRC_0	JRC_{∞}	JCS_0 (MPa)	L (m)	L_0 (m)
value	40	0.2	18	8	35	0.028	0.1

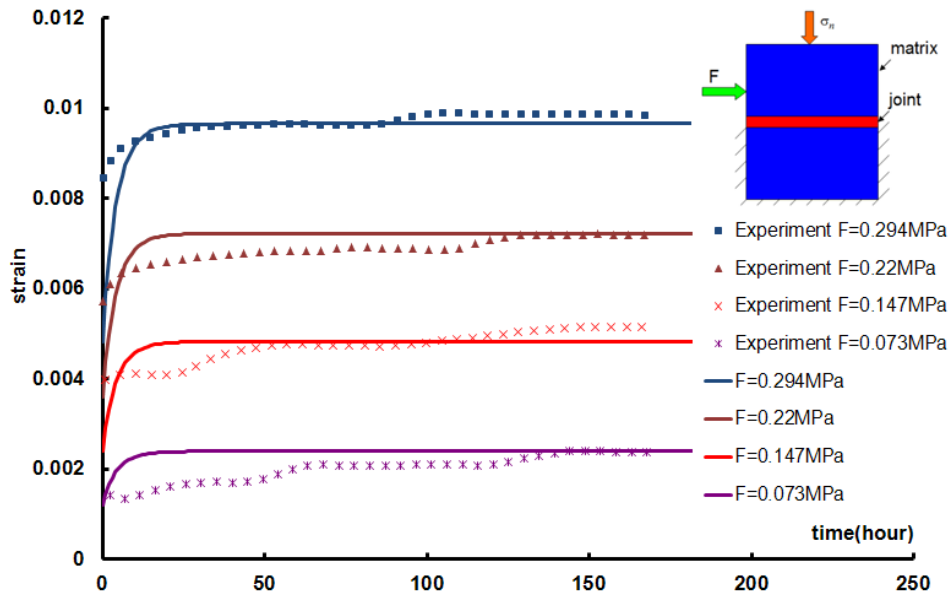


Figure 3.28 Numerical simulation of direct shear tests compared with experimental data

According to the results (Fig. 3.28), it can be observed that with the same parameters employed, under different shear stresses imposed, this numerical model can perform excellently in predicting the creep behaviour.

3.5. Conclusion

In this chapter, a constitutive model based on the continuous medium theory is developed for rock joints. A particular elasto-plastic model is proposed for the rock joint using Mohr-Coulomb yield function by taking into consideration of microstructure and morphology of the joint surface. A non-associated flow rule is adopted in the model to incorporate shear induced degradation of roughness of rock joint surface. And then, the time effects, e.g. the degradation of residual friction angle and the roughness of joint surface are taken into consideration. The present constitutive model essentially employs a number of model parameters in terms of shear stresses and displacements. The results of three experimental studies on natural and artificial rock joints are employed to evaluate the validity of the present model. It shows a good agreement between the measured and predicted responses of the rock joints for all the three cases.

Chapter 4. Numerical method for the jointed rocks

4.1. Introduction

With the efforts and advances made in recent years in both the numerical simulation methods and computational techniques, cracks in rocks (including both the crack initiation and propagation) can be simulated by various numerical methods such as the boundary element method (BEM) [36], the discrete element method (DEM) [37], the numerical manifold method (NMM) [38] and the meshless methods [39]. In addition to the above numerical methods, the extended finite element method (XFEM) [40], which based on the theory of FEM, has been a widely used method for predicting the behaviour of pre-existing crack, *e.g.* the crack initiation and propagation. As the first method for analyzing crack growth without remeshing, this method works by adding enrichment shape functions into the traditional FEM theory in the simulation of discontinuous in fixed meshes. In the numerical simulation of cracked structures under static and later under dynamic loading, XFEM has been successfully applied for several years. It is now becoming an efficient method to reduce the mesh dependencies in macrocracks growth simulation. XFEM has been adopted in this work for the numerical simulation of discontinuous analysis in hard rocks, and both the pre-exist rock joints and crack propagation could be taken into consideration.

In this chapter, the basic theory of the XFEM is briefly recalled, and several numerical implementation techniques are discussed. Finally, several numerical applications have been discussed to illustrate the efficiency of this method.

4.2. Basic theory of XFEM

The basic idea of XFEM is “extending” the nodal displacement for those nodes associated with the elements crossed by cracks. The “extending” nodal displacements represent the “displacement jump”: the discontinuities in the displacement field. If one element is crossed by a crack, the nodes of this element are then enriched by additional degrees of freedom (DOFs). In XFEM theory, the displacement field is decomposed into two parts, as [88]:

$$\vec{u}(x,t) = \vec{u}_n(x,t) + \vec{u}_r(x,t)\varphi(x) \quad (4.0)$$

in which \vec{u}_n and \vec{u}_r are continuous displacement functions. The first one \vec{u}_n is as that in the classical FEM, the nodal displacement vector; while the latter one \vec{u}_r represents the discontinuities, such as the displacement jump cause by the crack. φ is the enriched

approximation basis designed to describe the displacement jump, which is already described in many forms [40, 89-92].

A rock mass occupying a domain Ω crossed by a crack Γ_d with its normal as \vec{n} , as illustrated in Fig. 4.1, is studied. According to the theory of XFEM, the studied domain is divided into two parts: 1) the left side of the crack is considered as the positive part and noted as Ω^+ ; 2) the right side of the crack is noted as the negative part and noted as Ω^- . ($\Omega = \Omega^+ \cup \Omega^-$).

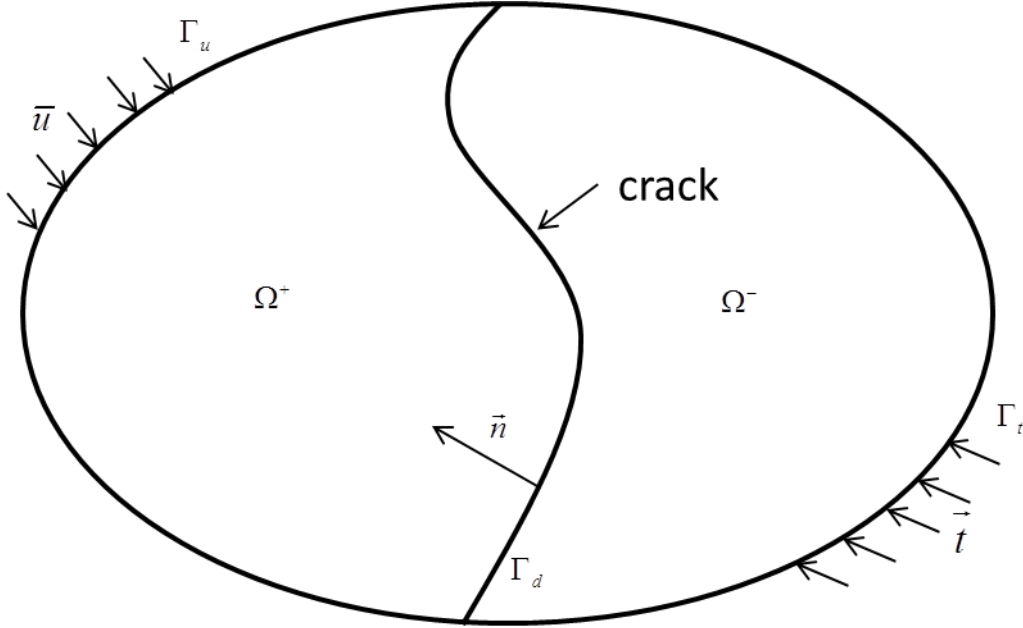


Figure 4.1 A domain crossed by a crack

The simplest and the most efficient technique of enriched approximation basis form is Heaviside jump function, so the displacement field can be written as:

$$\vec{u}(x,t) = \vec{u}_n(x,t) + H(x)\vec{u}_r(x,t) \quad (4.0)$$

where the Heaviside equation is given as:

$$H(x) = \begin{cases} +1 & \text{if } x \in \Omega^+ \\ -1 & \text{if } x \in \Omega^- \end{cases} \quad (4.0)$$

In equation(4.0), the displacement field $\vec{u}(x,t)$ is a continuous function in both Ω^+ and Ω^- , thus it is derivable respectively in each region. So the strain field in Ω^+ and Ω^- can be given as follows:

$$\varepsilon = \nabla^s \vec{u}_n + H(x)(\nabla^s \vec{u}_r) + \delta_{\Gamma_d} (\vec{u}_r \otimes \vec{n})^s \quad (4.0)$$

where ∇ is the gradient operator, δ_{Γ_d} is the Dirac-delta distribution of the discontinuity and \vec{n} is the normal vector to the discontinuity (as shown in Fig 4.1). $(.)^s$ represents the symmetric part of matrix.

In finite element theory, for an element with n nodes, if the displacement of each node is known, the displacement of any point in this element could be determined by using the interpolation function, as:

$$u(x) = \sum_{i=1}^n N_i(x) a_i \quad (4.0)$$

in which $u(x)$ is the displacement at position x , while a_i is the nodal displacement vector, and $N(x)$ is the interpolation function of given x . Finite element interpolation functions are also partitions of unity:

$$\sum_{i=1}^n N_i(x) = 1 \quad (4.0)$$

Similarly, for an element with enriched degree of freedom (DOF) in XFEM, the displacement at any point of given element can be given as:

$$u(x) = \sum_{i=1}^n N_i(x) a_i + \sum_{j=1}^m N_j(x) H_j(x) b_j \quad (4.0)$$

where b represents the nodal displacement vector for those nodes with enriched DOFs. m means the total number of “enriched” DOFs in current element. It is worth mentioned that, for the enriched DOFs, the same interpolation functions have been used, the only difference is the additional Heaviside jump function. Therefore, according to equation(4.0), the strain in the given enriched element can be given directly as:

$$\varepsilon(x) = \nabla^s u(x) = \sum_{i=1}^n B_i(x) a_i + \sum_{j=1}^m B_j'(x) H_j(x) b_j \quad (4.0)$$

where

$$B_i = \begin{bmatrix} N_{i,x} & 0 \\ 0 & N_{i,y} \\ N_{i,y} & N_{i,x} \end{bmatrix}; \quad B_j' = \begin{bmatrix} (N_j H)_{,x} & 0 \\ 0 & (N_j H)_{,y} \\ (N_j H)_{,y} & (N_j H)_{,x} \end{bmatrix} \quad (4.0)$$

Then, the stress field can be determined by using an adequate constitutive law, as:

$$\sigma(x) = D\varepsilon(x) \quad (4.0)$$

where D is the constitutive matrix, which relates the stress and strain. The D matrix can be determined from the constitutive law of the matrix. The D matrix is the elastic matrix when the Hook’s law is applied.

Reconsidering the domain crossed by crack, as shown in Fig. 4.1, the equilibrium equations without taking the body force into account are given as:

$$\text{div} \underline{\underline{\sigma}} = 0 \quad (4.0)$$

with the boundary conditions: the prescribed displacement and external force, as shown in Fig. 4.1:

$$\begin{aligned}\underline{\underline{\sigma}} \vec{n} &= t_d \quad \text{on } \Gamma_d \\ u_i &= \bar{u}_i \quad \text{on } \Gamma_u\end{aligned}\quad (4.0)$$

where $\underline{\underline{\sigma}}$ is the second order stress tensor, determined from the equation(4.0), while \vec{n} is the unit outward normal of boundary surfaces, t_d is the external force on the boundary Γ_t ; \bar{u}_i is the prescribed displacement components on the boundary Γ_u . Generally, the discontinuity is also considered as the “boundary”, as:

$$\underline{\underline{\sigma}} \vec{n} = \vec{t} \quad \text{on } \Gamma_t \quad (4.0)$$

in the equation(4.0), \vec{t} is the stress on the crack surface. If \vec{t} equals zero, the crack is then considered as traction free.

Similar to that of FEM, by applying the virtual work to the governing equations, after series of transformation, the governing equations finally turn to one solvable form, as:

$$\begin{bmatrix} \int_{\Omega} B^T DB d\Omega & \int_{\Omega} (B')^T DB d\Omega \\ \int_{\Omega} B^T DB' d\Omega & \int_{\Omega} (B')^T DB' d\Omega + \int_{\Gamma_d} N^T TN d\Gamma \end{bmatrix} \begin{Bmatrix} da \\ db \end{Bmatrix} = \begin{Bmatrix} f^{ext} \\ 0 \end{Bmatrix} - \begin{Bmatrix} f_a^{int} \\ f_b^{int} \end{Bmatrix} \quad (4.0)$$

In the equation(4.0), da represents the displacement increment for the normal DOF as that in the classical FEM, while db is the displacement increment for enriched DOF. The left side of the equation is the rigid matrix, and the first term is noted as K_{aa} :

$$K_{aa} = \int_{\Omega} B^T DB d\Omega \quad (4.0)$$

this term is exactly the same as that in the classical FEM. If there is no enriched DOF, the matrix in equation(4.0) will be simplified to that as equation(4.0). The other two terms, considering the coupling effects between the "normal" and "enriched" DOF, are:

$$\begin{aligned}K_{ab} &= \int_{\Omega} (B')^T DB d\Omega \\ K_{ba} &= \int_{\Omega} B^T D(B') d\Omega\end{aligned}\quad (4.0)$$

The fourth term represents the contribution of the discontinuous and is expressed as:

$$K_{bb} = \int_{\Omega} (B')^T DB' d\Omega + \int_{\Gamma_d} N^T TN d\Gamma \quad (4.0)$$

The second term of (4.0) represents the contribution of the crack. It should be taken into account when considering the stress on the crack surface, which represents the third boundary conditions, *e.g.* equation(4.0). And T represents the rigid matrix of crack, as that in equation (3.2) in Chapter 3:

$$T = \begin{bmatrix} K_{mm} & K_{mt} \\ K_{tm} & K_{tt} \end{bmatrix} \quad (4.0)$$

The right side of the equation(4.0) is the nodal unbalance force vector. f^{ext} denotes the external force allocated in node, and it can be calculated as that in the classical FEM. While

f_a^{int} and f_b^{int} are respectively the nodal force vector for "normal" and "enriched" DOF caused by the internal force, as:

$$f_a^{\text{int}} = \int_{\Omega} B^T \sigma d\Omega \quad (4.0)$$

$$f_b^{\text{int}} = \int_{\Omega} (B')^T \sigma d\Omega + \int_{\Gamma_d} N^T \vec{t} d\Gamma \quad (4.0)$$

The equation(4.0) can also be given in a simple form. It is exactly the same as that for the classical FEM, as:

$$KU = F \quad (4.0)$$

Essentially, there are no great difference between FEM and XFEM. Based on the classical FEM theory, the XFEM "extended" it by enriching certain nodes of the elements which are crossed by the discontinuous. Coupling the solid fundamentals of the classical FEM with several numerical implementation techniques, as discussed in the next section, the XFEM could be introduced into the applications.

4.3. Numerical implementation

As mentioned above, for taking the discontinuities into consideration, some modification should be taken. In this section, the numerical implementations of the XFEM are discussed.

Theoretically, when referring a classical 2D finite element mesh crossed by a crack, the crack could be any form, and is independent of the mesh (represent by the blue continuous line in Fig. 4.2). However, in the XFEM calculation program, the crack, as that of the calculation domain, should firstly be discretized. In place of the curve line, a straight line is used to replace the real crack in each element crossed by crack, as marked by dotted line in Fig. 4.2.

After defining the crack position, certain nodes should be chosen for the enriched DOFs. The rules for picking these nodes are simple and clear: all the nodes associated with the elements crossed by crack should be enriched. In our case, all those nodes marked with red circle and red squares are the nodes have been chosen as enriched nodes. For each of these nodes, two "additional" DOFs are added for representing the displacement jump caused by the crack.

Furthermore, the crack has its proper direction, as illustrated in the Fig. 4.1 from left to right, and the mesh has been divided into two parts. The chosen enriched nodes have been distinguished for two groups: for those enriched nodes located in the left side (above the crack), they have been marked by the red circles; while for those located in the right side of crack (below the crack), they have been marked by the red square. The reason is that, when calculate the rigid matrix, the nodal displacement or the strain, the Heaviside equation has

been used, e.g. equation(4.0), (4.0) and (4.0). The value of Heaviside equation depends on its position, as indicated in equation(4.0).

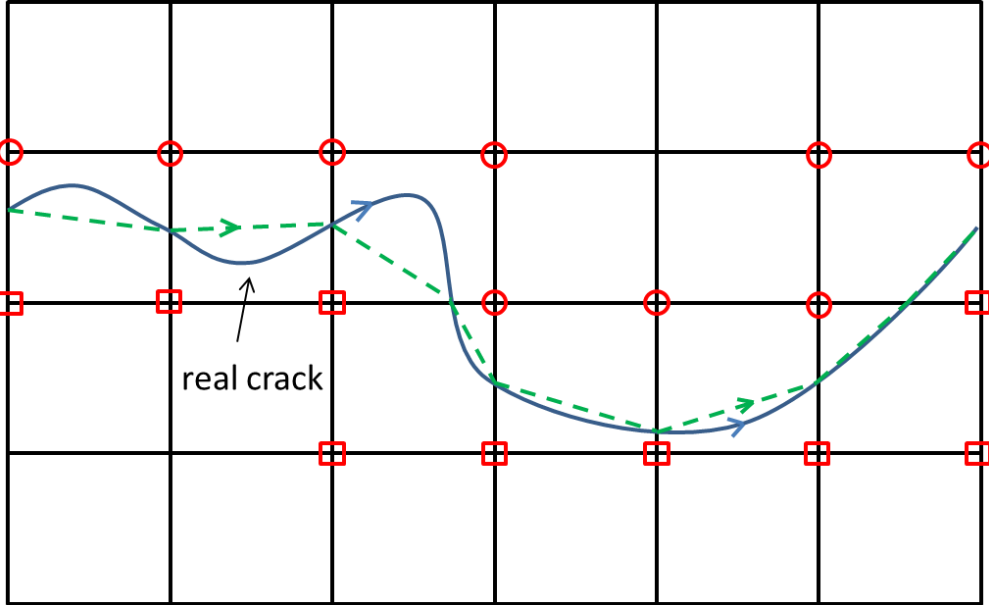


Figure 4.2 A classical finite element mesh crossed by a crack

For a crack crossed element, both the elemental rigid matrix and elemental nodal force vector are expressed as in equation(4.0). For example, when calculating the elemental rigid matrix, the integration should be done all over the element. However, not as that for classical FEM, the function for the integration is no longer continuous, as the Heaviside function has different value in Ω^+ and Ω^- . Therefore, the integration should be performed respectively in each domain. The schema of integration for those elements crossed by crack has been illustrated in Figure 4.3: for both Ω^+ and Ω^- , the domain has been divided into certain number of triangles; in each triangle, three integration points are prepared as that in the classical FEM for the integration. If the discontinuity is not traction free, the stress on the crack surface should be taken into consideration. The integration along the crack surface is illustrated by the red line in the Fig. 4.3. For this linear integration, two integration points are used. It should be mentioned here that, although several triangles and integration points are used for the mathematical integration, these triangles and integration points are determined according to the crack position and element nodes, nevertheless, no new element has been added, and no remeshing is needed, even for the propagated crack.

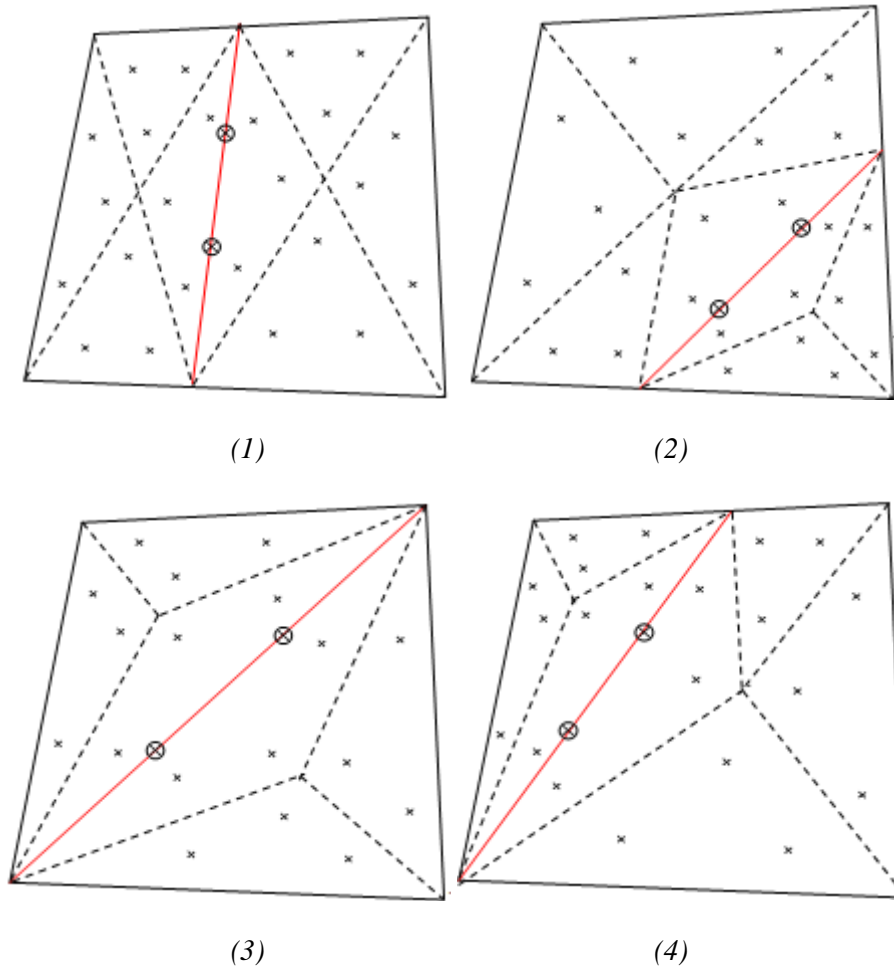


Figure 4.3 The integration schema for a 2D 4node element crossed by crack

4.4. Crack propagation criterions

When the crack propagation should be considered, two important problems arise. The first one concerns the determination of macroscopic crack initiation condition, i.e. the criterion condition for the transition from diffuse damage to localized crack. The second is related to the determination of propagation direction of the macroscopic cracks.

4.4.1. Crack initiation criterion

As discussed in Chapter 2, the macroscopic cracks are the result of coalescence of microcracks. The evolution of diffuse damage by microcracks is controlled by the damage criterion. When the diffuse damage reaches one critical state, the coalescence occurs and macroscopic cracks are initiated. Various macrocrack initiation criteria are proposed in the former researches. In present work, we propose a simple criterion based on a critical damage. In a given element, once the damage attains the defined critical damage, it is supposed that the given element is cracked and a crack should be “created”. The simplest method to identify

this characteristic damage is using the uniaxial test. We suppose that the macroscopic crack occurs when the damage value reaches the characteristic value corresponding to the peak stress state. In numerical implementation, when the damage value at an integration point inside an element reaches the critical value, a macroscopic crack will be inserted in this element by introducing additional degree of freedoms to the element nodes for representing the displacement discontinuities in current cracked element.

For illustrating this criterion, a simple example illustrated in Fig. 4.4 is applied. This example is based on the laboratory test conducted by Camps [93]. In the numerical simulation, the length of the specimen is set as 10cm when the height as 1cm. The boundary conditions are as following: in the left side, the displacements in x direction are blocked, while at the bottom, the displacements in y direction are blocked, a prescribed displacement in x direction of 0.1mm is applied at the right side of the specimen. The beam is divided into 11 elements.

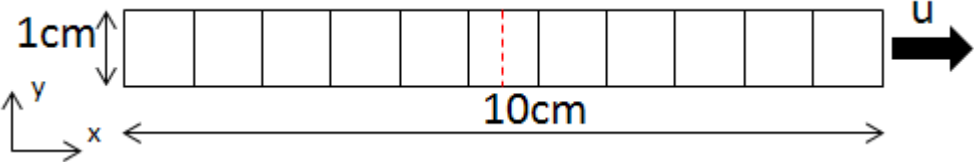


Figure 4.4 A specimen of concret under uniaxial traction

Before the initiation of crack, the damage model presented in chapter 2 has been employed. The parameters for the damage model are listed in Table 4.1. Firstly, by using these parameters, a uniaxial traction test is simulated; the strain-stress relationship is given in Fig. 4.5. In the same figure, the strain-damage curve is illustrated as well. Corresponding to the peak stress, the critical damage is about 0.62 and the value is used as the threshold of the crack initiation, *i.e.* the critical damage.

Table 4.1 Model parameters for concrete under uniaxial traction

$E(\text{GPa})$	ν	B_t	Y_{t0}	$K_n(\text{MPa})$	$f_t(\text{MPa})$	$[u_n]_m(m)$	c_1	ω_0
90	0.2	4250	10^{-5}	90	4	2×10^{-4}	10	0.62

In fact, for the given boundary conditions and the model used, the damage distribution in the specimen illustrated in Fig. 4.4 is uniform. The damage in all the integration points attains the critical damage at the same time since we suppose the concrete is a homogeneous material and a uniform Young’s modulus has been used. In such case, from the point of view of numerical simulation, all the elements will be “cracked”. However, due to the heterogeneity of the material in reality, the distribution of damage could not be uniform. Generally, one crack will firstly take place in the specimen at one point where the damage attains a critical

value. Thus, as a result of an arbitrary chosen, the crack is introduced in the centre of specimen.

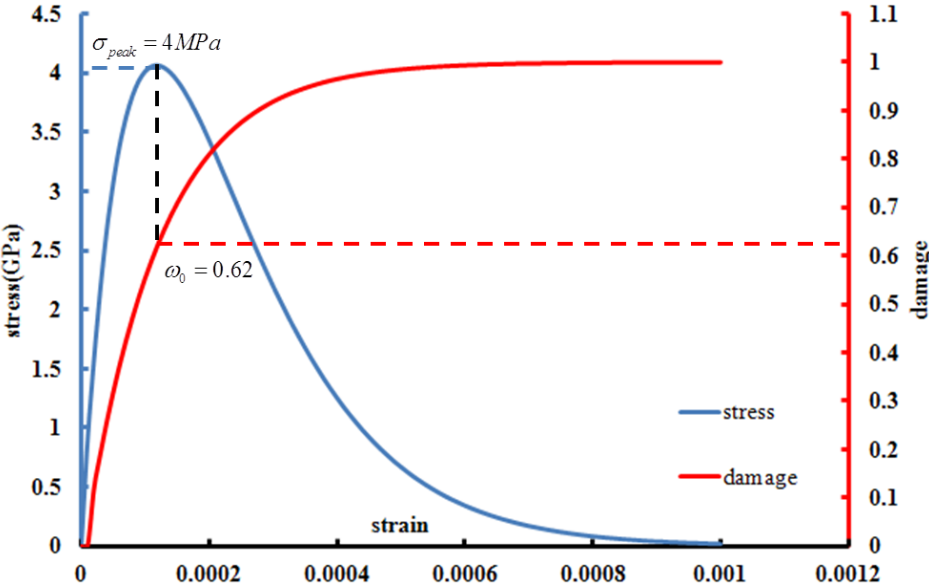


Figure 4.5 Identification of the critical damage for the crack initiation

Once the crack is inserted in the element, an appropriate constitutive law should be used for the crack. The model for rock joint in traction proposed in chapter 3 (3.3) has been adopted here and the corresponding parameters are also listed in Table 4.1. With the “creation” of macro-crack and a “softening” constitutive model for the crack under the increasing loading, the damage in specimen keeps in the critical value.

The tensile strain-stress relationship is given in Fig. 4.6. It should be noticed that the average strain is calculated as the ratio of the prescribed nodal displacement at the right side of the specimen to the initial length of the specimen. There are two distinguished stages: the first one corresponds the diffused damage, with the increase of the traction strain, the stress increases gradually until the damage attains the critical value; the second one corresponds the opening of the crack. With the increase of aperture, the stress decreases exponentially. The result of numerical simulation shows exact agreement with the experimental data.

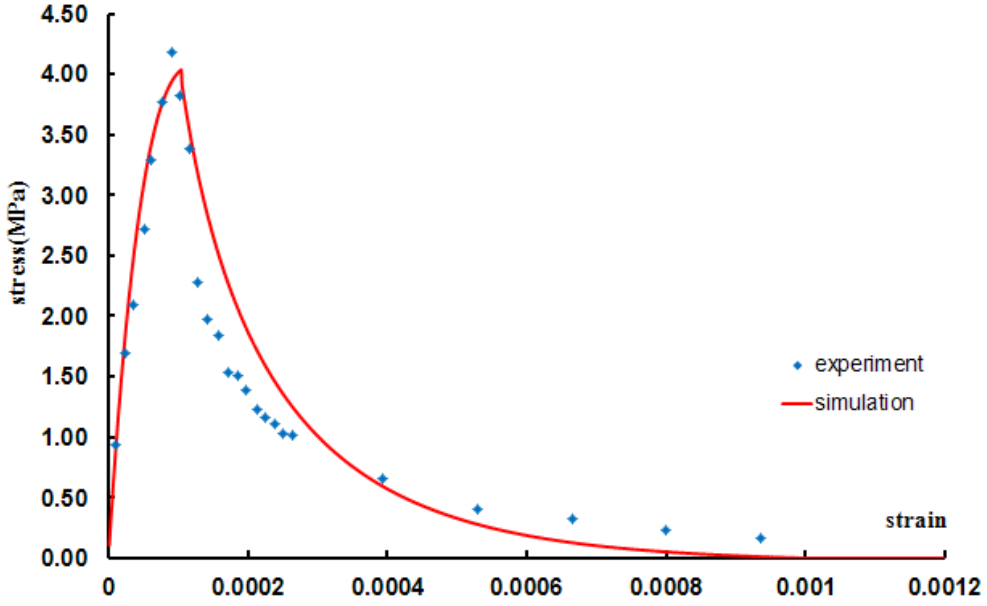


Figure 4.6 The evolution of stress versus strain in the specimen under uniaxial traction

4.4.2. Crack direction

The determination of crack propagation orientation is one of the most difficult issues in modelling the propagation of macroscopic cracks. Different classical criteria have been proposed and adapted: such as the criterion based on the maximum energy release rate, the minimum strain energy density criterion [94, 95], and some other criteria based on the maximum principal stress [96]. Since the tip of a discontinuity is normally located at a point where the stress state isn't known accurately (the discontinuity is independent of mesh), the local stress field cannot be relied upon to accurately yield the correct normal vector to a macrocrack. To overcome this problem, Wells [89] proposed a so-called averaged stress criterion. It is supposed that the crack direction perpendicular to the maximum principal stress (the tensile stress is positive). The averaged stress tensor is computed as:

$$\underline{\underline{\sigma}}_m = \int w \underline{\underline{\sigma}} dV \quad (4.0)$$

w is Gaussian type weight function defined as:

$$w = \frac{1}{(2\pi)^{3/2} l_c^3} \exp\left(-\frac{r^2}{2l_c^2}\right) \quad (4.0)$$

in this expression, r denotes the distance between the current point and the crack tip while l_c is a material characteristic length which determines the extent of interaction zone. The value of l_c depends on characteristic element size. In 2D problem, the material characteristic length is supposed to calculate as:

$$l_c = \sqrt{A_e} \quad (4.0)$$

which A_e the average element surface in a 2D mesh. Once the average stress tensor is determined, the three corresponding principal stresses can be calculated. The new crack direction is assumed to be perpendicular to the maximum principal stress (generally in traction).

4.5. A simple numerical application

In this section, a simple example of "artificial" jointed rock is used to verify and the XFEM program and the time-dependent behaviour jointed rocks. As illustrated in Fig. 4.7, the example concerns a straight pre-exist joint in a regular rock mass. A regular mesh with 1250 4-node elements has been established for the numerical simulation. As given in Fig. 4.8, two straight pre-exist joints with inclined angle as 13.5° and 45° located at the center of the rock matrix, the position of these two "joints" is independent of the mesh. In these two cases, the body force caused by gravity is neglected. The initial strain and the initial stress in the jointed rock mass, as well as on the crack surface, are supposed as zero. The external load is a pressure stress applied at the top of rock mass.

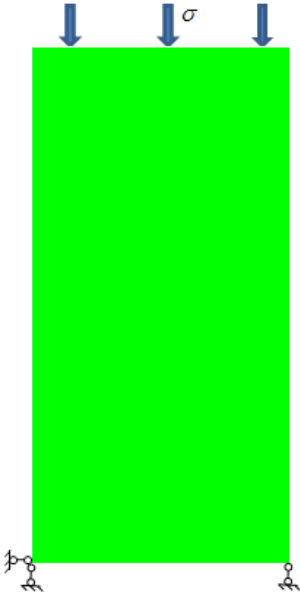


Figure 4.7 The geometry and boundary conditions of a rock mass

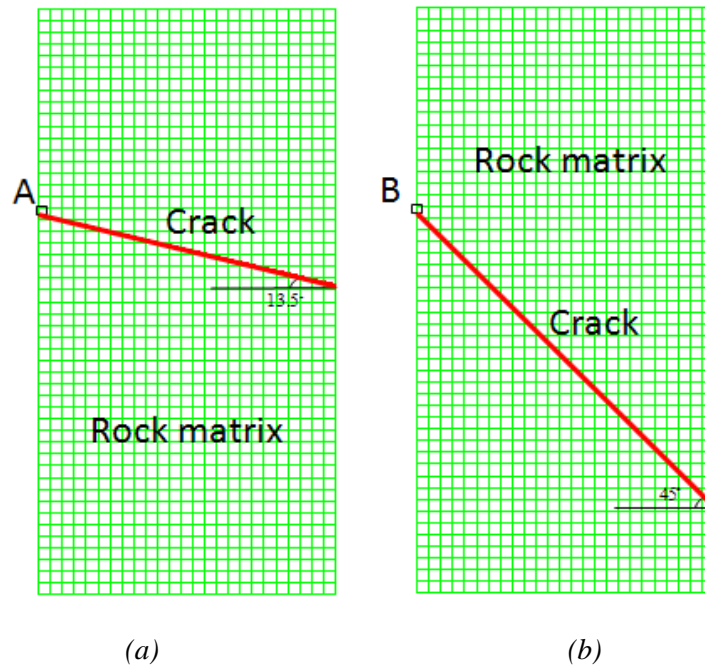


Figure 4.8 The given mesh and the two pre-existed joints with different incline angles

For the reason of simplicity, the rock matrix is supposed as a homogenous, isotropic, elastic material, with Young's modulus as 20GPa and Poisson's coefficient as 0.2. While for the rock joint, the simplest linear-elastic constitutive relation is used. The normal stiffness is supposed as 10^6 GPa to prevent the penetration of one part into another. While the tangent stiffness, with a value of 10MPa, is relatively small when comparing with the Young's modulus of the rock matrix. In this case, under the compression stresses applied at the top the rock mass, the half part above the crack will slide along the pre-exist crack toward the right side the rock mass.

The calculation is divided into two stages. The first one concerns the loading stage, the stress at the top the rock mass (0.1MPa) has been applied instantaneously. The final displacements for these two cases are given in the deformed mesh as given in Fig. 4.9. In such two simple cases, the results can be given directly by simple mathematic analysis. The calculation code gives exactly the same results as that given by theoretical analysis.

It is worth to indicate that, with the same geometry configuration, the same external boundary conditions and the same model parameters, the difference of the incline angle of the crack leads to the distinct final results.

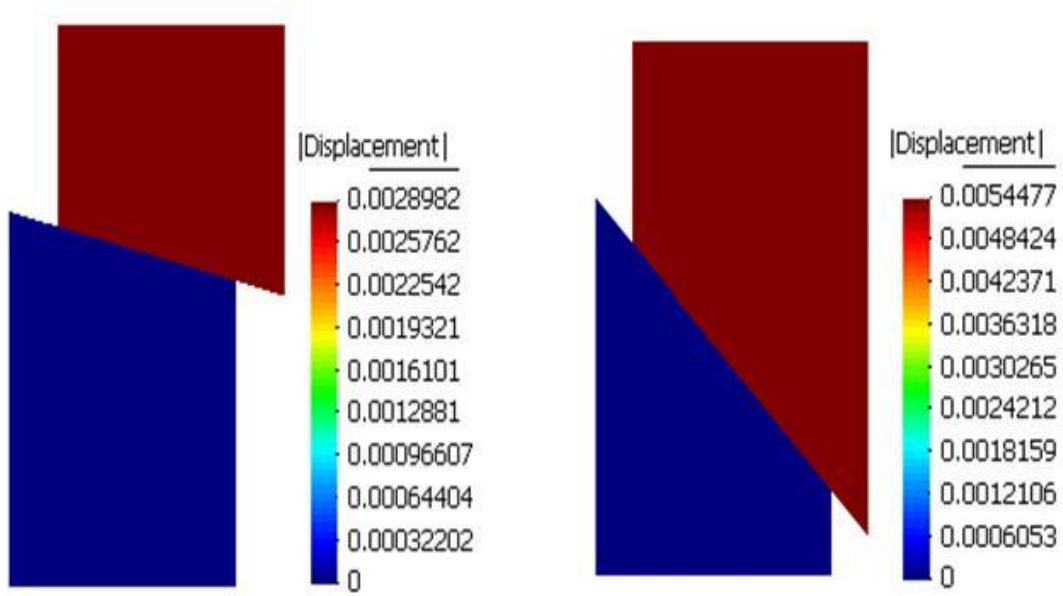


Figure 4.9 The final displacement of two simulations on the deformed mesh

The second stage concerns the degradation of joint with the increase of time, *i.e.* the shear resistance of the rock joint decreases with time. For the reason of simplicity, a simple exponential formulation is proposed for the shear stiffness of the rock joint, as:

$$K_t = K_{t_0} - dK_t [1 - \text{Exp}(B_1(t - t_0))] \quad (4.0)$$

where K_{t_0} is the initial shear stiffness of joint, dK_t is the total shear stiffness degraded during the long-period, B_1 controls the velocity of the degradation, t_0 prescribes the initial moment of the creep phenomenon. Because there is no adequate experimental observations, the parameters chosen here is a little arbitrary. The Young's modulus and coefficient of Poisson are coming from the laboratory observation of typical Marble rock. We suppose during 100years, the shear stiffness of rock joint has reduction of 1 MPa . The kinetic of the degradation is controlled by parameter $B_1 = 0.1$. All the parameters employed in this simulation are listed in Tab. 4.2. These parameters are used for both the two incline joints.

Table 4.2 Parameters for the simulation of simple slope

$E(\text{GPa})$	ν	$K_n(\text{GPa})$	$K_{t_0}(\text{MPa})$	$dK_t(\text{MPa})$	B_1	$\sigma(\text{MPa})$	$t_0(\text{s})$
20	0.23	10^6	7.5	1	0.1	0.1	1

The displacement of Point A and B, respectively for the two inclined joints are given in function of time in Fig. 4.10, as well as the degradation history of the tangent stiffness of the joint. It is obvious that with the same kinematic of degradation, the inclination of the joint has a big influence on the "landslide" observation. With the incline angle increase, the stress along the joint surface increases (shear stress component). During the degradation period, the shear stress remains constant, with the reduction of the shear stiffness, the shear displacement

increases. This example shows that the joint direction is important for the mechanical behaviour of the jointed rock.

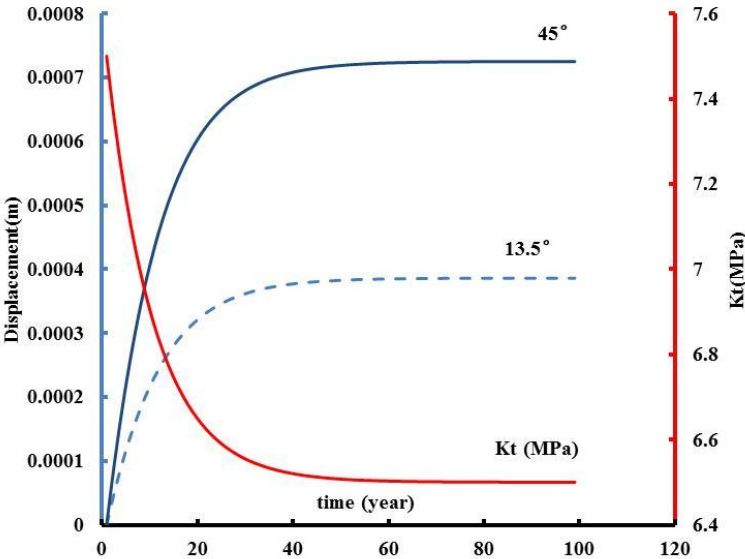


Figure 4.10 The time history of the displacement of Point A and B respectively for the two inclined joint and the time history of the degradation of K_t

By modifying the parameter dK_t from 1MPa to 7.5MPa, which represents the joints are completely stress free (shear stress) after 100 years. In this case, the time-displacement curves of Point A and B are given in Fig. 4.11. These lines are similar to that third stage of typical creep. The stable state at the end of 100 years in Fig.4.10 could not be maintained, and the displacement will continue to increase until the totally rupture of the structure.

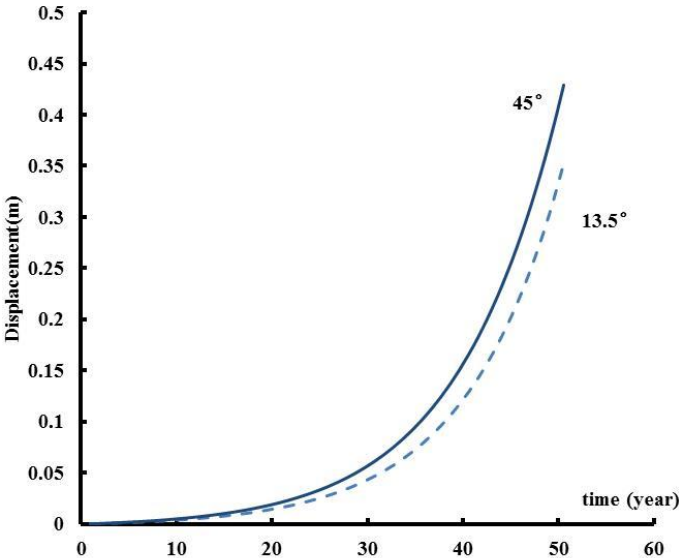


Figure 4.11 The time history of the displacement of Point A and B respectively for the two inclined joint

For the second stage, in place of the simple elastic model, the more sophisticated model which can reflect better the real joint conditions proposed in the chapter 3 (section 3.4.2) is used. It is supposed that, with the time increases, the asperities of the joint surface degrades, *i.e.* the JRC decrease with the increase of time. The model parameters are listed in Table 4.3. The variation of the JRC in function of time is illustrated in Fig. 4.12, the kinetic of JRC are the same for the two inclined joints. However, as given in Fig 4.13, there is a little difference for the average roughness angle α_0 between the two joints. That is because the normal stresses applied on the two joint surfaces are not the same. In fact, in case of 13.5° , the stress component in the normal direction of the joint surface is greater than that of 45° .

Table 4.3 Model parameters for the JRC degradation

Parameters	$\Phi(^\circ)$	JRC_0	JRC_∞	JCS_0 (MPa)	B
value	32	18	3	28	0.003

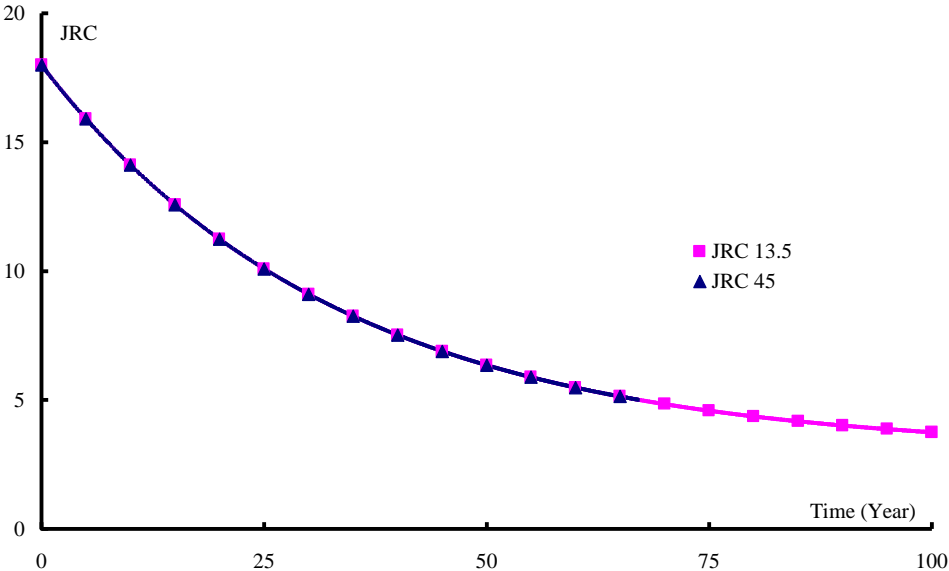


Figure 4.12 The variation of the JRC during the 100years for the two inclined joint

The shear displacement along the joint surface at Point A and B, for the two joints with respectively the incline angle as 13.5° and 45° are given in Fig. 4.14, and compared with the variation of the shear stiffness of the joint. Although there is a little difference in α_0 for the two cases caused by the different applied normal stresses, the difference in the shear stiffness for the two cases is negligible. We can find that the shear displacement in case of 45° increases rapider than that of 13.5° . This is because of the difference of the applied shear stresses on the two joint surfaces. In fact, in case of the 45° , the applied shear stress is more important than that of 13.5° .

It is worth mentioned, in Fig. 4.14, for the joint with an incline angle as 13.5 °, with the degradation of the JRC, the shear displacement is stabilised at the end of calculation. The applied shear stress is always located in the elastic domain. While for the case of 45 °, at the 67th years, the applied stress attains the shear resistance of the degraded joint, and the applied shear stress is the same as that of joint resistance. With the further degradation, the joint surface could not resist any more, and thus the rupture happens.

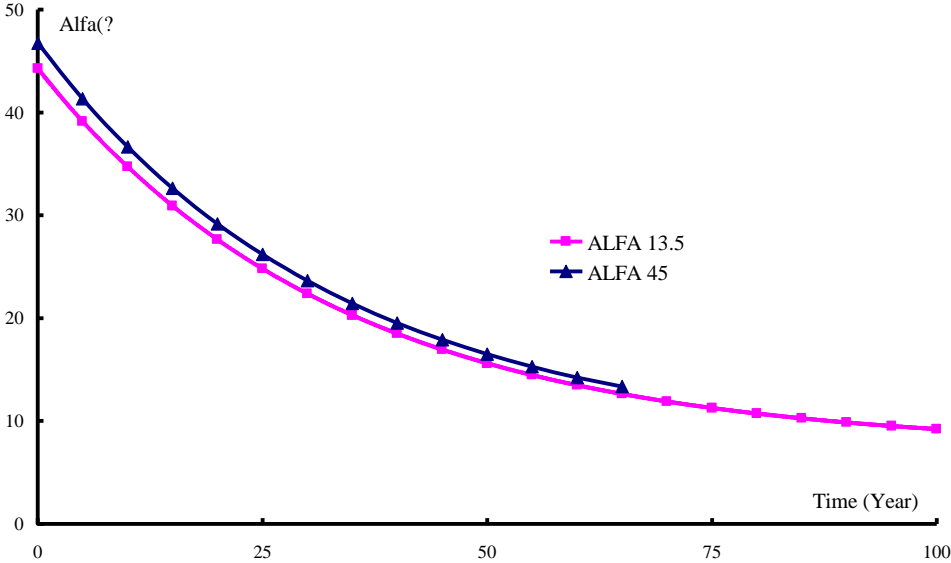


Figure 4.13 The variation of α_0 during the 100years for the two inclined joint

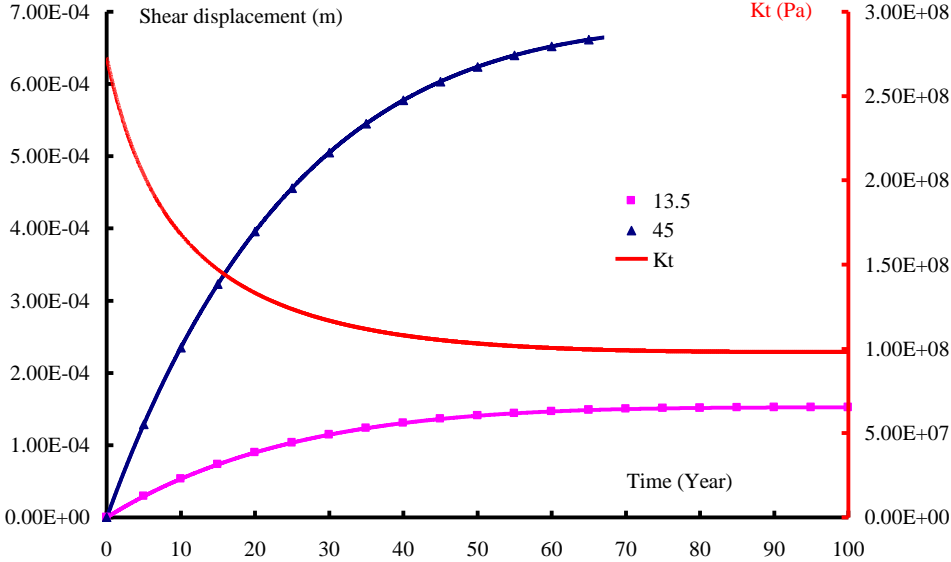


Figure 4.14 The time history of the displacement of Point A and B respectively for the two inclined joint and the time history of the degradation of Kt

4.6. Conclusion

In this chapter, XFEM theory is briefly recalled, and the numerical implementation techniques are discussed. The criterion based on the diffuse damage for the crack initiation is discussed based on a simple traction example. The crack propagation direction is given by an average stress based criterion. Finally, the efficiency of XFEM is illustrated by two simple jointed rock mass examples and the degradation of the rock joint has been also illustrated clearly. The XFEM could be ideal numerical tools for simulating the jointed rock mass in both short-term and long-term behaviours.

Chapter 5. Long-term stability analysis of a jointed rock slope

5.1. Introduction

In this section, the proposed numerical method will be applied to study the long-term stability of a jointed rock slope. The studied slope is one of the hydraulic projects presented in the first chapter. As illustrated in Fig. 5.1, the typical jointed rock slope is located in a narrow valley, with the river width about 80m~100m and the depth 6m~8m. The rock slopes at both sides of this river are solid and steep, which consist one typical deep “V” river valley. The main geometrical components of these slopes are marbles and meta-sandstones.



Figure 5.1 The typical V valley with two high steep rock slopes at both side

The left bank is typical reverse slope, its strata strike is basically same with the valley-side slope direction ($30^{\circ} \sim 40^{\circ}$). In the slope part above 350m, the main component are meta-sandstones (incline $40^{\circ} \sim 50^{\circ}$), below 350m, the slope is mainly constituted by marbles (incline $50^{\circ} \sim 70^{\circ}$). Lamprophyre veins expose in both two banks of the valley, because of the tectonic movements, the contract surface of lamprophyre veins and surrounding rocks developed into structural surfaces, which may gravely affect the slope stability of the banks, and thus are regarded as the joints.

In the left bank, the weathering effect mainly concentrates in low-hardness rocks *e.g.* lamprophyre veins, or structural surfaces in the left bank. However, other rocks are weakly weathered and lightly abraded, that's because the high hardness and high weathering resistance of marbles and meta-sandstones, which are the main components of the left bank.



Figure 5.2 The height steep rock slope during the phase of excavation

As mentioned before, because of the great height, the steep (Fig. 5.2) and the complicated geometrical and topographical condition of left bank, the slope stability is one of the most important issue in the whole hydraulic project. Until now, a lot of analyses are already performed for left bank stability during construction. Furthermore, after the

construction of the project, the eventual degradation of the "joint" will be one of the significant factors in rock deformation, during the long period of the operational stage. The rheology behaviour of left bank rocks under different water level and the long-term stability are important problems concerned. Therefore, the analyses of long-term stability of the structure are cardinal significant for the project.

5.2. The geometry and the boundary conditions

With fully consideration of the slope geological representation and the monitoring results, one typical section (Fig. 5.3) is chosen.

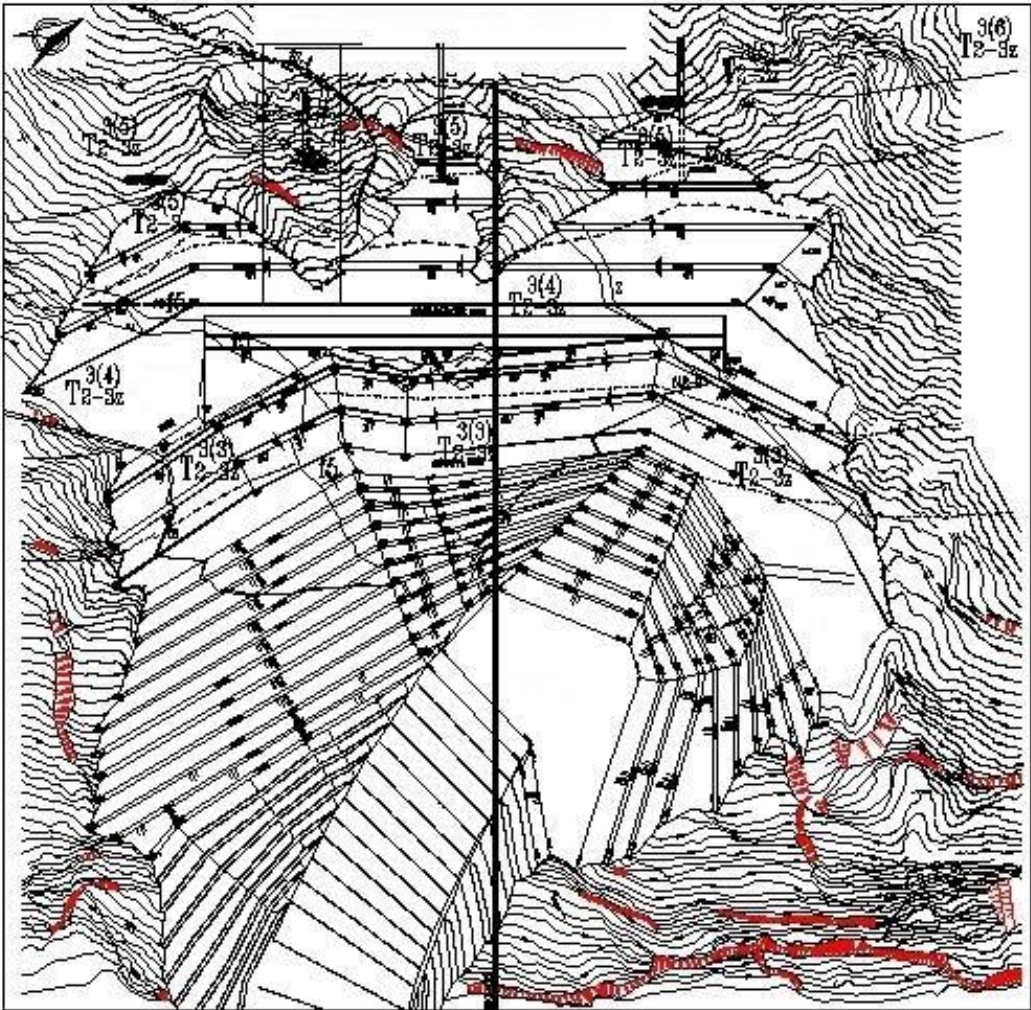


Figure 5.3 Position of the typical section chosen for study

The geometry of chosen section is given in Fig. 5.4. This typical section has a height as 847.75m, and the width is 753.9m. The global coordinate is set as that illustrated in Fig. 5.4, the horizontal line is set as global X-axis. The rock in the given section can be distinguished as two main groups: the marble rock and the meta-sandstone. However, according to the

Chinese classification method[97] which is based on rock rigidity, completeness and the degree of degradation, the rocks can be classified into 5 grades and 2 sub-grades for each grade (grade I 1 to grade V2 represent the solidest to the weakest groups). In the present section, there are totally 7 groups as illustrated in Fig. 5.4 and listed in Table 5.1.

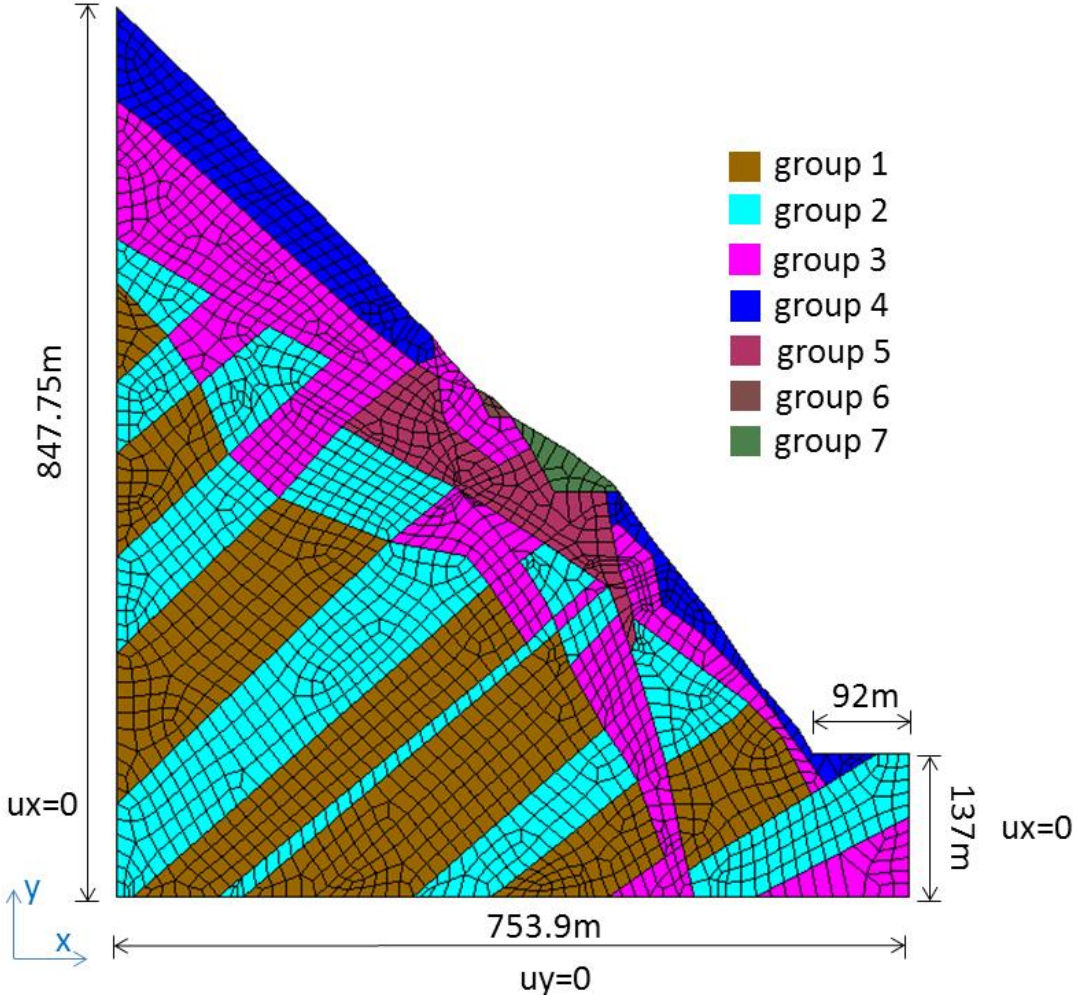


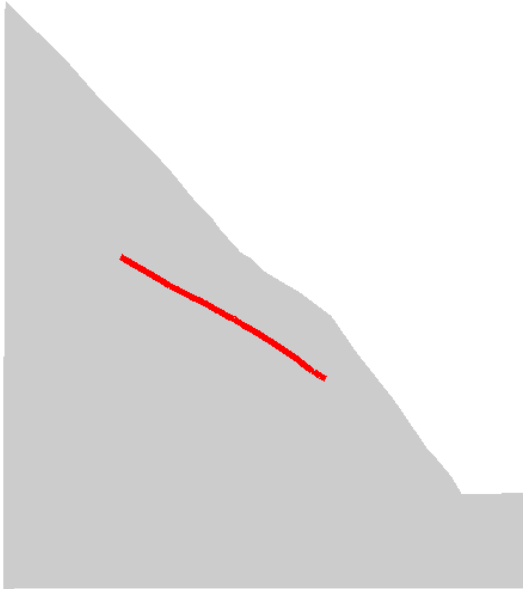
Figure 5.4 Geometry, boundary conditions and material groups

Table 5.1 The rock groups in the chosen section

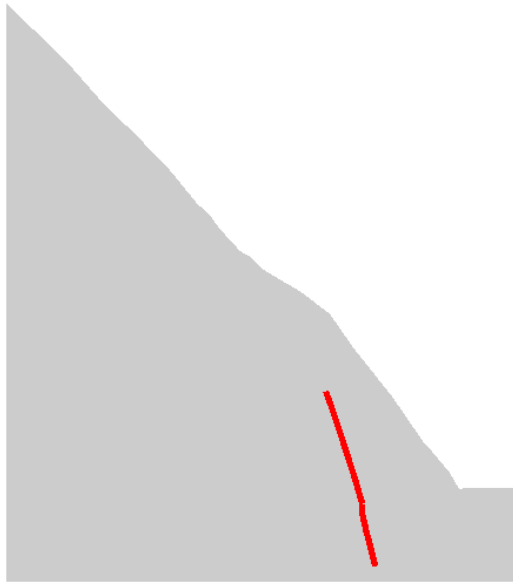
Group	Classification
1	grade II
2	grade III1
3	grade III2
4	grade IV1
5	grade IV2
6	grade III2
7	grade IV1

The chosen section is discretized into 2061 4node-elements, with 2178 nodes altogether. The boundary conditions are: two prescribed zero horizontal displacements are applied at right and left side respectively; a prescribed zero vertical displacement is applied at the bottom of the structure. This 2D case is a typical configuration of plane strain problem.

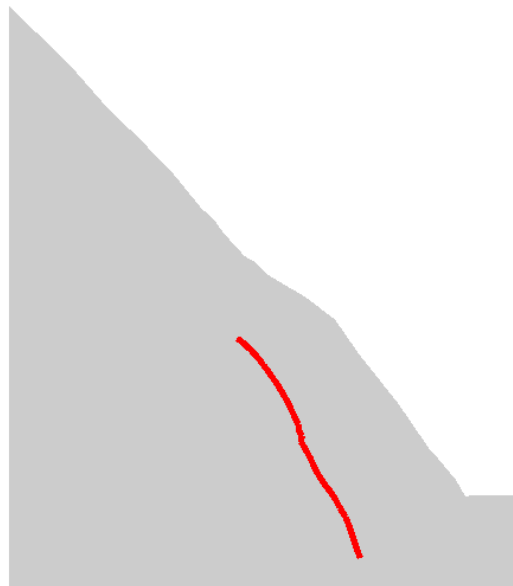
In this typical section, there are three deep "joints", which represent the Lamprophyre veins, the weak and vulnerable material. In fact, lamprophyre and broken belt don't consist big proportion in this rock slope, but they are the most fragile part of the structure, deformations tend to concentrate in these joints, degradate the material strength, and then could finally cause slip of joint surfaces and the failure of the whole structure. The position of the three "joints" are illustrated in Fig. 5.5. The Joint N¹ has a incline angle about 30° while the Joint N² and Joint N³ have the incline angle as 75° and 61° respectively.



(a) The position of the joint N¹



(b) The position of the joint N 2



(c) The position of the joint N 3

Figure 5.5 The position of the three main joints in the rock mass

In this study, the only external load is the gravity. The numerical simulation has been divided into two stages. The first stage concerns the application of the gravity to get the distribution of the initial stress. And then, in the second stage, the gravity keeps as constant, and the mechanical properties of rock joints "degrade". The objective of this calculation is to find the influence of the "degradation" of the rock joints on the redistribution of the stress, the displacement and the damage, and finally, to evaluate the long term stability of the rock slope.

5.3. The models and parameters

According to [97] and [98], the geometrical properties of rocks from grade I to grade V are listed below (Tab. 5.2).

Table 5.2 Properties of rocks in different grades (according to [97] and [98])

Ranking grade	Young's module (GPa)	Poisson Ratio	Compressive stress (MPa)
I	>33	<0.2	>250
II	33~20	0.2~0.25	250~100
III	20~6	0.25~0.3	100~50
IV	6~1.3	0.3~0.35	50~25
V	<1.3	<0.35	25~0

By comparing the classification of rock materials listed in Tab. 5.1, the essential mechanical parameters for each group in the slope are given in Table 5.3:

Table 5.3 Essential mechanical properties of each rock group

	Ranking grade	Young's module (GPa)	Poisson Ratio	Compressive stress (MPa)	Density (kg / m^3)
group 1	II	25	0.23	110	2770
group 2	III1	15	0.25	80	2700
group 3 and 6	III2	10	0.28	65	2700
group 4 and 7	IV1	5	0.3	42	2600
group 5	IV2	3	0.35	30	2600

The elasto-damage model presented in Chapter 2 is used for the 7 different rock groups. In the elastic damage model, the parameters B_c and B_t respectively control the evolution kinetics of the compressive and tensile damage. In this model, the peak value of the stress-stain course is compared with the compressive strength of the material. As there is no sufficient data in the traction, the traction strength is arbitrary supposed as 10% of the of compression strength. Therefore, the B_c and B_t are adjusted to achieve the peak compressive/traction strength for each material. The damage threshold in both compression and traction are supposed as zero, i.e. $Y_{c0} = Y_{t0} = 0$. While the parameter controlling the influence of confining pressure is set as $n = 1$. The model parameters for all the 7 groups are listed in Table 5.4.

Table 5.4 Damage parameters for 7 rock groups

Materials	group 1	group 2	group 3, 6	group 4, 7	group 5
B_t	850	850	750	600	500
B_c	320	200	130	90	60

While for the rock joints, the identification of the model parameters is not so easy. Few experimental results are available for this situation. By comparing the essential rock properties and main parameters used for the three joints are listed in Table 5.5.

Table 5.5 The essential parameters used for the three joints

parameters	$\Phi(\circ)$	B	JRC_0	JRC_∞	JCS_0 (MPa)
Value	30	0.05	18	7	28

5.4. Numerical results and discussions

The numerical results are presented and discussed in this section. These results include the nodal displacement history during the "degradation" stage, the distribution of the displacement, the stress and the damage caused by the degradation of the mechanical properties of rock joints.

The distribution of the initial stresses has a great influence on the global mechanical behavior and the deformation properties. Technically, the measurement of the in situ stress is difficult, therefore there is no sufficient information about the in situ stress distribution. The stress due to the gravity are calculated and served as the initial stress for the next stage of calculation. We suppose that during the stage of gravity application, there is no induced damage. Thus, in this stage, elastic model is employed for the entire 7 rock group. The distributions of the stresses induced by the gravity are illustrated in Figure 5.6. Due to the 7 different rock groups and the non-homogenous density, the distribution of stress is not homogenous. And at certain place, such as the material interfaces and the structure boundaries, the stress concentration is observed.

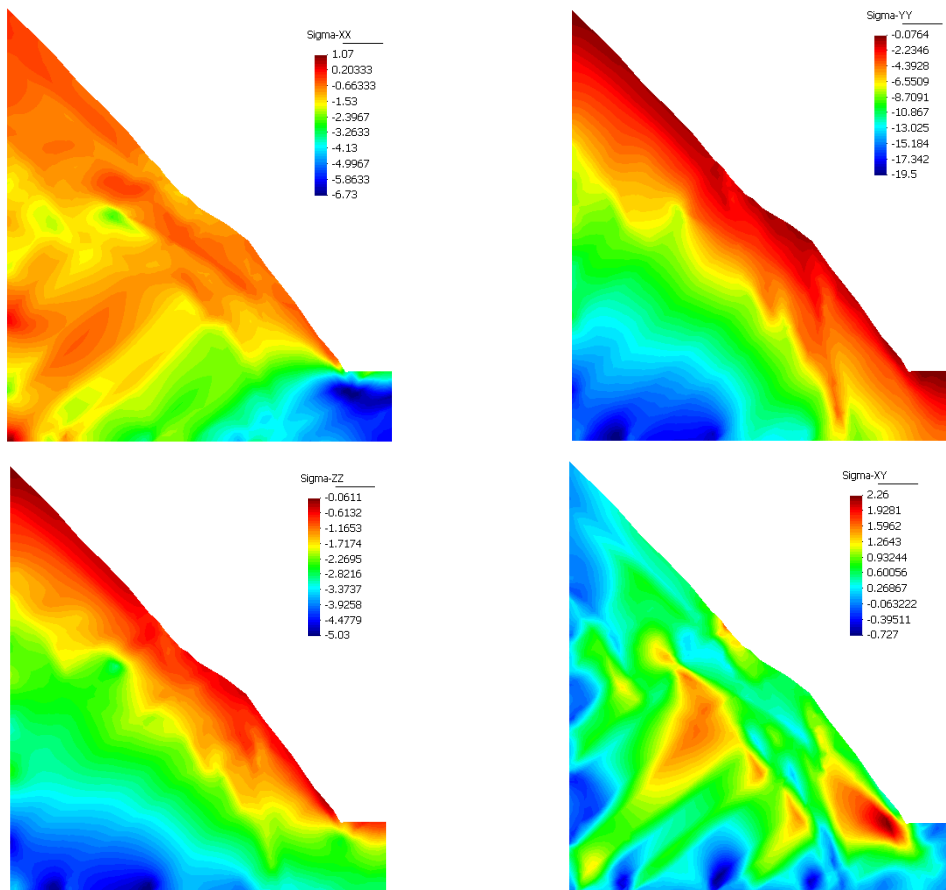
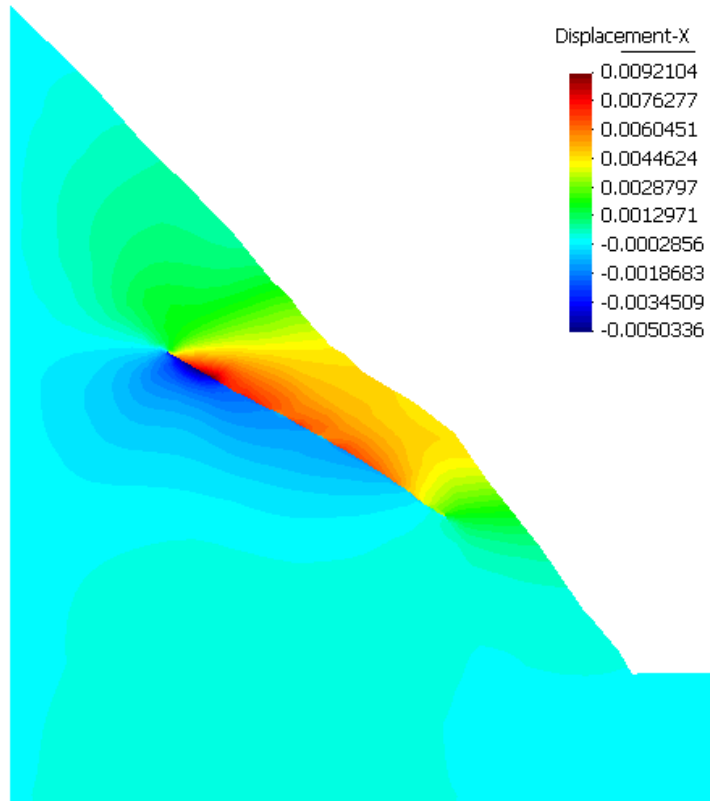


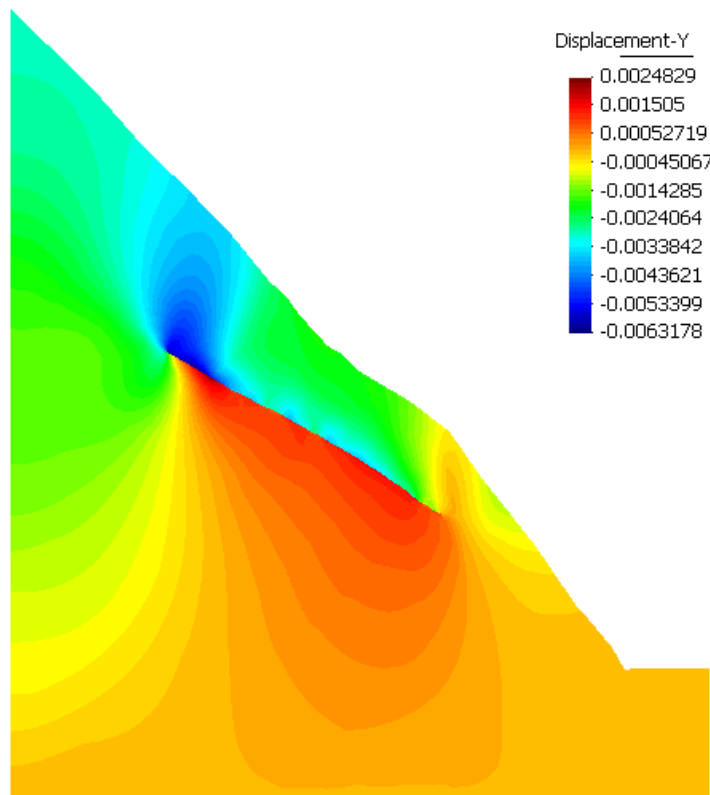
Figure 5.6 The distribution of the stress in the rock mass due to the gravity

5.4.1. Numerical results for Joint N 1

The final displacements in both X and Y due to the rock's degradation are presented in Fig. 5.7. It is worth to be mentioned that the displacements presented in the Fig 5.7 are the "pure" displacement in the second stage ("degradation" calculation). The displacements induced by the gravity are reset to zero at the beginning of the second stage of calculation. Due to the "release" of the shear stress on the rock joint surface, a "slide" along the joint surface is observed in the displacement filed. Namely, for the horizontal displacement, as illustrated in Fig. 5.7(a), the rock above the joint surface has a tendency to slip to the right side, *i.e.* the positive X direction; while the part below the joint has an inverse tendency (displace in the negative direction of X-axis). While for the vertical displacement, as illustrated in Fig. 5.7(b), the rock above the joint surface has a tendency of slip down (to the negative direction of Y-axis), and the rock below the joint has a tendency to raise (in the positive direction of Y-axis). The shear stress is initially resisted by the joint surface, and then the resistance released progressively with the degradation of the joint asperity in shear direction. The release of shear stress induces the "rebound" of the displacement.



(a) The distribution of the displacement in x direction



(b) The distribution of the displacement in y direction

Figure 5.7 The distribution of the displacement in section N-I

The final stress states induced by the “degradation” process are presented in Fig. 5.8. Similar to that of the displacement, the initial stresses have been removed from the final stress state. The main propose of this calculation is to investigate the influence of the "degradation" on stress distribution. Globally, the perturbation in the stress field is "local", *i.e.* the important variations of stress mainly concentrate at the two terminals of the joint. In fact, due the "release" of the shear stress on the joint surface, the stress initially resisted by joint has been relayed by the rock with more resistance. As illustrated in Fig 5.8, the released stress due to the degradation of joint has been transferred to the two terminals, especially the upper terminal, in where concentrated traction stress is observed.

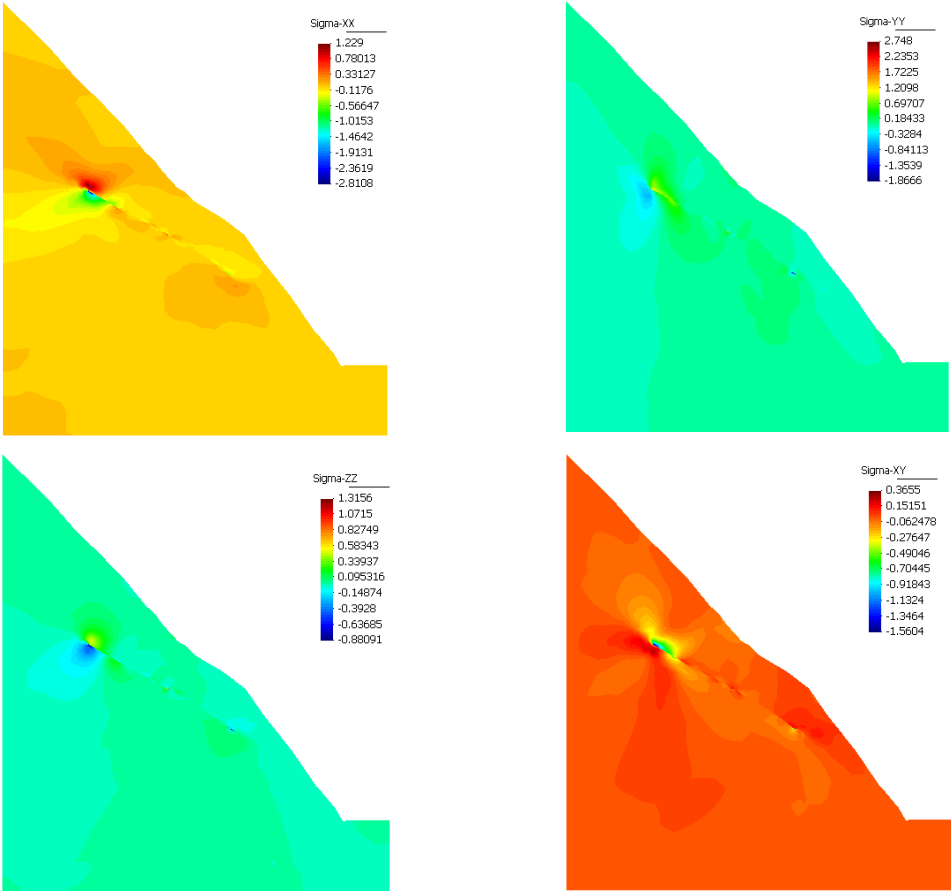


Figure 5.8 The distribution of the stress in the rock mass due to the joint degradation N^I

The distribution of the damage is presented in Fig. 5.9. This is also the "pure" damage due to the joint degradation (as in the first stage where the gravity is applied, there is no damage). The damage mainly concentrates near the joint surface, especially at the two terminal points because of the "strain concentration" (stress concentration) at the two terminal points as illustrated in Fig. 5.8. Meanwhile, in the elements far from the joint, the damage is zero. As illustrated in Fig. 5.9, a greater damage concentrates on the centre of the joint with damage as 0.245. This is due to the curvature of joint of the material interface. The irregular

element discretization may be another factor to the damage concentration. It is worth to notice that the maximum damage in the calculation is about 0.25, which is much smaller than the critical damage value defined as the crack initiation criterion. According all the hypotheses supposed here, there is no "joint" propagation, the joint is stable during the "postulated" degradation process.

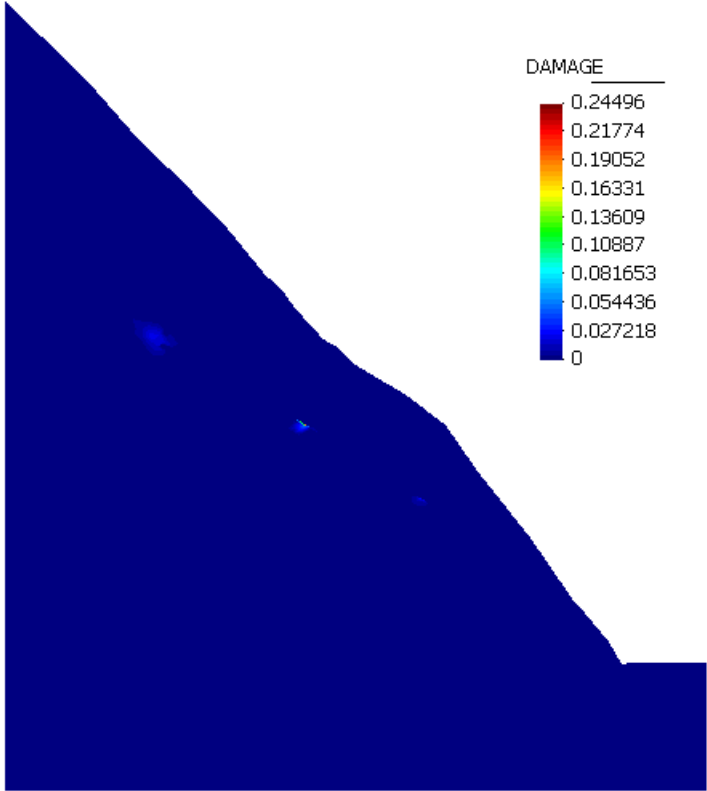
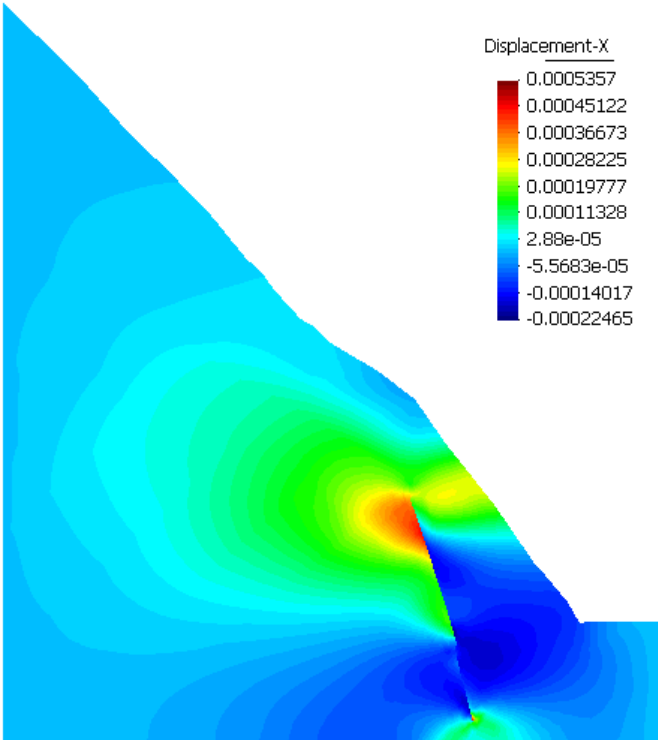


Figure 5.9 The distribution of the damage in the rock mass due to the joint degradation N°1

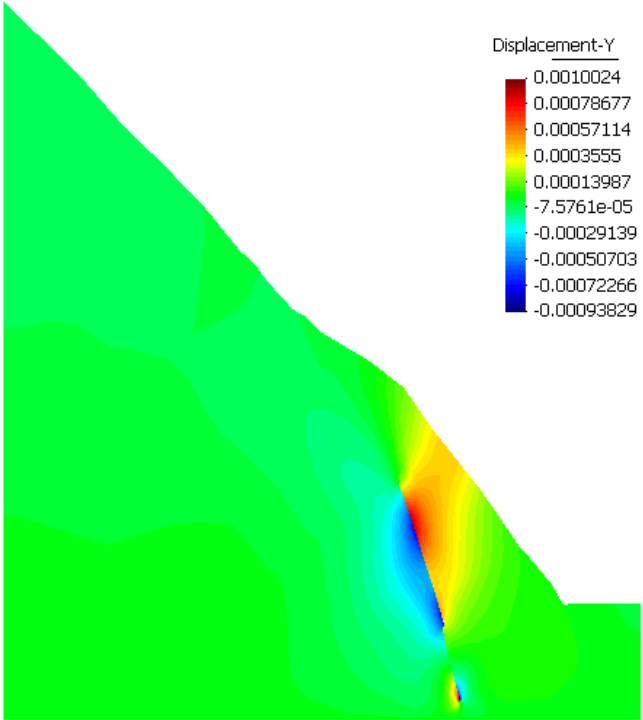
5.4.2. Numerical results for Joint N°2

The final displacements in the direction of both X-axis and Y-axis due to the degradation Joint N°2 are presented in Fig. 5.10. Due to the "release" of the shear stress on the rock joint surface, the similar "slide" phenomena as that of Joint N°1 is observed. However, not as that of Joint N°1, the displacement is mainly manifested in the X direction, in the case of Joint N°2, the induced displacement in Y direction is greater than that in X direction. In spite of the slide, the Joint N°2 has a tendency to rotate in the clockwise direction. That is due to the push from the rock located at up-right side of joint. On the other hand, the lower terminal of joint is imbedded in the deep rock where the displacement is limited by the boundary conditions. And in the lower part of joint, the compression stress is greater than that in the upper part which

caused bigger resistance in lower part. Because of the influence the distribution of initial stress, comparing with that of Joint N¹, the total displacement in current case is smaller.



(a) The distribution of the displacement in x direction



(b) The distribution of the displacement in y direction

Figure 5.10 The distribution of the displacement in section N²

The final stress states induced by the "degradation" process in Joint N² are presented in Fig. 5.11. Similar to that of the case Joint N¹, the distribution of stress is mainly concentrated in the near field of joint, especially at the vicinity area of two terminals of the joint and on the surface of joint where the "asperities" are presented. As that in case of Joint N¹, the traction zone in current case is also obvious. However, in the current case, the traction seems smaller that of Joint N¹. This is due to a greater initial stresses which offered a bigger resistance. With the same degradation, the "released" stress is smaller than that in case of Joint N¹, therefore the concentrated traction stress is smaller.

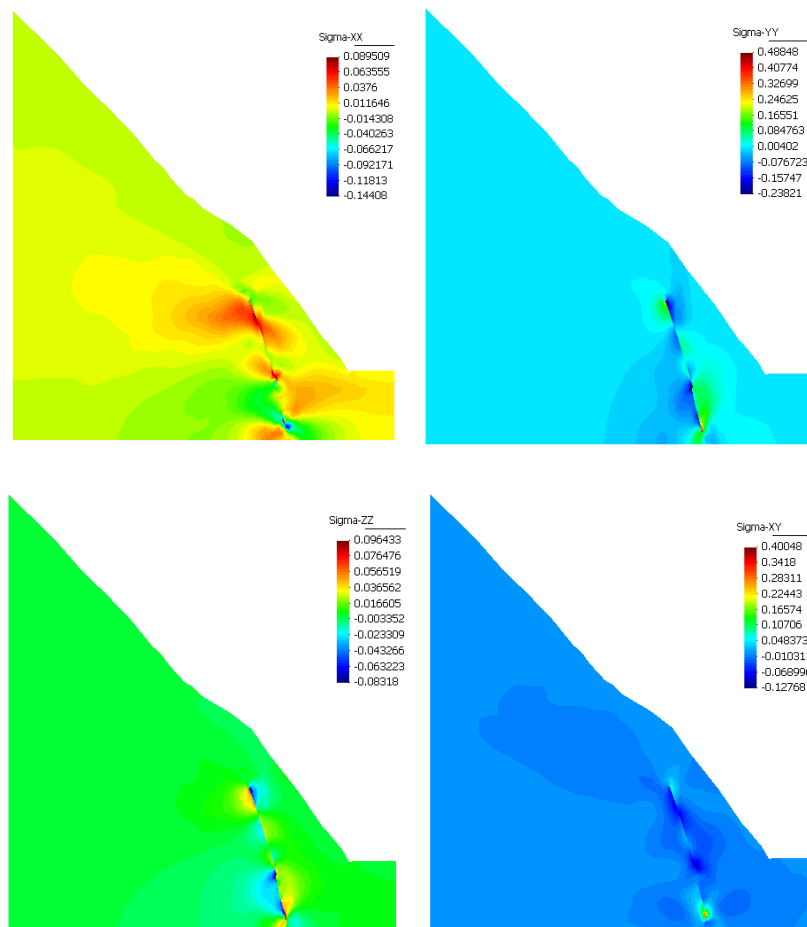


Figure 5.11 The distribution of the stress in the rock mass due to the joint degradation N²

The final stress states induced by the "degradation" process in Joint N² are presented in Fig. 5.11. Similar to that of the case Joint N¹, the distribution of stress is mainly concentrated in the near field of joint, especially at the vicinity area of two terminals of the joint and on the surface of joint where the "asperities" are presented. As that in case of Joint N¹, the traction zone in current case is also obvious. However, in the current case, the traction seems smaller that of Joint N¹. This is due to a greater initial stresses which offered

a bigger resistance. With the same degradation, the "released" stress is smaller than that in case of Joint N¹, therefore the concentrated traction stress is smaller.

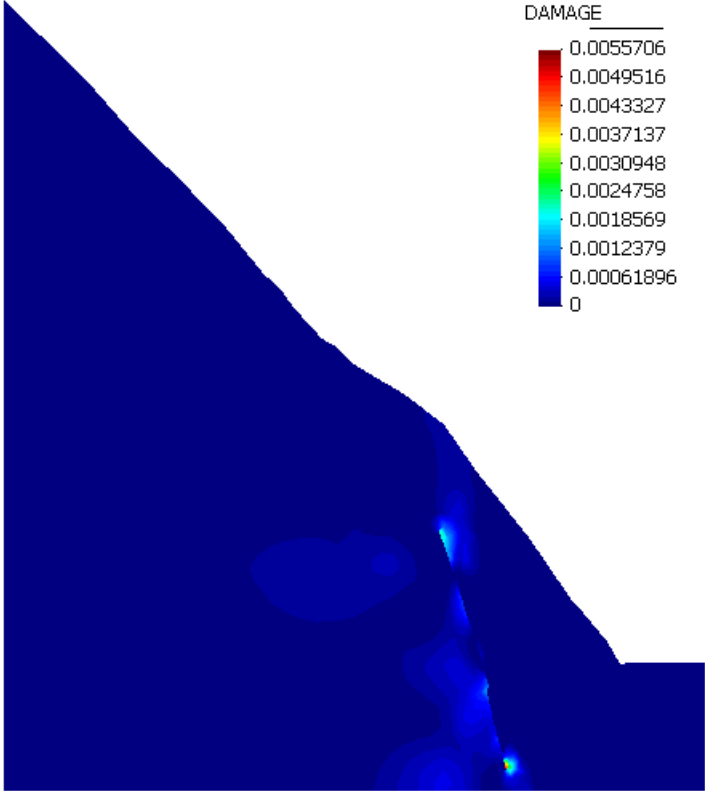
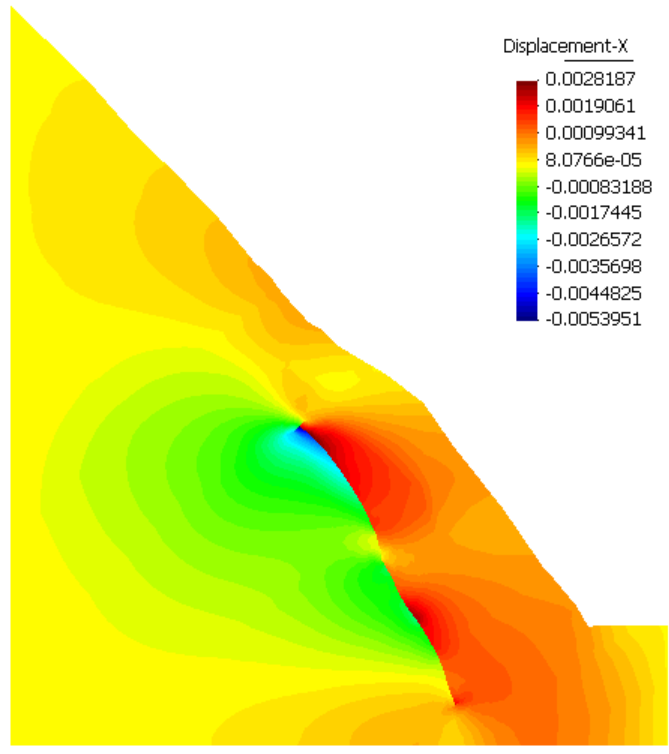


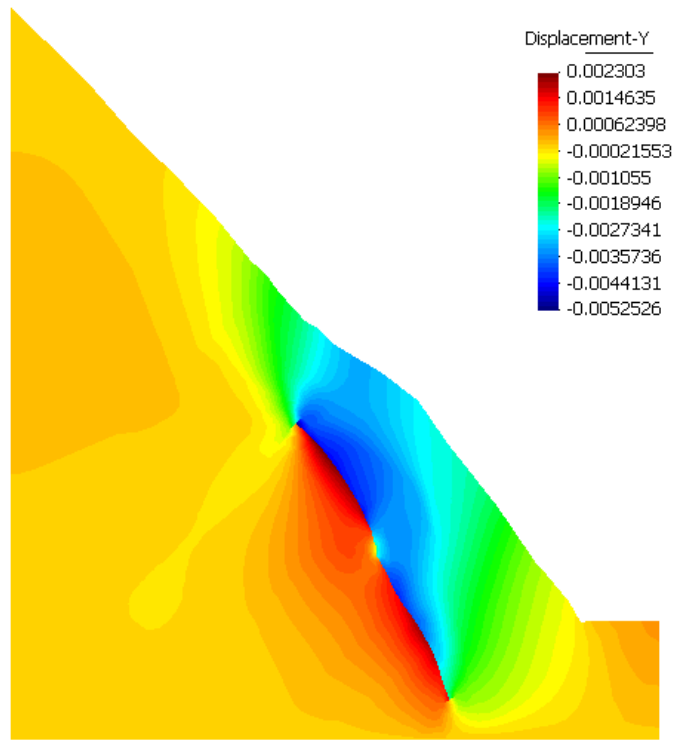
Figure 5.12 The distribution of the damage in the rock mass due to the joint degradation N²

5.4.3. Numerical results for Joint N³

For the Joint N³, with which the incline angle is about 61°, between the other two cases, 30° and 75° respectively for Joint N¹ and Joint N². Its geometry location is also between the two previous joints. The final displacements induced by the degradation Joint N³ are presented in Fig. 5.13. The amplitudes of the displacement in X and Y are quasi the same. The main phenomenon observed is the sliding along the joint surface. The maximum displacements in both X and Y directions are located at the up terminal point of the joint. This is due to the "released" shear stress of the joint surface mainly concentrated on the upper part and transferred to the rock around. Comparing with the other two cases, the amplitude of the displacement, just as its incline angle, is medium.



(a) The distribution of the displacement in x direction



(b) The distribution of the displacement in y direction

Figure 5.13 The distribution of the displacement in section N³

The final stress states induced by the "degradation" process in Joint N³ are presented in Fig. 5.14. Similar to that of the two previous cases, the distribution of stress is mainly

concentrated in the near field of joint, especially at the neighbouring zone of two terminals of the joint and on the surface of joint where the "asperities" are presented. The maximum traction values appear at the place where the curvature of joint changes.

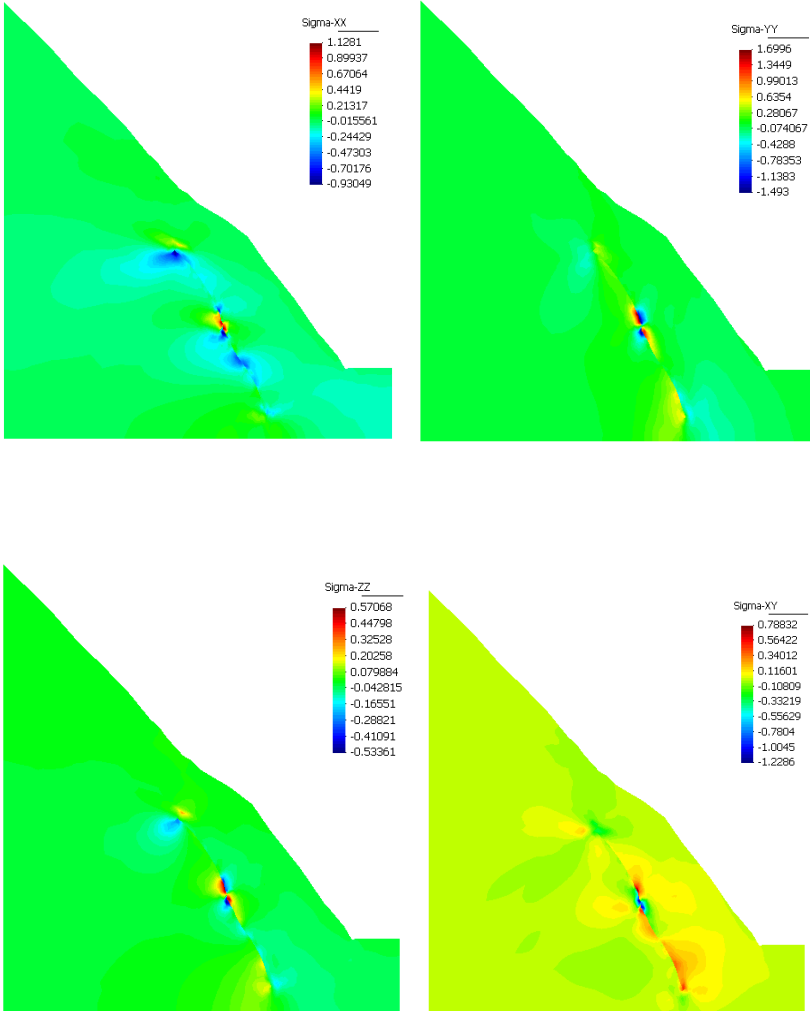


Figure 5.14 The distribution of the stress in the rock mass due to the joint degradation N 3

The distribution of the damage induced by the degradation process in Joint N 3 is presented in 5.15. The damage mainly concentrates near the joint surface, especially at the two terminal points and the transition point of the covertures. The maximum value of the damage is about 0.016, which is much less than the critical value for the crack propagation. As that of two previous cases, the current joint is stable during the "postulated" degradation process too.

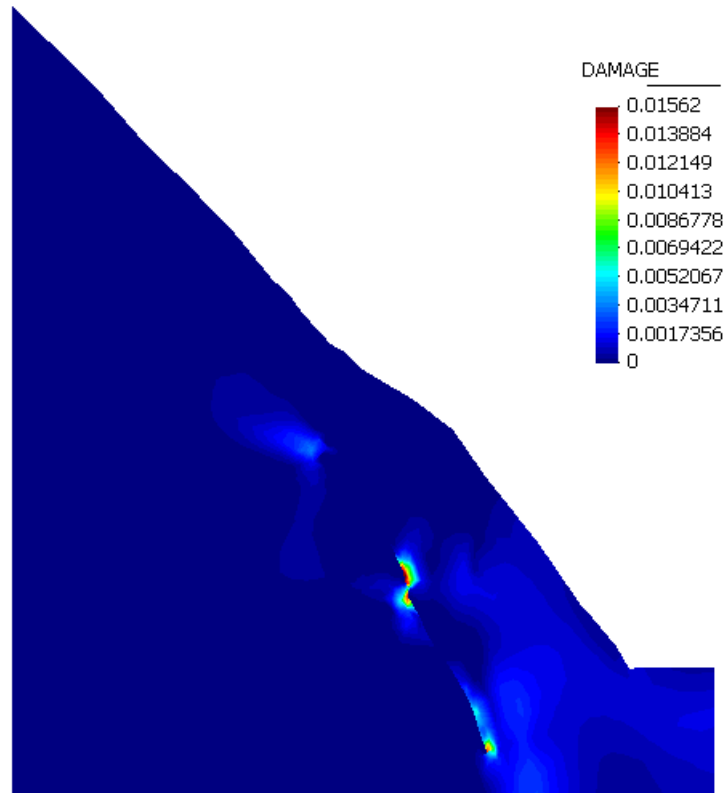


Figure 5.15 The distribution of the damage in the rock mass due to the joint degradation

5.4.4. Discussions

At the beginning of the construction, several monitor detectors are installed to test the in situ displacement and assess the long-term stability of slope. Several horizontal adits are arranged and excavated for the installation of the displacement detectors. The displacement detectors installed in deep rock masses is composed of graphite pole convergence meter, displacement across valley measuring line, leveling point and sliding micrometer. In the chosen section, there is an adit excavated for displacement monitors. The position of adit and detector is given in Fig. 5.16. As illustrated in Fig. 5.17, the displacements of 7 representative points of the detector are fetched to observe the deformation state.

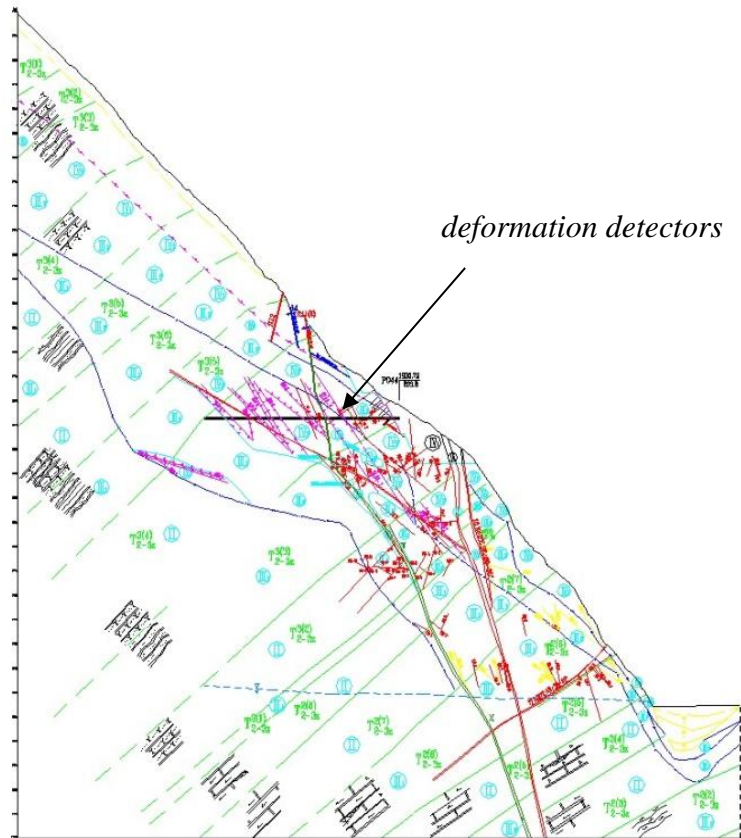


Figure 5.16 The position of the observation gallery in current section (From internal report)

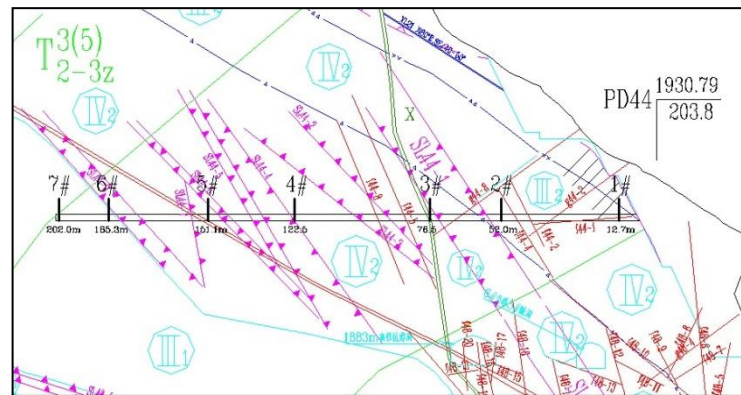


Figure 5.17 The position of the detectors in the observation gallery (From internal report)

As shown in Fig. 5.18, the monitoring results for more than 1600 days are showed. These deformations are mainly concerning the creep deformation caused by the excavation. On the other hand, the duration of these observation results time is only for about 5 years. During our calculations mentioned above, it mainly concerning the degradation of joint in the future 100 years. However, the data given in Fig. 5.18 still shows the time effect in slope deformation.

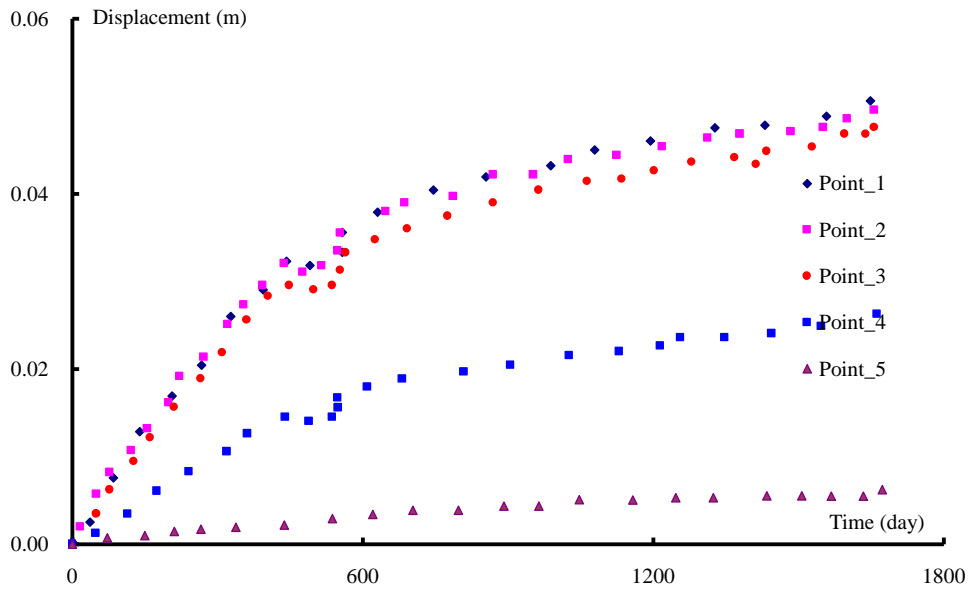


Figure 5.18 The historical displacement of each observation points (From internal report)

Among the 7 observation points, three points are chosen for discussion, separately the Point 1, Point 3 and Point 7. The historical displacements of these three points in both X-direction and Y-direction respectively for the three joints are presented in Fig.19-Fig.24.

In case of Joint N^o1, the joint by which the adit traversed. The Point 7 is located at the left side of joint, while Point 3 and Point 1 are located at the right side of joint. This is clearly reflected by the displacement in X direction, as illustrated in Fig.19. For Point 7, the displacement in X direction has a negative value, while those of Point 1 and Point 3 are positive. Comparing with Point 1, Point 3 is just near the joint. Thus during the degradation process, the displacement of Point 3 is greater than that of Point 1. While for the displacement in Y direction, all the three points have the same tendency in the negative direction of Y-axis. Globally, due to the degradation of the joint resistance, the strength of the structure weakens with time passage. Under the constant stresses, there will be subsidence (deformation in the negative direction Y-axis). This is available for all the three joints.

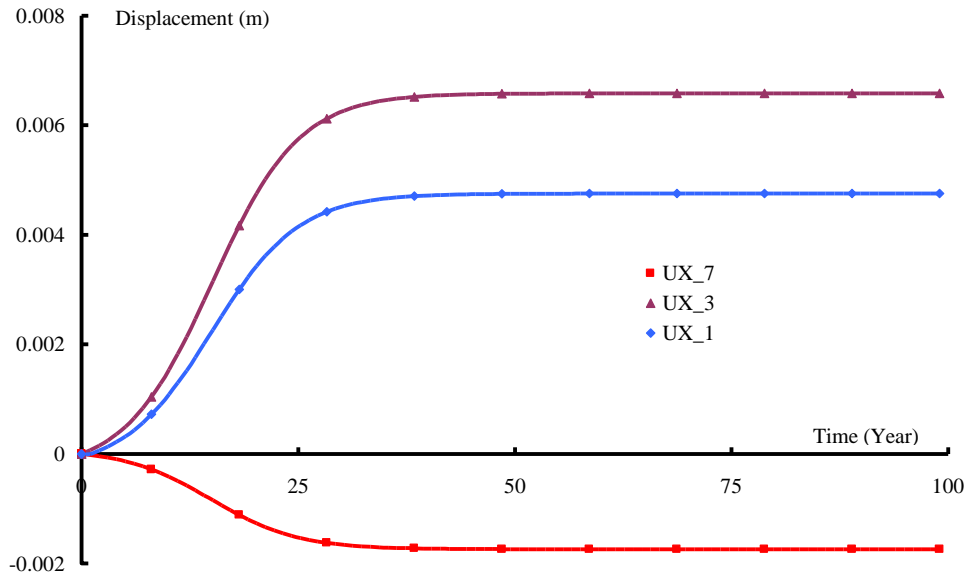


Figure 5.19 The historical displacement in X direction of three observation points induced by the degradation of Joint N^o1

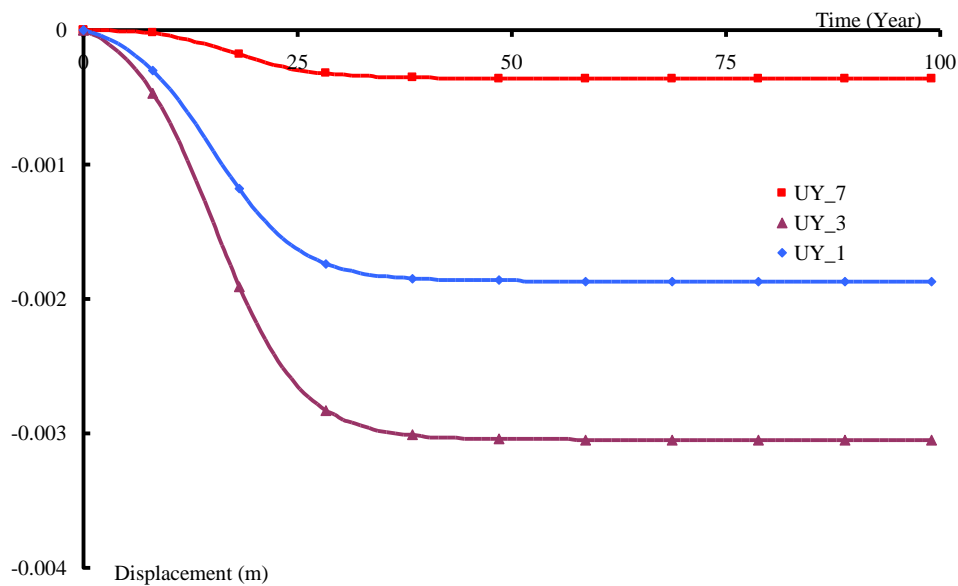


Figure 5.20 The historical displacement in Y direction of three observation points induced by the degradation of Joint N^o1

In the case of Joint N^o2, the displacements of the three points are presented in Fig. 5.21 and Fig. 5.22, respectively for the displacement in X and Y direction. Generally, the observations points are far from the joint. The effect of the joint degradation has little influence on the displacement of observation point. Therefore, the amplitude of displacement in both directions is small. Comparing with that of Joint N^o2, the upper terminal of Joint N^o3 is much closer to the detector. So the amplitude of the displacement in case of Joint N^o3 is greater than that of Joint N^o2.

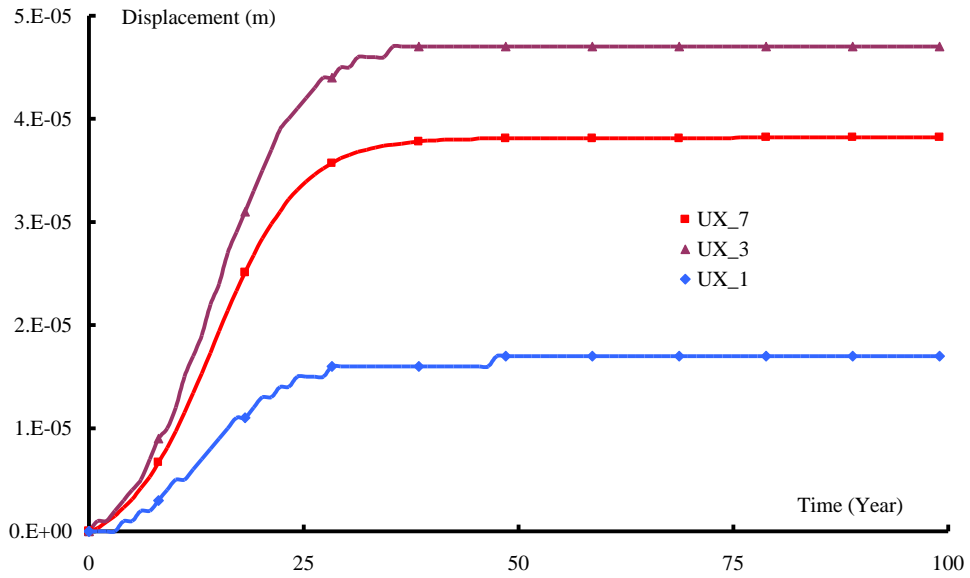


Figure 5.21 The historical displacement in X direction of three observation points induced by the degradation of Joint N 2

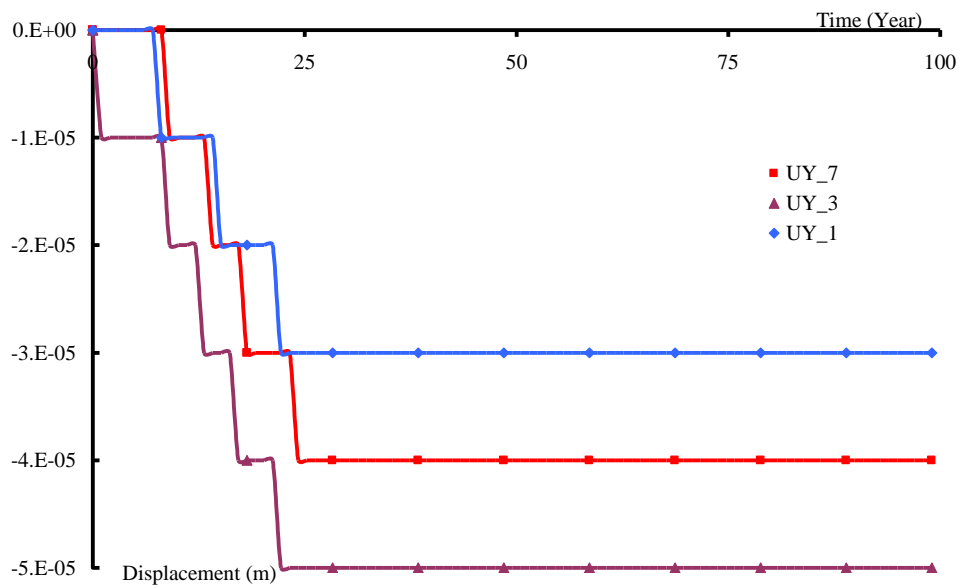


Figure 5.22 The historical displacement in Y direction of three observation points induced by the degradation of Joint N 2

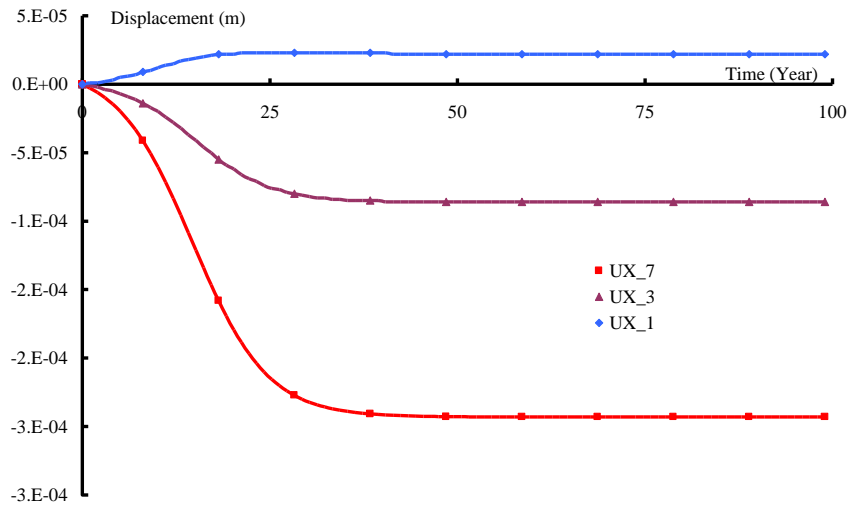


Figure 5.23 The historical displacement in X direction of three observation points induced by the degradation of Joint N 3

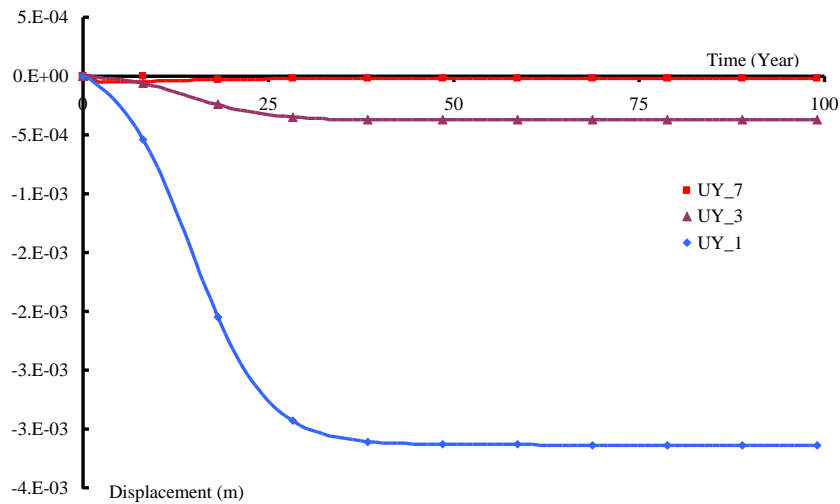


Figure 5.24 The historical displacement in Y direction of three observation points induced by the degradation of Joint N 3

5.5. Conclusion

In this chapter, the elasto-damage presented in chapter 2, the constitutive model for rock joint presented in chapter 3, the XFEM method presented in chapter 4 have been adopted to study the long-term stability of jointed rock slope in a great-scale hydraulic project. Three joints with different incline angle in different position have been chosen for current study. It is supposed that during the operational stage of this project, the rock joint's resistance degraded gradually with time passage. The numerical simulation results showed that, the release of stress due to joint degradation is a local behaviour. With all the parameters adopted, the damage caused by the degradation process is relatively small and far away from the critical value for the crack propagation.

Chapter 6. Conclusion and perspectives

6.1. General conclusion

In this thesis, numerical models are proposed to simulate the mechanical responses of rock matrix and rock joints for both the short-term and long-term situations.

Firstly, considering the influence of confining pressures, one elasto-damage model is ameliorated to describe the ductility of hard rocks, the simulation of a series of experimental results of marbles and meta-sandstones showed that the improved elasto-damage model is capable to describe the behaviour of hard rocks and it can especially reflect the ductile property of rocks. One time-dependent creep model is raised to simulate the short-term and long-term mechanical responses of rock matrix. Some simulations are also effected to verify the ability of this creep model.

Secondly and more importantly, under external loadings, the deformations tend to concentrated in the joint part or rock, therefore the joint part is significant in analyzing rock behaviour. Similarly with the rock matrix, a constitutive model is employed for rock joint, the asperity of joint surface is represented by a parameter JRC . For this instantaneous model, both the normal and shear stiffness are discussed, the asperity, friction angle and length of joint surface are taken into consideration. For long-term model, the asperity parameter JRC is supposed to be time-dependent, and then some related parameters become variables of time. Several sensitive analyses are performed to study the effect of time related parameters. Experimental results are employed to validate the time-dependent model, the simulation results showed that this model have exact ability to describe the creep phenomenon of rock joint.

For describing the opening and propagation of rock fractures more precisely, extended finite element method (XFEM) is employed. This method works by introducing additional degrees of freedom, which could reflect the fracture position in elements, into traditional finite element theory. A simple damage criterions is proposed for the joint initiation and validated by a simple traction example, in this example, the relationship normal joint departure and normal joint stress is traced, and then another simple slope mesh is created to analyze the influence of incline angle of joints.

At last, all the theories and models mentioned are applied to assess the stability of one huge hydraulic structure. Three main joints within the slope are studied in detail respectively,

the simulation results show that these models are capable in simulating the great structures with complicated components.

6.2. Perspectives

Based on the researches of this thesis, it is possible to suggest a number of perspectives for some further theoretical and applied works to improve the theoretical basis and ability of models for more efficiency and more precise simulations.

- 1) These models could be applied in more projects to examine their simulating ability.
- 2) For better solve real engineering problems, the models should be extended to three-dimensional algorithms. That would abundantly increase the calculation burden of computers. Algorithms more efficiency should also be developed to solve this problem.
- 3) New initial propagation criteria should be developed for exactly reflects the real discontinuities' situations.
- 4) By considering the complicated environments of projects, the coupling factors, i.e. the hydraulic, chemical and thermal effect for rocks, especially for rock joints could be taken into account in this model.

References

1. Zhou, J.W., W.Y. Xu, and X.G. Yang, *The 28 October 1996 landslide and analysis of the stability of the current Hua-shiban slope at the Liang-jiaren Hydropower Station, Southwest China*. Engineering Geology, 2010. **114**: p. 45-56.
2. Crozier, M.J. *Proceedings of the 8th International Conference and Field Trip on Landslides*. 1986. London: Croom Helm Pub.
3. Schuster, R.L. *The 25 most catastrophic landslides of the 20th century, in Chaocon*. in *Proceedings of the 8th International Conference and Field Trip on Landslides*. 1996.
4. Pamela, J.W., *Weathering*. Georgia Perimeter College.
5. Hoxha, D., et al., *A microstructural study of natural and experimentally induced cracks in a granodiorite*. Tectonophysics, 2005. **395**(1): p. 99-112.
6. Paterson, M.S. and T.F. Wong, *Experimental rock deformation-the brittle field*. 2005: Springer.
7. Eslami, J., D. Hoxha, and D.Grgic, *Estimation of the damage of a porous limestone using continuous wave velocity measurements during uniaxial creep tests*. Mechanics of materials, 2012. **49**: p. 51-65.
8. Homand, F. and J.F. Shao, *Mechanical behaviour of a porous chalk and effect of saturating fluid*. Mechanics of cohesive-frictional materials, 2000. **5**(7): p. 583-606.
9. Hadley, K., *Comparison of calculated and observed crack densities and seismic velocities in westerly granite*. Journal of Geophysical research, 1976. **81**(20): p. 3484-3494.
10. Shao, J.F., *Modeling of anisotropic damage and creep deformation in brittle rocks*. International Journal of Rock Mechanics & Mining Sciences, 2006. **43**(4): p. 582-592.
11. Ren, Z.J., X.H. Peng, and C.L. Yang, *Micromechanical damage model for rocks and concretes subjected to coupled tensile and shear stresses*. Acta Mechanica Solida Sinica, 2008. **21**(3): p. 232-240.
12. Chen, Y.F., et al., *Micromechanical analysis of anisotropic damage and its influence on effective thermal conductivity in brittle rocks*. International Journal of Rock Mechanics and Mining Sciences, 2012. **50**(0): p. 102-116.
13. Gu éry, A.A., et al., *A micromechanical model for the elasto-viscoplastic and damage behavior of a cohesive geomaterial*. Physics and Chemistry of the Earth, 2008. **33**(0): p. S416-S421.
14. Zhu, Q.Z., et al., *Micromechanical modelling of anisotropic damage in brittle rocks and application*. International Journal of Rock Mechanics and Mining Sciences, 2008. **45**(4): p. 467-477.
15. Jiang, T., et al., *Experimental investigation and micromechanical analysis of damage and permeability variation in brittle rocks*. International Journal of Rock Mechanics and Mining Sciences, 2010. **47**(5): p. 703-713.
16. Sacco, E. and F. Lebon, *A damage-friction interface model derived from micromechanical approach*. International Journal of Solids and Structures, 2012. **49**(26): p. 3666-3680.
17. Zhou, X.P. and H.Q. Yang, *Micromechanical modeling of dynamic compressive responses of mesoscopic heterogenous brittle rock*. Theoretical and Applied Fracture Mechanics, 2007. **48**(1): p. 1-20.

- 18.Xie, N., et al., *Micromechanical analysis of damage in saturated quasi brittle materials*. International Journal of Solids and Structures, 2012. **49**(6): p. 919-928.
- 19.Kuhl, E., E. Ramm, and R.d. Borst, *An anisotropic gradient damage model for quasi-brittle materials*. comput. methods Appl. Mech, 2000. **183**: p. 87-103.
- 20.Desmorat, R., F. Gatuíngt, and F. Ragueneau, *Nonlocal anisotropic damage model and related computational aspects for quasi-brittle materials*. Engineering fracture mechanics, 2007. **74**(10): p. 1539-1560.
- 21.Brunig, M., *An anisotropic continuum damage model: theory and numerical analyses*. Latin american journal of solids and structures, 2004. **1**: p. 185-218.
- 22.Voyiadjis, G.Z. and B. Deliktas, *A coupled anisotropic damage model for the inelastic response of composite materials*. Comput. methods Appl. Mech, 1998. **183**: p. 159-199.
- 23.Edelen, D.G.B., *Non-local Field Theory*. A.C. Eringen (Ed.), Continuum Physics, 1976. **4**: p. 75-204.
- 24.Eringen, A.C., C.G. Speziale, and B.S. Kim, *Crack Tip Problem in Non-local Elasticity*. J. Mech. Phys. Solids, 1977. **25**: p. 339-355.
- 25.Pijaudier-Cabot, G. and Z.P. Bazant, *Nonlocal damage theory*. J Eng Mech ASCE, 1987. **113**: p. 1512-1533.
- 26.Bazant, Z.P., G. Pijaudier-Cabot, and G. CALT, *Nonlocal continuum damage: Localization instability and convergence*. Journal of Appl Mech, 1988. **55**: p. 287-293.
- 27.Bazant, Z.P. and J. Ozbolt, *Nonlocal microplane model for fracture, damage and size effect in structures*. Journal of Engineering Mechanics, ASCE, 1990. **116**(11): p. 2485-2505.
- 28.Zhu, Q.Z., J.F. Shao, and D. Kondo, *A micromechanics-based non-local anisotropic model for unilateral damage in brittle materials*. C. R. Mecanique, 2008. **336**: p. 320-328.
- 29.Pijaudier-Cabot, G. and Z.P. Bazant, *Dynamic stability analysis with nonlocal damage*. Computers and structures, 1988. **29**(3): p. 503-507.
- 30.Johansson, F., *Shear strength of unfilled and rough rock fractures in sliding stability analyses of concrete dams*. Thesis of Royal institute of technology, Stockholm, 2009.
- 31.Woo, I., J. Fleurisson, and H. Park, *Influence of weathering on shear strength of fractures in a porphyritic granite rock mass in Jechon area, South Korea*. Geoscience journal, 2010. **14**: p. 289-299.
- 32.Rafek, A.G., T.L. Goh, and M.H. Arifin, *Correlation of Joint Roughness Coefficient with Peak Friction Angles of Discontinuity Planes of Schists, Peninsular Malaysia*. Sains Malaysiana, 2012. **41**(3): p. 293-297.
- 33.Mohd-Nordin, M.M., et al., *Long-wavelength elastic wave propagation across naturally fractured rock masses*. Rock Mech Rock Eng, 2014. **47**(2): p. 561-573.
- 34.Grasselli, G., *3D behavior of bolted rock joints: experimental and numerical study*. International journal of rock mechanics and mining sciences, 2005. **42**: p. 13-24.
- 35.Lacroix, P. and D. Amitrano, *Long term dynamic of rock slides and damage propagation inferred from mechanical modelling*. Journal of Geophysical research, 2013. **118**: p. 2292-2307.
- 36.Crouch, S.L., *Solution of plane elasticity problems by the displacement discontinuity method*. int. J. numer. anal. methods geomech, 1976. **10**: p. 301-343.
- 37.Cundall, P.A. and O.D.L. Strack, *A discrete numerical model for granular assemblies*. Geotechnique, 1979. **29**: p. 47-65.

38. Shi, G.H., *Manifold method of material analysis*. Proceedings of the transaction of the ninth army conference on applied mathematics and computing, 1991: p. 57-76.
39. Li, S.C. and Y.M. Cheng, *Enriched meshless manifold method for two-dimensional crack modeling*. Theoretical and Applied Fracture Mechanics, 2005. **44**(3): p. 234-248.
40. Mões, N., J. Dolbow, and T. Belytschko, *Finite element method for crack growth without remeshing*. Int. J. Numer. Methods Eng, 1999. **46**(1): p. 131-150.
41. Griggs, D.T., *Creep of rocks*. Journal of Geology, 1939. **47**: p. 225-251.
42. Haupt, M., *A constitutive law for rock salt based on creep and relaxation tests*. Rock Mechanics and Rock Engineering, 1991. **24**: p. 179-206.
43. Maranini, E. and M. Brignoli, *Creep behaviour of a weak rock: experimental characterization*. International Journal of Rock Mechanics and Mining Sciences, 1999. **36**(1): p. 127-138.
44. Fujii, Y. and T. Kiyama, *Circumferential strain behaviour during creep tests of brittle rocks*. International Journal of Rock Mechanics and Mining Sciences, 1999. **6**: p. 323-337.
45. Muriel, G.B., *Creep behavior of Bure clayey rock*. Applied Clay Science, 2004. **26**(1-4): p. 449-458.
46. Singh, D.P., *A study of creep of rocks*. International Journal of Rock Mechanics and Mining Sciences & Geomechanics, 1975. **12**(9): p. 271-276.
47. Ohnaka, M., *Acoustic emission during creep of brittle rock*. International Journal of Rock Mechanics and Mining Sciences & Geomechanics, 1983. **20**(3): p. 121-134.
48. Boukharov, G.N., M.W. Chanda, and N.G. Boukharov, *The three processes of brittle crystalline*. International Journal of Rock Mechanics and Mining Sciences & Geomechanics, 1995. **32**(4): p. 325-335.
49. Kazuhiko, M., O. Yoshiaki, and H. Hideyuki, *Micromechanics-based prediction of creep failure of hard rock for long-term safety of high-level radioactive waste disposal system*. Mechanics of Materials, 2003. **35**(3-6): p. 587-601.
50. Deng, R.G., *A new rock creep model*. Chinese Journal of Rock Mechanics and Engineering, 2001. **20**(6): p. 780-784.
51. Cao, S.G., *A improved rock creep model*. Chinese Journal of Rock Mechanics and Engineering, 2002. **21**(5): p. 632-634.
52. Yuan, H.P., *Visco-elastoplastic constitutive relationship of rock and modified Burgers creep model*. Chinese Journal of Rock Mechanics and Engineering, 2006. **28**(6).
53. Jin, J. and N.D. Cristescu, *An elastic/viscoplastic model for transient creep of rock salt*. International Journal of Plasticity, 1998. **14**(1-3): p. 85-107.
54. Yang, C., J.J.K. Daemen, and J.-H. Yin, *Experimental investigation of creep behavior of salt rock*. International Journal of Rock Mechanics and Mining Sciences, 1999. **36**(2): p. 233-242.
55. Wang, G., et al., *Experimental investigations of the creep-damage-rupture behaviour of rock salt*. International Journal of Rock Mechanics and Mining Sciences, 2014. **66**: p. 181-187.
56. Wang, G., *A new constitutive creep-damage model for salt rock and its characteristics*. International Journal of Rock Mechanics and Mining Sciences, 2004. **41**: p. 61-67.

57. Molladavoodi, H. and A. Mortazavi, *A damage-based numerical analysis of brittle rocks failure mechanism*. Finite Elements in Analysis and Design, 2011. **47**(9): p. 991-1003.
58. Xie, N., et al., *Micromechanical analysis of damage in saturated quasi brittle materials*. International Journal of Solids and Structures, 2012. **49**(6): p. 919-928.
59. Shao, J.F., K.T. Chau, and X.T. Feng, *Modeling of anisotropic damage and creep deformation in brittle rocks*. Int. J. Rock Mech. Min. Sci. and Geomech, 2006. **43**(4): p. 582-592.
60. Budiansky, B. and R.J. O'Connell, *Elastic moduli of a cracked solid*. International Journal of Solids and Structures, 1976. **12**(2): p. 81-97.
61. Bazant, Z.P., T. Belytschko, and T.P. Chang, *Continuum theory for strain-softening*. J Eng Mech ASCE, 1984. **110**: p. 1666-1692.
62. Petley, D., M. Bulmer, and W. Murphy, *Patterns of movement in rotational and translational landslides*. Geology, 2002. **30**(9): p. 719-722.
63. Baud, P. and P. Meredith, *Damage accumulation during triaxial creep of darley dale sandstone from pore volumetry and acoustic emission*. Int. J. Rock Mech. Min. Sci. and Geomech, 1997. **24**: p. 1-8.
64. Mazars, J. and G. Pijaudier-Cabot, *Continuum damage theory: Application to concrete*. J. Eng. Mech, 1989. **115**: p. 345-365.
65. Lemaitre, J., *A continuous damage mechanics model for ductile fracture*. J. Eng. Mater. Technol, 1985. **107**: p. 83-89.
66. Simo, J.C. and J.W. Ju, *Strain and stress based continuum damage models – I Formulation*. Int. J. Solids Struct, 1987. **23**(821-840).
67. Yang, S.Q., *Study on rheological mechanical properties of rock and its engineering applications*. thesis of Hohai University, 2006.
68. Meng, Z.P., *Temperature and pressure under deep conditions and their influences on mechanical properties of sandstone*. Chinese Journal of Rock Mechanics and Engineering, 2006. **25**: p. 1177-1181.
69. Goodman, R.E., *Introduction to rock mechanics*. 1980.
70. Amadei, B. and S. Seab, *Constitutive models of rock joints*. 1990.
71. Amadei, B. and S. Seab, *Modelling rock joints under shear and normal loading*. Int. J. Rock Mech. Min. Sci. & Geomech, 1992. **29**(3): p. 267-278.
72. Plesha, M.E., *Constitutive models for rock discontinuities with dilatancy and surface degradation*. Int. J. numer. anal. methods geomech, 1987. **11**: p. 345-362.
73. Nguyen, T.S., *Selvadurai A. P. S. A model for coupled mechanical and hydraulic behaviour of a rock joint*. Int. J. numer. anal. methods geomech, 1998. **22**: p. 29-48.
74. Bandis, S.C., A.C. Lumb, and N.R. Barton, *Fundamentals of rock joint deformation*. International Journal Rock Mechanics Mining Science & Geomechanics, 1983. **20**(2): p. 121-129.
75. Barton, N., S. Bandis, and K. Bakhtar, *Strength, Deformation and Conductivity Coupling of Rock Joints*. Int. J. Rock Mech. Min. Sci. & Geomech, 1985. **22**(3): p. 121-140.
76. Bart, M., *Contribution à la modélisation du comportement hydromécanique des massifs rocheux avec fractures*. Thesis of Lille 1, 2000.
77. Hordijk, D.A., *Local approach to fatigue of concrete*. Doctoral thesis of Delft University of Technology, 1991.
78. Goodman, R.E., *Methods of geological engineering in discontinuous rocks*. West publishing Co., 1976.

79. Michalowski, R. and Z. Mroz, *Associated and non-associated sliding rules in contact friction problems*. ARCH. MECH. STOSOW, 1978. **3**: p. 259-276.
80. Bandis, S., *Experimental studies of scale effects on shear strength and deformation of rock joints*. Ph. D. thesis, 1980, Univ. of Leeds, Dept of Earth Sciences, 1980.
81. Benjelloun, Z.H., *Etude expérimentale et modélisation du comportement hydromécanique des joints rocheux*. Thèse de l'Université de J. Fourier, Grenoble, 1991.
82. Barton, N. and V. Choubey, *The shear strength of rock joints in theory and practice*. Rock Mechanics, 1977. **10**: p. 1-54.
83. Bandis, S., A.C. Lumsden, and N. Barton, *Experimental studies of scale effects on the shear behaviour of rock joints*. Int. J. Rock Mech. Min. Sci. & Geomech, 1981. **18**(1-21).
84. Skinas, C.A., S.C. Bandis, and C.A. Demiris, *Experimental investigations and modelling of rock joint behaviour under constant stiffness*. Proc. Int. Symp. on Rock Joints, Loen, Norway, Balkema, 1990: p. 301-308.
85. Gutierrez, M., L.E. Øino, and K. Høeg, *The effect of fluid content on the mechanical behaviour of fractures in chalk*. Rock Mechanics and Rock Engineering, 2000. **33**(2): p. 119-129.
86. Woo, I., J.A. Fleurisson, and H.J. Park, *Influence of weathering on shear strength of joints in a porphyritic granite rock mass in Jechon area*. Geosciences Journal, 2010. **14**(3): p. 289-299.
87. Gong, C., *creep character and stability analysis of left bank slope of jinping project*. master thesis of Chengdu University of Technology, 2011: p. 50.
88. Belytschko, T. and T. Black, *Elastic crack growth in finite elements with minimal remeshing*. Int. J. Numer. Methods Eng, 1999. **45**(5): p. 601-620.
89. Wells, G.N., L.J. Sluys, and R.d. Borst, *Simulating the propagation of displacement discontinuities in a regularized strain-softening medium*. Int. J. Numer. Methods Eng, 2002. **53**: p. 1235-1256.
90. Karihaloo, B.L. and Q.Z. Xiao, *Modeling of stationary and growing cracks in FE framework without meshing: A state of the art review*. Comput. Struct., 2003. **81**(3): p. 119-129.
91. Mariani, S. and U. Perego, *Extended finite element method of quasi-brittle fracture*. Int. J. Numer. Methods Eng., 2003. **58**(1): p. 103-126.
92. Zhu, Q.Z., *On enrichment functions in the extended finite element method*. Int. J. Numer. Meth. Engng, 2011. **00**: p. 1-33.
93. CAMPS, G., *Etude des interactions chemo-mécaniques pour la simulation du cycle de vie d'un élément de stockage en béton*. thèse de l'Université de Toulouse, 2008.
94. Nuismer, R., *An energy release rate criterion for mixed mode fracture*. Int. J. Fract., 1975. **11**: p. 245-250.
95. Sih, G., *Strain-energy-density factor applied to mixed-mode crack problems*. Int. J. Fract. , 1974. **10**: p. 305-321.
96. Erdogan, F. and G. Sih, *On the crack extension in plates under plane loading and transverse shear*. J. Basic Eng., 1973. **85**: p. 519-527.
97. Hoek, E., P.K. Kaiser, and W.F. Bawden, *Support of Underground Excavations in Hard Rock*. 1995, Rotterdam: Balkema.
98. Liu, Z.B., et al., *Comprehensive Stability Evaluation of Rock Slope Using the Cloud Model-Based Approach*. Rock Mech Rock Eng, 2013.